Università degli Studi di Padova
Centro interdipartimentale "Centro Ricerche Fusione"

Universidade de Lisboa
Instituto Superior Técnico (IST)

JOINT RESEARCH DOCTORATE IN FUSION SCIENCE AND ENGINEERING
Cycle XXVIII

Theoretical analysis of tokamak disruptions by simplified analytical models and numerical simulations

Coordinator: Prof. Paolo Bettini
Supervisors: Dr. Roberto Paccagnella, Prof. Roberto Turolla

Candidate: Vadim Yanovskiy

Padova, January 2016

ABSTRACT

One of the main obstacle on the way to the commercial fusion reactor based on the tokamak configuration is disruptions, which are abrupt terminations of the plasma discharge. Being not mitigated they can cause severe damage to the machine. For future large devices, like ITER and DEMO, strong electromagnetic loads on the vacuum vessel during disruptions pose a threat to their structural integrity. Some estimates for ITER give alarming hundred MN, but the lack of the predictive theory including all the effects into account, raise a concern about the accuracy of these evaluations. The largest forces are observed when plasma touches the wall. Their amplitudes depend on the halo currents, which are the part of the plasma current flowing into the conducting structures and then returning back into the plasma. Uncertainties in the halo current distribution and dynamics are a challenge for the theoretical modelling. The first part of this thesis presents the calculations of the EM force acting on the vacuum vessel within single-mode cylindrical approximation and the analysis of the interplay between eddy currents, plasma surface currents and halo currents.

The second part of the thesis is dedicated to the most dangerous instabilities that can lead to a disruption: the resistive wall mode RWM and the tearing mode. In the presence of the resistive wall both can be suppressed or partially mitigated by the plasma rotation. This effect is studied analytically for configurations with positive and negative magnetic shear. For the advance tokamak scenario with hollow equilibrium current profile the influence of the differential plasma rotation on the double tearing mode stability is analyzed. The double and triple wall assemblies with different parameters are considered with respect to the problem of the magnetic island locking. In particular, a simple analytical formula for the electromagnetic torque acting on the plasma is derived for the ITER wall arrangement with double vacuum vessel and blanket.

PREFAZIONE

Uno dei principali ostacoli sulla via della realizzazione di un reattore a fusione commerciale che si basi sulla configurazione Tokamak è rappresentato dalle disruzioni, cioè dalle terminazioni veloci della scarica di plasma, che se non adeguatamente mitigate possono causare danni gravi al reattore. Per futuri grandi impianti come ITER o DEMO, i forti carichi elettromagnetici sul contenitore da vuoto (vessel) durante le disruzioni possono minacciarne l'integrità strutturale. Alcune stime per ITER prevedono forze di decine di MN, ma la mancanza di una teoria veramente predittiva e completa, che includa tutti gli effetti rilevanti, solleva anche preoccupazioni sull'accuratezza di queste previsioni. Le forze più elevate sono osservate sperimentalmente quando il plasma viene in contatto con la prima parete. L'ampiezza dipende dalle cosiddette correnti di halo, che rappresentano la parte di corrente di plasma che può fluire verso le strutture conduttive ed eventualmente richiudersi nuovamente sul plasma stesso. Incertezze sull'ampiezza e la distribuzione delle correnti di halo e sulla dinamica del processo rappresentano una sfida aperta ai modelli teorici. La prima parte del lavoro di tesi presenta il calcolo delle forze elettromagnetiche sul vessel esercitate da una perturbazione in approssimazione cilindrica e l'analisi e la relazione tra vari tipi di correnti: le correnti indotte (eddy), le correnti di superficie (surface) e le correnti di halo propriamente dette.

La seconda parte della tesi è dedicate alle instabilità più pericolose che possono portare a disruzioni: I modi di parete detti Resistive Wall Modes (RWM) e i modi tearing o riconnettivi. In presenza di una parete resistiva entrambi possono essere soppressi o almeno mitigati dalla rotazione di plasma. Questo effetto viene studiato analiticamente per configurazioni con shear magnetico positive e negative. Si analizza l'effetto della rotazione nel caso specifico di uno scenario tokamak avanzato con profilo di corrente cavo. Rispetto al problema del frenamento di un'isola magnetica vengono considerati gli effetti di pareti resistive multiple (fino a 3) aventi diverse conducibilità elettriche. In particolare viene derivata una formula analitica semplice per il momento elettromagnetico esercitato dalla parete di ITER, comprendente vessel e blanket.

Contents

I. INTRODUCTION

1.1.Tokamaks

It is very interesting to fashion from clay. To fashion from three-dimensional vector fields, like magnetic and velocity ones, is even more fun. However, the equations governing the dynamics of plasma are a stubborn material – closer to Carrara marble. Titans of the last century sculpted magnificent models and provoked an ocean of physical effects, neglecting the irrelevant and grasping the essential [1-4]. They also developed powerful chisels that are routinely used nowadays [5-7].

One of the practical applications for the art and handicraft of neglecting is the extraction of the energy from the matter, for example, using the following fusion reaction

$$ {}_1\mathbf{D}^2 + {}_1\mathbf{T}^3 = {}_2\mathbf{He}^4 + {}_0\mathbf{n}^1 + 17.6\,\mathrm{MeV}. \qquad (1.1) $$

These 17.6 MeV of kinetic energy can be transformed, in principle, into the electricity for a fridge, however, there are still several unsolved physical and engineering problems. To realize the above reaction one needs high plasma pressure: present naturally in the Sun's core due to gravity, and on the Earth's surface created artificially in a strong magnetic field. One of the machines for this purpose is called the tokamak [8]. To build a commercial fusion reactor based on tokamak configuration, a way must be found to avoid disruptions - sudden terminations of plasma discharges, causing severe damage to plasma-facing and structural components [9, 10].

From a magneto-hydro-dynamic (MHD) point of view tokamaks are a family of thermonuclear musical instruments. Its sole toroidal string is confined by twisted magnetic field lines and, like a violin's chord, can suddenly break. If one smashes a metal torus with a hammer there will be a sound composed of the frequencies determined by the parameters of the doughnut. The plasma ring contains such a hammer (the energy source) within itself and sometimes behaves as if made of the finest Murano glass. The reason is that the volume of some magnetic tones can grow to a level high enough to tear the magnetic configuration, therefore in our study we are interested not only in their frequencies but primarily in their growth rates.

1.2. Instabilities

The string vibration is a superposition of harmonics characterized by only one mode number. Modes of a circular membrane are specified by two numbers, since there are nodes in radial and angular directions. Three are for a solid cylinder. In the study of a cylinder made of plasma we consider only the fundamental radial harmonic, because it is the fastest one, therefore, the perturbations have only poloidal m and longitudinal n numbers. For the disruption-free tokamak operation it is not necessary to suppress all the modes, some of them being properly controlled can work to the benefit, for example, $m=1$ mode can serve for helium ash removal from the plasma core [11]. The most dangerous modes that can lead to a disruption have low m and n numbers: $m/n=2/1$, $m/n=3/1$ and $m/n=3/2$. They are the focus of the present study.

The ideal kink is the harmonic that transforms the energy stored in the plasma pressure and/or current gradients into the kinetic energy of the plasma fluid distorting strongly the plasma column into a helix. If it grows uncontrollably, at certain amplitude plasma touches the surrounding solid structures, contaminates by impurity ions and collapses. In contrast, the tearing modes release the plasma potential energy through the resistive dissipation and the magnetic reconnection changing the magnetic field topology. Being not mitigated, they can provoke the global stochastization of magnetic field lines, which is followed by a disruption.

If plasma is surrounded by a nearby conductive shell, for example, a vacuum vessel, then the typical growth time of ideal modes increases from fractions of a microsecond to tens of milliseconds. In this case the ideal kinks are called resistive wall modes RWMs and are slow enough to be controlled by externally applied magnetic perturbations [12-14]. Another stabilizing mechanism of RWMs allowing the operation under higher pressure comes from the plasma rotation. Being first observed in tokamak DIII-D in 1995 [15, 16] it still remains a mystery, at least till now there is no universally recognized predictive theory explaining the effect. Different physical reasons can, at least hypothetically, lead to the rotational stabilization, such are: Landau damping [17], resistive energy dissipation [18, 19], the mode resonances with Alfvén continuum [20] or bounce/precession motions of thermal [21, 22] and fast particles [23]. There are also strong theoretical indications that the mode rotation combined with a nonlinear (due to the skin effect) energy sink in the resistive wall can contribute to the stabilization [24]. Recently an extension of the energy principle was proposed [25] that allows incorporation of any mechanism into a standard scheme. It gives a basis for a systematic comparison of all these theories within a unified general

approach. This important task can be realized only numerically, as a preparation to it, in the present thesis the effect of the resistive dissipation on the rotational stabilization is studied analytically with an accent on the comparison between the influence of the plasma rotation on the RWMs and linear tearing modes and with an emphasis on the interplay between the mode and plasma rotation. The results are presented in Chapter 5.

A linearly unstable tearing mode leads to the magnetic reconnection and the formation of a magnetic island, which changes the magnetic topology and deteriorates the confinement properties. In the presence of a resistive wall and the plasma rotation, non-linear growth of magnetic islands saturates at smaller amplitudes. However, rotating modes provoke the resistive wall to exert the electromagnetic torque on the plasma that results in the mode locking and following mode growth up to the level that can cause a disruption. The dynamics of the island growth and locking is studied in Chapter 6 under different wall configurations and for various equilibrium current profiles.

1.3.Disruptions

While the physics of disruptions is not yet properly understood, one can distinguish between two main mechanisms leading to the plasma collapse:

(1) The non-linear growth, interaction and overlapping of magnetic islands causing the fast global stochastization of magnetic field lines.

(2) The non-linear development of the ideal kink.

Both ways result in the sudden (less than 1 ms) cooling of the plasma to sub-KeV temperatures and global contamination of the plasma by impurity ions from the plasma facing components. These factors increase dramatically the plasma electrical resistivity that causes fast decay of the plasma current.

During the current quench the vacuum vessel is the subject of strong sideways electromagnetic force [26]. In the JET tokamak it can be so large (up to 4 MN) that it led to the considerable displacements of the vessel [27-31]. Upper estimates for ITER give alarming 40-50MN [32], 70MN [33, 34] and 80MN [35]. Since the plasma dynamics is complex these calculations were performed under certain constraints and simplifications, that raises a concern about their reliability and possible underestimation of the loads. On the other hand, simple

analytical analysis can provide some insight and basic understanding of the problem. The calculation of the sideways force within single-mode approximation is presented in Chapter 3.

The largest forces are observed when plasma touches the wall. In this case the problem complicates by the presence of halo currents, which are the part of the plasma current flowing into the wall and then returning back somehow. In spite of the fact that, uncertainties in their distribution and amplitudes make the modelling problematic, some theoretical efforts in this direction has been done. The recent theory [36, 37] relates halo currents to the plasma surface currents. The last ones are studied in Chapter 4 in the presence of the resistive wall with an emphasis on their interplay with wall eddy currents.

II. FORMULATION OF THE PROBLEM

2.1. Geometry and initial set of the equations

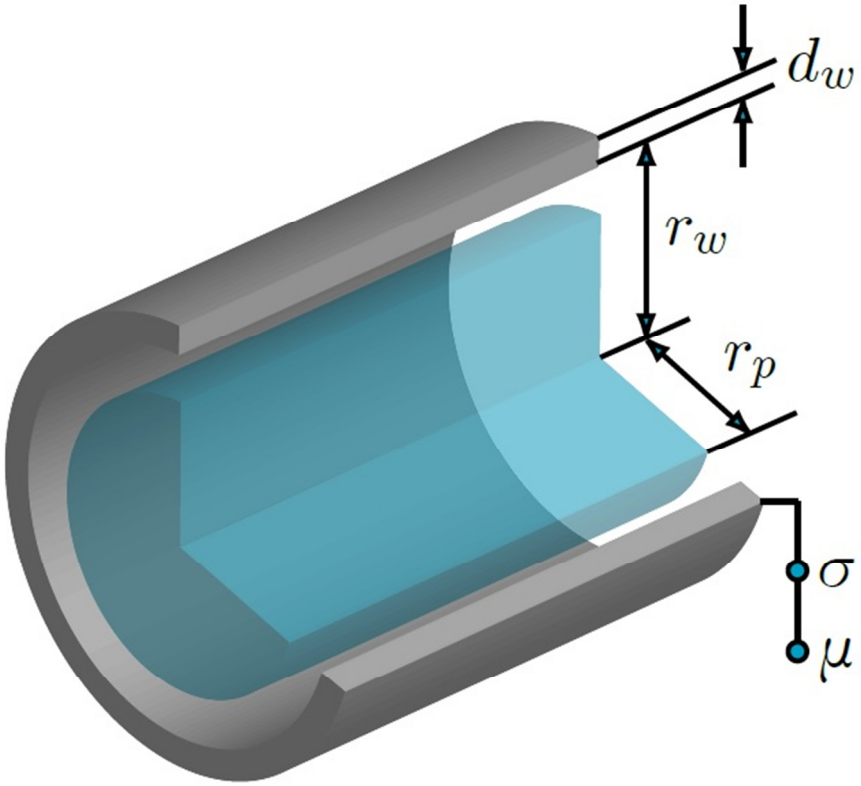

Fig. 2.1. Configuration under study and basic notations. The plasma cylinder of radius r_a is surrounded by the coaxial conducting wall with radius r_w, finite thickness d_w and magnetic permeability μ. The plasma-wall gap and space behind the wall are treated as vacuum.

We consider a cylindrical plasma column of radius r_a separated from a coaxial resistive wall of radius r_w and thickness d_w by a vacuum gap with the space behind the wall treated as vacuum (Fig. 2.1). Dynamics of such a system is governed by sets of equations different for plasma, wall and vacuum regions, the initial state and also boundary conditions for one plasma-vacuum and two wall-vacuum interfaces complemented by restrictions at the axis and at infinity.

The Maxwell equations, which are valid in every region

$$\nabla \times \mathbf{E} = -\frac{\partial \mathbf{B}}{\partial t}, \tag{2.1}$$

$$\nabla \cdot \mathbf{B} = 0, \tag{2.2}$$

$$\nabla \times \mathbf{H} = \mathbf{j}, \tag{2.3}$$

$$\mathbf{B} = \mu \mathbf{H} \tag{2.4}$$

are supplemented for the wall region by Ohm's law for a solid conductor

$$\eta_w \mathbf{j} = \mathbf{E}, \tag{2.5}$$

and for the plasma region by generalized Ohm's law, motion equation, continuity equation and entropy conservation law

$$\eta_{pl} \mathbf{j} = \mathbf{E} + \mathbf{v} \times \mathbf{B}, \tag{2.6}$$

$$\rho \frac{d\mathbf{v}}{dt} = -\nabla p + \mathbf{j} \times \mathbf{B} - div\vec{\vec{\pi}} + \mathbf{f}, \tag{2.7}$$

$$\frac{\partial \rho}{\partial t} + \nabla \cdot (\rho \mathbf{v}) = 0, \tag{2.8}$$

$$\frac{dp}{dt} + \Gamma p \nabla \cdot \mathbf{v} = 0, \tag{2.9}$$

with

$$\frac{d}{dt} = \frac{\partial}{\partial t} + \mathbf{v} \cdot \nabla. \tag{2.10}$$

Here $\mathbf{E}$, $\mathbf{H}$, $\mathbf{B}$, $\mathbf{j}$, $\mathbf{v}$, ρ and p are the electric field, magnetic field, magnetic induction, current density, velocity, mass density and pressure, respectively, μ is the magnetic permeability, η_w and η_{pl} are the wall and plasma resistivity, Γ is the ratio of specific heats, $\vec{\vec{\pi}}$ is the viscous stress tensor and the term $\mathbf{f}$ contains all forces not included in the first three terms on the right hand side of Eq. (2.7).

The boundary conditions at the two wall-vacuum interfaces are

$$\langle \mathbf{n} \cdot \mathbf{B} \rangle = 0, \qquad \langle \mathbf{n} \times \mathbf{H} \rangle = 0, \tag{2.11}$$

where $\mathbf{n}$ is the unit normal and the brackets mean the jump across the surface. While for the plasma-vacuum interface one has to apply

$$\langle \mathbf{n} \cdot \mathbf{B} \rangle = 0, \qquad \left\langle p + \frac{\mathbf{B}^2}{2\mu_0} \right\rangle = 0 \tag{2.12}$$

To solve the problem one needs also to know the initial profiles for all quantities in Eqs. (2.1-2.9) including viscosity coefficients and explicitly determine the term $\mathbf{f}$, which can include, for example, the interaction with neutral gas and/or fast particles from NBI.

In practice, however, it hardly can be done even numerically, since the task in such formulation is rather complicated. So we are forced to make a model from Eqs. (2.1-2.9), which being resistive MHD equations is already a simplification with its own limits of applicability. Step by step we describe the assumptions we make.

2.2. Linear analysis

Let us consider a configuration with such spatial distribution of all quantities $\mathbf{X_0(r)}$ entering equations (2.1)-(2.9) that plasma is stable, that is what we call equilibrium state. In the linear analysis we add small perturbations $\mathbf{x}_1(\mathbf{r},t)$, which are always present in the real machine, and see how the system evolves in time

$$\mathbf{X}(\mathbf{r},t)=\mathbf{X_0}(\mathbf{r})+\mathbf{x}_1(\mathbf{r},t). \tag{2.13}$$

In the cylindrical approximation

$$\frac{nr_a}{mR}<<1, \tag{2.14}$$

one can consider single harmonics

$$\mathbf{x}_1(\mathbf{r},t)=\mathrm{Re}\left[\ \mathbf{x_{mk}}(r)\exp(im\theta+ik_z z+i\gamma)\right], \tag{2.15}$$

$$\gamma=\gamma_R+in\omega, \tag{2.16}$$

where (r,θ,z) are the cylindrical coordinates, t is the time, γ_R and ω are the growth rate and the mode angular rotation frequency, $k_z=-n/R$ with $2\pi R$ the length of the equivalent torus, m and n are the poloidal and toroidal mode number.

If $\mathbf{X_0(r)}$ are assumed to be known (in practice, however, they are known roughly), equations (2.1)-(2.9) with boundary conditions (2.11), (2.12) allow us (in principle) to predict dynamics of different harmonics (m,n). If $\gamma_R>0$, then this particular equilibrium is unstable for this mode (m,n) and vice versa.

2.3. Equilibrium state

Hereinafter we assume that the whole system is immersed in the strong uniform longitudinal magnetic field $B_{0,z}(r)=B_z$. The poloidal field B_θ, such that

$$B_\theta<<B_z \tag{2.17}$$

is created by the plasma current of the form

$$\mathbf{j}_0=j_0\left(1-\alpha\frac{r^2}{r_a^2}\right)\cdot\mathbf{e_z}, \tag{2.18}$$

where $\mathbf{e}_z$ is the unit vector along ∇z and j_0 is the current density at the axis. Parameter α is negative for hollow current profile, $\alpha = 0$ for flat and $\alpha = 1$ for purely parabolic one.

To be noticed is that to analyse the external (with respect to the plasma) part of the problem one has to know only the complex growth rate γ , without making any assumptions about the plasma. We take advantage of this fact to calculate eddy currents in the resistive wall and the electromagnetic torque acting on the plasma.

III. EXTERNAL WITH RESPECT TO THE PLASMA PART OF THE PROBLEM

The presence of nearby conducting wall can improve the plasma stability [9, 10, 15, 16, 38-48]. While the plasma may be treated in a variety of ways, the solutions in the vacuum gap, resistive wall and external vacuum remain always the same. Let us solve this external part of the problem first, and then we will use these results for matching with different plasmas.

3.1. Vacuum regions

For straight tokamak (2.14), (2.17), from (2.2) it follows that

$$\mathbf{b} = \nabla\psi \times \mathbf{e}_z, \tag{3.1}$$

where ψ is the perturbed poloidal magnetic flux. Then, in vacuum regions we obtain from the Amper's law

$$\Delta\psi = 0. \tag{3.2}$$

Its solution in the vacuum gap is

$$\psi_g \propto C_g (r/r_w)^m + (r/r_w)^{-m}, \tag{3.3}$$

while for the outer vacuum it gives

$$\psi_{out} \propto C_{out}\left[r/(r_w + d_w)\right]^{-m}, \tag{3.4}$$

since at the infinity ψ_{out} has to be finite. Here C_g and C_{out} are constants.

3.2. Resistive ferromagnetic wall region

Ferritic steel is a possible candidate for the blanket components of future fusion reactors [10, 48-50], that is why we assume also that the wall has the uniform magnetic permeability μ different from the vacuum one μ_0. From (2.1), (2.3), (2.4), (2.5) with (3.1) we obtain [24, 51]

$$\mu\sigma_w \frac{\partial\psi}{\partial t} = \Delta\psi, \tag{3.5}$$

where $\sigma_w = 1/\eta_w$ is the wall conductivity.

The solution of the last equation is a superposition of modified Bessel functions

$$\psi_w = gI_m(y) + hK_m(y), \tag{3.6}$$

where

$$y = \sqrt{\hat{\mu}\tau_{sk}\gamma}\,\frac{r}{d_w}, \tag{3.7}$$

with the wall skin time determined by

$$\tau_{sk} = \mu_0 \sigma_w d_w^2, \tag{3.8}$$

$$\hat{\mu} = \mu / \mu_0, \tag{3.9}$$

g and h are constants.

3.3. Wall-vacuum boundary conditions and matching

Applying boundary conditions (2.11) for two wall-vacuum interfaces we can match solutions in the wall and two vacuum regions [52, 53]

$$\left.\frac{r\psi_g'}{\psi_g}\right|_{w-} = -\Gamma_m - m, \tag{3.10}$$

where subscript $w\_$ means that the ratio has to be calculated at the inner side of the wall,

$$\Gamma_m = \frac{y_i}{\hat{\mu}}\frac{hK_{m-1}(y_i) - gI_{m-1}(y_i)}{hK_m(y_i) + gI_m(y_i)} - m\frac{\hat{\mu}-1}{\hat{\mu}}, \tag{3.11}$$

$$\frac{g}{h} = \frac{y_e K_{m-1}(y_e) - m(\hat{\mu}-1)K_m(y_e)}{y_e I_{m-1}(y_e) + m(\hat{\mu}-1)I_m(y_e)}, \tag{3.12}$$

$$y_i \equiv r_w\sqrt{\mu\sigma\gamma} \text{ and } y_e \equiv y_i(1 + d_w / r_w). \tag{3.13}$$

For $\hat{\mu} = 1$, (3.11) reduces to

$$\Gamma_m = y_i \frac{K_{m-1}(y_i)I_{m-1}(y_e) - I_{m-1}(y_i)K_{m-1}(y_e)}{K_m(y_i)I_{m-1}(y_e) + I_m(y_i)K_{m-1}(y_e)}. \tag{3.14}$$

The expression (3.11) can be simplified for two limit cases of weak and strong skin effect. If the skin depth s determined by

$$\frac{1}{s} = \mathrm{Re}\sqrt{\mu\sigma\gamma} \tag{3.15}$$

is much bigger than the wall thickness $s >> d_w$ and $\hat{\mu} << r_w/(md_w)$, then from (3.11) we obtain

$$\Gamma_m = \gamma\tau_w - m^2\frac{d_w}{r_w}\frac{\hat{\mu}^2 - 1}{\hat{\mu}}, \tag{3.16}$$

with the wall time given by

$$\tau_w = \mu_0 \sigma_w d_w r_w . \tag{3.17}$$

For $\hat{\mu} = 1$ (3.16) reduces to

$$\Gamma_m = \gamma \tau_w . \tag{3.18}$$

In the opposite limit $s << d_w$, from (3.11) we find

$$\Gamma_m = \frac{r_w}{d_w} \sqrt{\frac{\gamma \tau_{sk}}{\hat{\mu}}} - m \frac{\hat{\mu} - 1}{\hat{\mu}} . \tag{3.19}$$

For $\hat{\mu} = 1$ (3.19) reduces to

$$\Gamma_m = \frac{r_w}{d_w} \sqrt{\gamma \tau_{sk}} . \tag{3.20}$$

For magnetically thin resistive wall one can use constant-ψ approximation within the wall, in this case Γ_m is an analogue of the tearing mode parameter Δ' and gives the jump of the logarithmic derivative of the perturbed poloidal magnetic flux across the wall.

3.4. Magnetic perturbation in the vacuum gap

From (3.3) it follows that

$$\left. \frac{r \psi_g'}{\psi_g} \right|_{w-} = -m + 2m \frac{C_g}{1 + C_g} , \tag{3.21}$$

with (3.10) it gives

$$C_g = -\frac{\Gamma_m}{2m + \Gamma_m} . \tag{3.22}$$

With (3.22) the matching condition at the plasma boundary

$$\left. \frac{r \psi_g'}{\psi_g} \right|_{a+} = -m + 2m \frac{C_g (r_a / r_w)^{2m}}{1 + C_g (r_a / r_w)^{2m}} , \tag{3.23}$$

takes the form

$$\left. \frac{r \psi_g'}{\psi_g} \right|_{a+} = -m \frac{2m + \Gamma_m \left[1 + (r_a / r_w)^{2m} \right]}{2m + \Gamma_m \left[1 - (r_a / r_w)^{2m} \right]} , \tag{3.24}$$

where the subscript a_+ refers to the outer side of the plasma-vacuum interface.

To be noticed is that for the case of ideal wall the radial component of the magnetic field has to be zero at the inner side of the wall $b_r(r_w)=0$, then from (3.3) we find $C_g=-1$, taking it into account we have

$$\psi'_g(r_w)=\frac{\Gamma_m+m}{\Gamma_m+2m}\psi'_{g,id}(r_w), \tag{3.25}$$

where $\psi'_{g,id}(r_w)$ is the value of $\psi'_g(r_w)$ for the ideal wall. The ratio on the RHS varies from 0.5 for no wall ($\Gamma_m=0$) to 1 for the ideal wall ($\Gamma_m=\infty$).

Plasma-wall interaction plays an important role in the stability problem. That is why we want to have a closer look at the behaviour of magnetic perturbation in the vacuum gap for different parameters of the mode and the wall. In Figs. 3.1-3.4 radial b_r and poloidal b_θ components are represented in terms of the poloidal flux ψ. As it follows from (3.1)

$$b_r=im\psi/r \text{ and } b_\theta=-\psi'. \tag{3.26}$$

The drop of the amplitudes across the vacuum gap

$$\frac{\psi_g(r_w)}{\psi_g(r_a)}=\left(\frac{r_a}{r_w}\right)^m\frac{2m}{2m+\Gamma_m\left[1-(r_a/r_w)^{2m}\right]}, \tag{3.27}$$

$$\frac{\psi'_g(r_w)}{\psi'_g(r_a)}=\left(\frac{r_a}{r_w}\right)^{m+1}\frac{2m+2\Gamma_m}{2m+\Gamma_m\left[1+(r_a/r_w)^{2m}\right]}, \tag{3.28}$$

is shown as a function of the growth rate for locked modes ($\omega=0$) in Fig.3.1 and as a function of the mode rotational frequency for marginally stable modes ($\gamma_R=0$) in Fig. 3.2. With respect to $\gamma_R=0$ (or $\omega=0$) case, for faster modes the radial component at the wall becomes smaller, while the poloidal one increases. For locked modes (Fig. 3.1), with higher m both components decrease, for marginally stable rotating modes this dependence is more complicated, as can be seen in Fig. 3.2. Both figures indicate that even for modes with high m, for example $m=10$, plasma wall interaction must be strong, indeed, as it was shown in Ref. [54] it can provide stabilization for sufficiently fast rotating modes. The same dependencies are plotted in Fig. 3.3 for the wall with different magnetic permeability. As it follows from (3.16) the curves are split already at $\gamma=0$, which means the negative shift of the stability boundary with increase of $\hat{\mu}$, see Ref. [55] for more detail. For larger $\hat{\mu}$, the radial component increases and the poloidal one becomes smaller.

In Fig. 3.4 one can see how the magnetic perturbation at the inner side of the wall depends on the plasma-wall separation for the modes growing on the wall time scale $\gamma\tau_w = 1$, and much faster instabilities, for which the skin effect in the wall becomes notable $\gamma\tau_{sk} = 1$. Closer is the wall, smaller is the drop of the field across the vacuum gap.

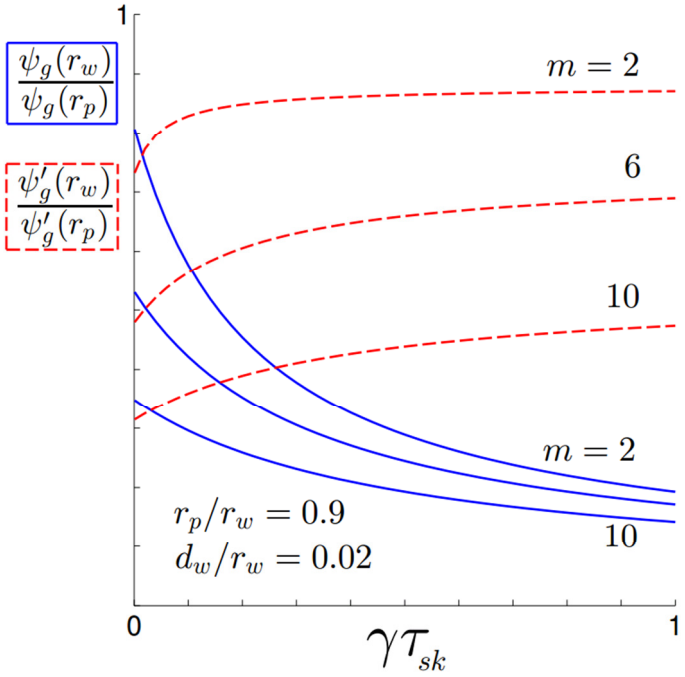

Fig. 3.1. The $\psi_g(r_w)/\psi_g(r_a)$ (solid lines) and $\psi_g'(r_w)/\psi_g'(r_a)$ (dashed) versus the growth rate $\gamma = \gamma_R$ normalized to the wall skin time τ_{sk} for locked modes with m=2, 6 and 10. The wall position r_a / r_w =0.9.

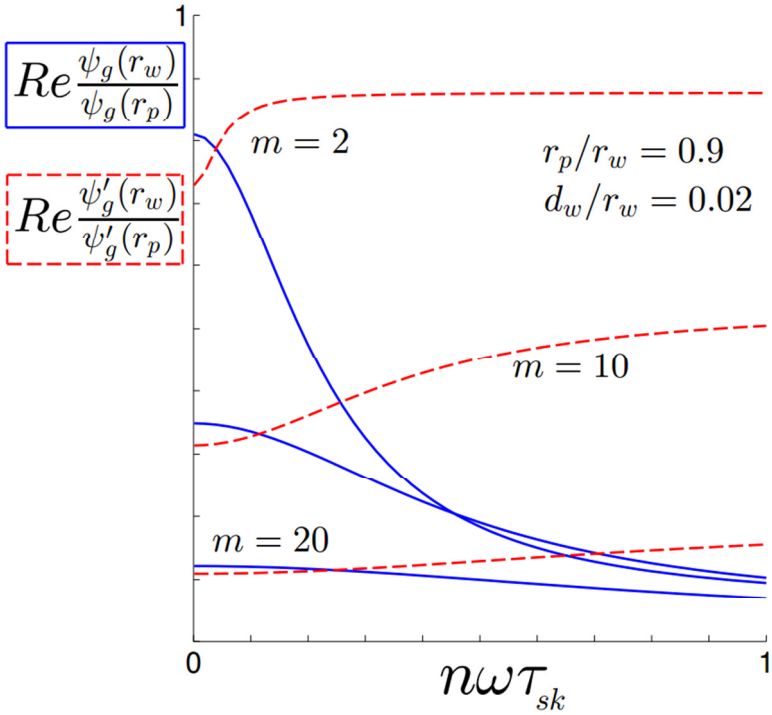

Fig. 3.2. The real part of $\psi_g(r_w)/\psi_g(r_a)$ (solid lines) and $\psi_g'(r_w)/\psi_g'(r_a)$ (dashed) versus the mode frequency $n\omega$ normalized to the wall skin time τ_{sk} for marginally stable modes with m=2, 10 and 20. The wall position r_a / r_w =0.9.

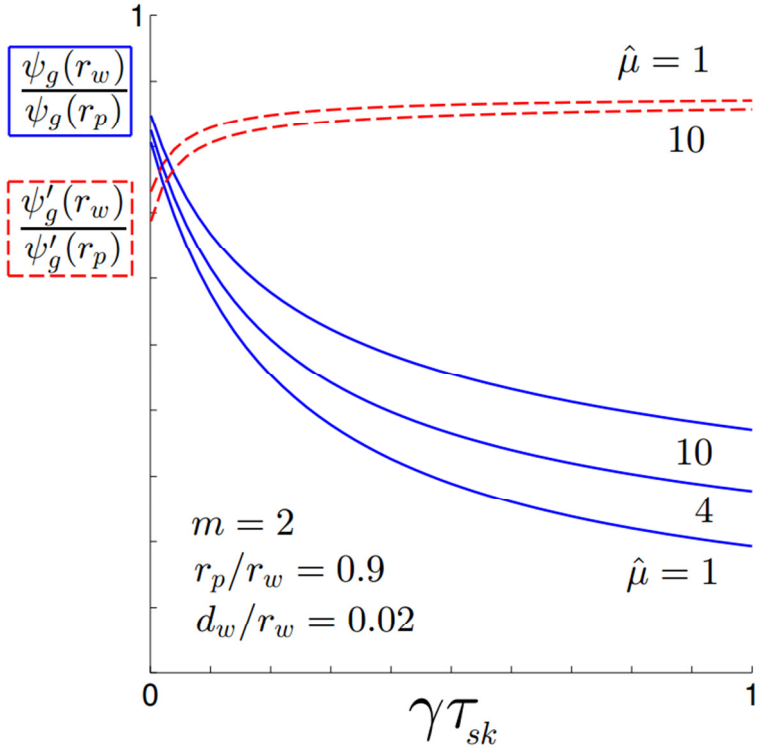

Fig. 3.3. The $\psi_g(r_w)/\psi_g(r_a)$ (solid lines) and $\psi_g'(r_w)/\psi_g'(r_a)$ (dashed) versus the growth rate $\gamma = \gamma_R$ normalized to the wall skin time τ_{sk} for $m/n = 2/1$ locked mode and the wall with $\hat{\mu} = 1$, 4 and 10 located at r_a/r_w =0.9.

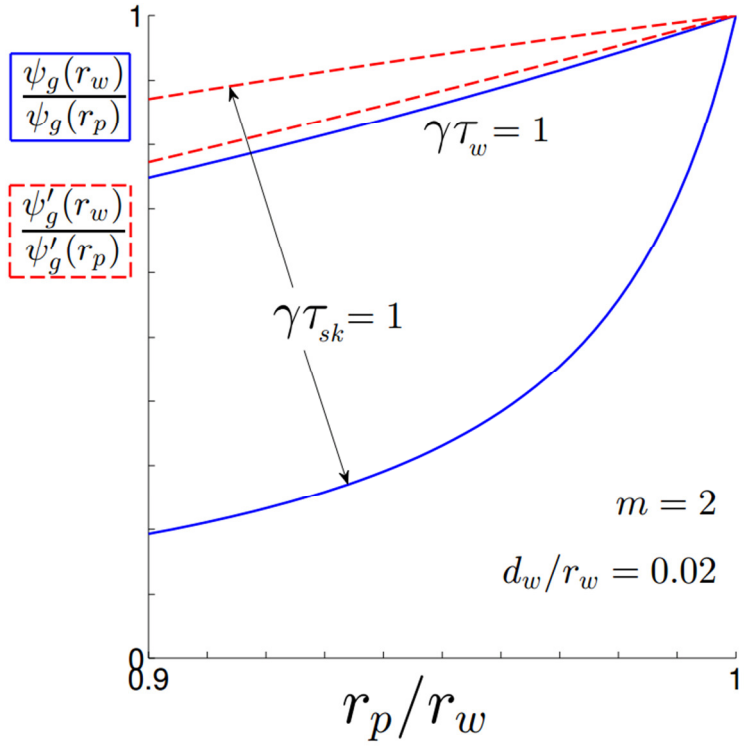

Fig. 3.4. The $\psi_g(r_w)/\psi_g(r_a)$ (solid lines) and $\psi_g'(r_w)/\psi_g'(r_a)$ (dashed) versus the wall position for $m/n = 2/1$ locked modes with the growth rates such that $\gamma\tau_w = 1$ and $\gamma\tau_{sk} = 1$.

3.5. The force produced by eddy currents

As a response to external magnetic perturbations the wall generates eddy currents $\mathbf{j}_{eddy}$. For geometrically thin wall, $d_w << r_w$, local volume density of the corresponding force acting on the vacuum vessel is

$$\mathbf{f}_{eddy} = \int_{w-}^{w+} \mathbf{F}_{eddy}\, dr = \int_{w-}^{w+} \mathbf{j}_{eddy} \times \mathbf{B}_0\, dr = \left[\mathbf{e_r} \times \mathbf{H_1}\Big|_{w-}^{w+}\right] \times \mathbf{B}_0 = -(\mathbf{B}_0 \cdot \mathbf{H_1}\Big|_{w-}^{w+})\mathbf{e}_r\,, \tag{3.29}$$

where w_- and w_+ mean internal and external radius of the wall, respectively.

In vacuum

$$\mathbf{H}_1 = \nabla\varphi\,, \tag{3.30}$$

hence

$$H_{1,z} = -\frac{nr}{mR} H_{1,\theta}\,, \tag{3.31}$$

and

$$f_r \equiv \mathbf{f}_{eddy} \cdot \mathbf{e}_r = -B_{0,\theta}(1 - nq_w/m) H_{1,\theta}\Big|_{w-}^{w+}, \tag{3.32}$$

where

$$q_w \equiv q(r_w)\,, \tag{3.33}$$

and the safety factor q is determined in the cylindrical geometry by

$$q \equiv \frac{rB_z}{RB_\theta}\,. \tag{3.34}$$

From (2.4), (2.11) and (3.26) we find

$$H_{\mathbf{1},\theta}\Big|_{w-}^{w+} = -\frac{\psi'_w}{\mu}\Big|_{w-}^{w+} = \frac{\psi'_g(r_w)}{\mu_0}\left(1 - \frac{\psi'_w(r_w + d_w)}{\psi'_w(r_w)}\right). \tag{3.35}$$

From (3.6) it follows that

$$\frac{\psi'_w(r_w + d_w)}{\psi'_w(r_w)} = \frac{gI'_m(y_e) + hK'_m(y_e)}{gI'_m(y_i) + hK'_m(y_i)}\,, \tag{3.36}$$

and (3.3) with (3.22) gives

$$\psi'_g(w_-) = \psi'_{g,id}(w_-)\frac{\Gamma_m + m}{\Gamma_m + 2m}\,, \tag{3.37}$$

where $\psi'_{g,id}(w_-)$ is $\psi'_g(w_-)$ at $C_g = -1$ ($\Gamma_m = \infty$), which corresponds to the ideal wall. The maximum of the force f_r is reached at $|\gamma| \to \infty$

$$f_r^{\max} = -\frac{B_{0,\theta}\psi'_{g,id}(w_-)}{\mu_0}(1-nq_w/m), \tag{3.38}$$

then for the normalized force we have

$$f_N \equiv \frac{f_r}{f_r^{\max}} = \frac{\Gamma_m + m}{\Gamma_m + 2m}\left(1 - \frac{gI'_m(y_e) + hK'_m(y_e)}{gI'_m(y_i) + hK'_m(y_i)}\right). \tag{3.39}$$

In Fig. 3.5 this quantity is plotted versus the growth rate normalized on the wall skin time τ_{sk} for the wall with $\hat{\mu} = 1$, 10 and 100. While it decreases for larger $\hat{\mu}$, for the values relevant to the fusion reactors ($\hat{\mu} = 1-4$) the effect is negligible.

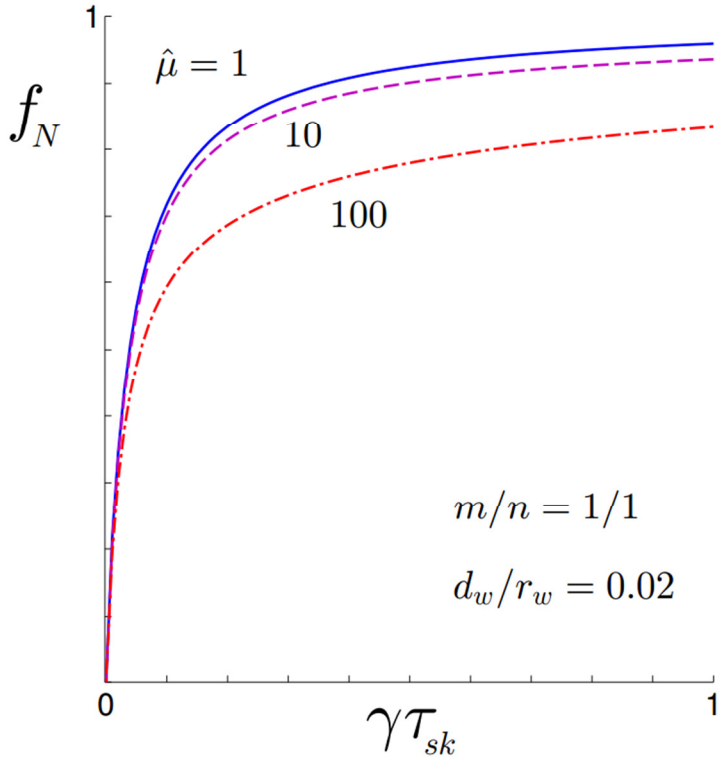

Fig. 3.5. The normalized eddy force amplitude versus the growth rate $\gamma = \gamma_R$ normalized to the wall skin time τ_{sk} for $m/n = 1/1$ locked mode and the wall with $\hat{\mu} = 1$, 10 and 100.

As was shown in [56] the sideways force calculated within simplified single-mode analysis is proportional to f_N, therefore, it has to be maximal for the ideal wall. In contrast, the recent analytical theory [26, 57] based on the first principles predicts the contrary, zero sideways force for the ideal wall and the peak of load for $\gamma\tau_w \approx 1$. Numerical simulations in [33, 34] also give the largest sideways force for perturbations developing on the wall time scale, $\gamma\tau_w \approx 1$.

IV. IDEAL PLASMA

4.1. Reduction of RMHD equations

In our analysis we neglect viscosity and the term $\mathbf{f}$ in the equation of motion (2.7)

$$\rho \frac{d\mathbf{v}}{dt} = -\nabla p + \mathbf{j}\times\mathbf{B}. \tag{4.1}$$

Linearizing (4.1), in the absence of equilibrium flow, $\mathbf{v}_0 = 0$, we find that

$$\rho_0 \gamma^2 \boldsymbol{\xi} = -\nabla p_1 + \mathbf{j}_1 \times \mathbf{B}_0 + \mathbf{j}_0 \times \mathbf{b}, \tag{4.2}$$

where the perturbed plasma displacement $\boldsymbol{\xi}$ is defined by the relation

$$\mathbf{v}_1 \equiv \frac{d\boldsymbol{\xi}}{dt}. \tag{4.3}$$

Using (2.1) and (2.6) with $\eta_{pl} = 0$, we obtain the connection between $\mathbf{b}$ and $\boldsymbol{\xi}$:

$$\mathbf{b} = \nabla\times(\boldsymbol{\xi}\times\mathbf{B}_0). \tag{4.4}$$

Radial component of the above equation is

$$b_r = iF\xi_r, \tag{4.5}$$

where

$$F \equiv \frac{m}{r}B_\theta + k_z B_z = \frac{mB_z}{R}(\tilde{\mu} - n/m), \tag{4.6}$$

and

$$\tilde{\mu} = 1/q. \tag{4.7}$$

Allowing for (4.4), (2.8), (2.9), in the large-aspect-ratio approximation (2.14), (2.17), from (4.2), one can obtain differential equation for the radial displacement ξ_r [4]

$$\frac{1}{r}\frac{\partial}{\partial r}\left[r^3(F^2 + \mu_0\rho_0\gamma^2)\xi_r'\right] - \left\{U + \mu_0\gamma^2\left[\rho_0(m^2-1) - r\rho_0'\right]\right\}\xi_r = 0, \tag{4.8}$$

where

$$U = (m^2 - 1 + k_z^2 r^2)F^2 + 2k_z^2 r p_0' + \frac{2k_z^2}{m^2}(r^2 k_z^2 B_z^2 - m^2 B_\theta^2). \tag{4.9}$$

At the stability boundary, $\gamma = 0$, (4.8) has a singular point, $r = r_s$, where $F(r_s) = 0$. For internal modes $r_s < r_a$, and $r_s > r_a$ for external ones. The terms with k_z in (4.9) are small, in our analysis of external modes with $m > 1$ we neglect them. Then (4.8) reduces to

$$\frac{1}{r}\frac{\partial}{\partial r}\left[r^3(F^2+\mu_0\rho_0\gamma^2)\xi_r'\right]-\left\{(m^2-1)F^2+\mu_0\gamma^2\left[\rho_0(m^2-1)-r\rho_0'\right]\right\}\xi_r=0. \qquad (4.10)$$

4.2. Plasma-vacuum boundary conditions

Integrating (4.10) across the plasma-vacuum boundary allowing for the continuity of $b_r(a)$ we arrive at the matching condition of the form

$$\left[\ln\left(\frac{b_r}{\tilde{\mu}-n/m}\right)\right]'\Bigg|_{a+}=\left\{(\ln\xi_r)'+\left(\frac{\tilde{\gamma}}{m\tilde{\mu}-n}\right)^2\left[\ln(r\xi_r)\right]'\right\}\Bigg|_{a-}, \qquad (4.11)$$

where

$$\tilde{\gamma}=\hat{\tau}_A\gamma, \qquad (4.12)$$

$$\hat{\tau}_A\equiv R\tau_A/a, \qquad (4.13)$$

with Alfvén transient time determined by

$$\tau_A\equiv\frac{a\sqrt{\mu_0\rho_0}}{B_z}. \qquad (4.14)$$

The subscripts $a-$ and $a+$, refer to the inner and outer sides of the plasma-vacuum interface, respectively.

4.3. Dispersion relation for ideal external kink modes

Allowing for the fact that in the vacuum gap

$$\tilde{\mu}=\tilde{\mu}_a(r_a/r)^2, \qquad (4.15)$$

where $\tilde{\mu}_a=\tilde{\mu}(r_a)$, by means of (3.26) and (3.24), (4.11) reduces to

$$\tilde{\gamma}^2\left[r\ln(r\xi_r)\right]'\Big|_{a-}=m^2(\tilde{\mu}_a-n/m)^2\left[\frac{2\tilde{\mu}_a}{\tilde{\mu}_a-n/m}-m-1-\frac{2m\Gamma_m(r_a/r_w)^{2m}}{2m+\Gamma_m\left[1-(r_a/r_w)^{2m}\right]}-r(\ln\xi_r)'\Big|_{a-}\right]. \qquad (4.16)$$

This is the dispersion relation for ideal plasma resistive wall external modes.

4.4. Ideal wall and no wall stability limits

Let us determine the stability boundaries with the ideal wall and without any wall. Since $\left[\ln f(x)\right]'>0$, from (4.16) it follows that the instability condition, $\gamma_R>0$, is

$$\frac{2\tilde{\mu}_a}{\tilde{\mu}_a - n/m} - m - 1 - \frac{2m\Gamma_m (r_a / r_w)^{2m}}{2m + \Gamma_m \left[1 - (r_a / r_w)^{2m}\right]} - r(\ln \xi_r)'\big|_{a-} > 0, \tag{4.17}$$

where $\Gamma_m = \infty$ for the ideal wall, and $\Gamma_m = 0$ for the no wall case.

4.5. Flat current profile

For flat current and density profiles solution of equation (4.10) which is finite for $r = 0$ is

$$\xi_r \propto (r/a)^{m-1}. \tag{4.18}$$

Substituting (4.18) into (4.16), we arrive at the dispersion relation

$$\tilde{\gamma}^2 = 2\frac{(m - nq_a)}{q_a^2}\left(1 - \frac{(m - nq_a)(1 + 2m/\Gamma_m)}{1 - (r_a / r_w)^{2m} + 2m/\Gamma_m}\right), \tag{4.19}$$

where $q_a = 1/\tilde{\mu}_a$.

The instability conditions, $\gamma_R > 0$, are given by

$$(m - nq_a)\left[1 - (m - nq_a)\right] > 0, \tag{4.20}$$

for no wall, $\Gamma_m = 0$, and by

$$(m - nq_a)\left[1 - (r_a / r_w)^{2m} - (m - nq_a)\right] > 0. \tag{4.21}$$

for the ideal wall, $\Gamma_m \to \infty$.

The solutions of the (4.19) are shown in Figs. 4.1 for different positions of the ideal wall. By putting the ideal wall closer to the plasma we shrink the range of nq_a where the instability can exist. If we replace the ideal wall with a wall of a finite conductivity, the stability limits become the same as for the no wall case, but in the wide range of nq_a, such that $m - 1 < nq_a < m - 1 + (a/b)^{2m}$, the time scale on which the instability develops increases from $\hat{\tau}_A = 10^{-6} - 10^{-7}$ s to $\tau_w = 10^{-3} - 10^{-1}$ s. This can be seen in Fig. 4.2, where solid curves represent the growth rate normalized on the wall time τ_w (in contrast to Fig. 4.1 with normalization to $\hat{\tau}_A$) as a function of the edge safety factor for different resistive wall positions, the vertical dashed lines indicate corresponding ideal wall stability limits.

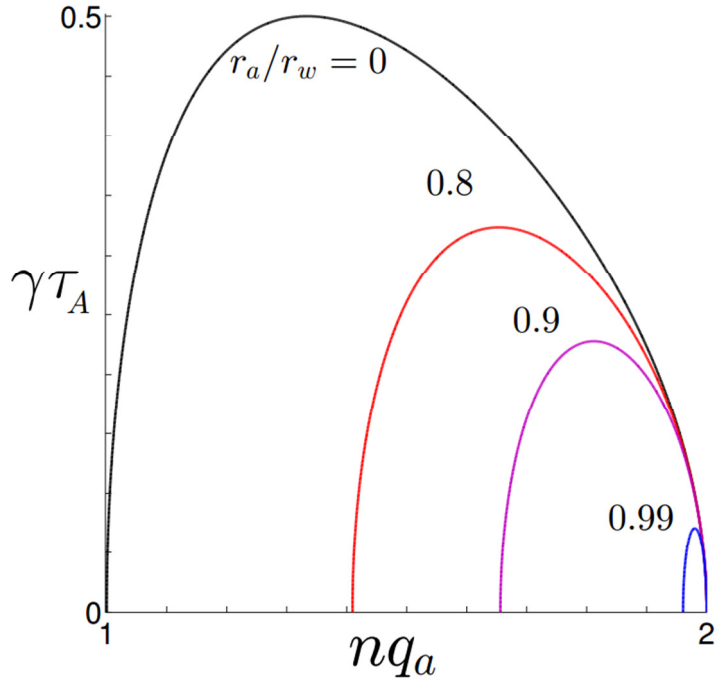

Fig. 4.1. The growth rate $\gamma = \gamma_R$ normalized to $\hat{\tau}_A$ versus edge safety factor nq_a calculated by Eq. (4.19) for $m=2$ mode. The no wall case – the uppermost curve, ideal wall at r_a/r_w =0.8, 0.9 and 0.99 - red, purple and blue line, respectively.

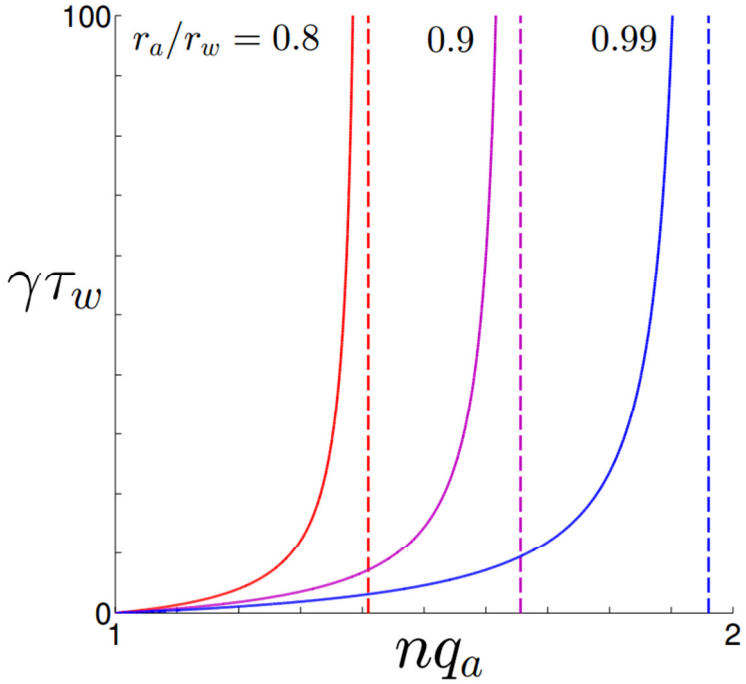

Fig. 4.2. The growth rate (solid curves) $\gamma = \gamma_R$ normalized to the wall time τ_w versus edge safety factor nq_a calculated by Eq. (4.19) for $m=2$ mode. From left to right, the wall at r_a/r_w =0.8, 0.9 and 0.99. Vertical dashed lines designate corresponding ideal stability limits. We also assumed $\tau_w/\hat{\tau}_A = 5\cdot 10^4$ and $d_w/r_w = 0.02$.

4.6. Plasma surface currents

Plasma surface currents are determined by the jump of the magnetic field across perturbed plasma-vacuum interface [58]

$$\mu_0 \mathbf{i}^{surf} = \mathbf{n} \times (\mathbf{B}_{gap} - \mathbf{B}_{pl}) \Big| = \mathbf{n} \times (\mathbf{b} + \boldsymbol{\xi} \cdot \nabla \mathbf{B}_0) \Big|_{a-}^{a+}, \tag{4.22}$$

where, $\mathbf{n}$ is the unit normal to the perturbed surface, $\mathbf{B}_{gap}$ and $\mathbf{B}_{pl}$ are magnetic fields adjacent to the perturbed plasma's surface from the side of vacuum gap and plasma, respectively. The toroidal component of the above equation is

$$\mu_0 i_z^{surf} = (b_\theta + \xi_r B_\theta') \Big|_{a-}^{a+}. \tag{4.23}$$

By means of (4.5), (3.26) and (4.11), from (4.23) we find

$$\mu_0 i_z^{surf} = -\psi_a \left[\ln \frac{\psi}{\tilde{\mu} - n/m} \right]' \Bigg|_{a-}^{a+} = -\psi_a \frac{\tilde{\gamma}^2}{\tilde{\gamma}^2 + (\tilde{\mu} - n/m)^2} \left[\ln \frac{\psi}{\tilde{\mu} - n/m} \right]' \Bigg|_{a+}, \tag{4.24}$$

where $\psi_a \equiv \psi(r_a)$. Finally, allowing for (4.15) and (3.24) we arrive at

$$\mu_0 i_z^{surf} = \frac{B_z}{R} \frac{\tilde{\gamma}^2}{\tilde{\gamma}^2 + (\tilde{\mu}_a - n/m)^2} \left[-2\tilde{\mu}_a + m(\tilde{\mu}_a - n/m) \frac{2m + \Gamma_m \left[1 + (r_a / r_w)^{2m} \right]}{2m + \Gamma_m \left[1 - (r_a / r_w)^{2m} \right]} \right] \xi_a, \tag{4.25}$$

where $\xi_a \equiv \xi_r(r_a)$. For the ideal wall, $\Gamma_m = \infty$, the last expression reduces to

$$\mu_0 i_z^{surf,id} = \frac{B_z}{R} \frac{\tilde{\gamma}^2}{\tilde{\gamma}^2 + (\tilde{\mu}_a - n/m)^2} \left[-2\tilde{\mu}_a + m(\tilde{\mu}_a - n/m) \frac{1 + (r_a / r_w)^{2m}}{1 - (r_a / r_w)^{2m}} \right] \xi_a \tag{4.26}$$

4.7. Eddy currents in the wall

Toroidal component of eddy current for geometrically thin wall, $d_w << r_w$, is determined by

$$i_z^{eddy} = \int_{w-}^{w+} j_{1,z} \, dr = H_{1,\theta} \Big|_{w-}^{w+}. \tag{4.27}$$

By means of (3.24), (3.28), (3.35) and (4.5), from (4.27) we find that

$$\mu_0 i_z^{eddy} = -\frac{2mB_z}{R} (\tilde{\mu}_a - n/m) \left(\frac{r_a}{r_w} \right)^{m+1} \frac{m + \Gamma_m}{2m + \Gamma_m \left[1 - (r_a / r_w)^{2m} \right]} \left(1 - \frac{\psi_w'(r_w + d_w)}{\psi_w'(r_w)} \right) \xi_a. \tag{4.28}$$

For the ideal wall, $\Gamma_m = \infty$ and $\psi'_w(r_w + d_w) = 0$, then the last expression reduces to

$$\mu_0 i_z^{eddy} = -\frac{2mB_z}{R}\frac{\tilde{\mu}_a - n/m}{1-(r_a/r_w)^{2m}}\left(\frac{r_p}{r_w}\right)^{m+1}\xi_a \tag{4.29}$$

4.8. Comparison of eddy and plasma surface currents

Let us compare eddy and surface currents for the flat current profile, for this case the growth rate is determined by (4.19). In Figs. 4.3 and 4.4 normalized quantities

$$i_N^{eddy} = \frac{\mu_0 R}{B_z \xi_a} i_z^{eddy}, \tag{4.30}$$

$$i_N^{surf} = \frac{\mu_0 R}{B_z \xi_a} i_z^{surf}, \tag{4.31}$$

are plotted versus edge safety factor.

The black curves show growth rate normalized to $\hat{\tau}_A$ (in Fig. 4.3) and to the wall skin time τ_{sk} (in Fig. 4.4). As far as the growth rate is small on the Alfvén time scale the surface current is negligible in comparison with the eddy current. The last one increases for faster modes. Within the ideal wall instability range indicated by vertical dashed lines in Fig. 4.4, the instability is fast enough to cause large surface current that can screen partially or totally the perturbation coming from plasma to the wall and, therefore, it makes the eddy current smaller or absent. When the rational surface is very close to the plasma edge $nq_a \approx m$, the growth rate has the wall time scale $\gamma\tau_w \approx 1$, nevertheless, the eddy current is almost zero, and the surface one reaches its maximum value. As it was shown in [37] this is a peculiarity of the flat equilibrium current profile. As we increase its parabolicity, the surface currents become smaller and for purely parabolic distribution they equal to zero at the point $nq_a = m$.

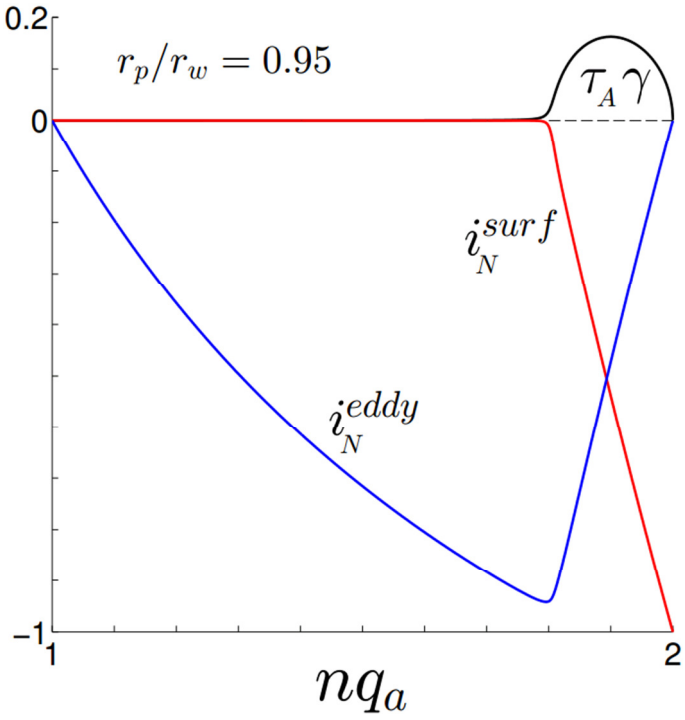

Fig. 4.3. The growth rate $\gamma = \gamma_R$ normalized to the Alfvén time τ_A (black curve), eddy (blue) and surface currents (red) versus edge safety factor nq_a for flat current profile and $m=2$ locked mode. We also assumed $r_p / r_w = 0.95$, $\tau_w / \tau_A = 5 \cdot 10^4$ and $d_w / r_w = 0.02$.

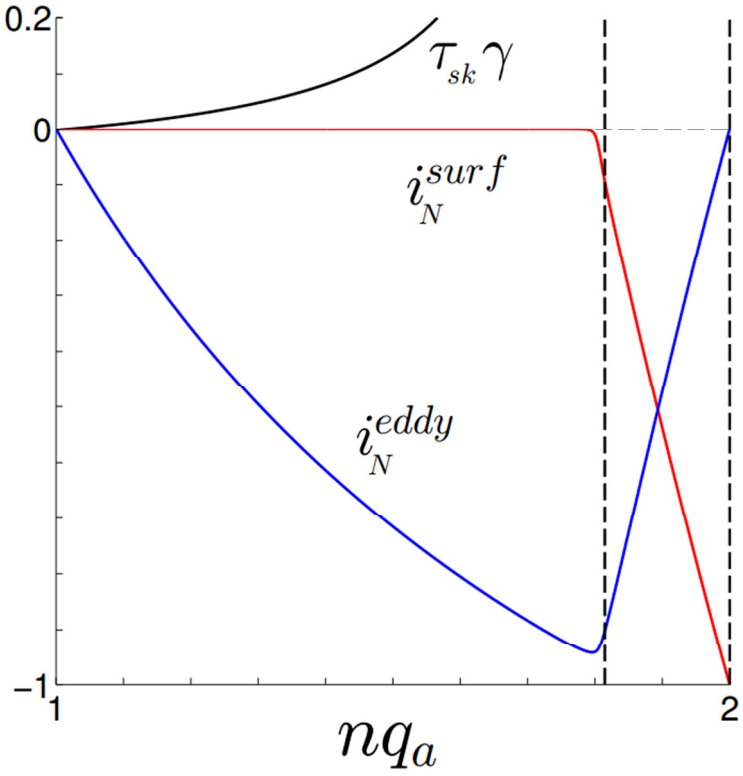

Fig. 4.4. The same plot as in Fig. 4.3, but with the growth rate normalized to the wall skin time τ_{sk}. Vertical dashed lines designate the ideal wall instability range.

4.9. Parabolic current profile

For parabolic current distribution of the form (2.18), from (4.7) we find

$$\tilde{\mu} = \tilde{\mu}_0 \left(1 - \frac{\alpha}{2} \frac{r^2}{r_a^2} \right), \tag{4.32}$$

where $\tilde{\mu}_0 = \tilde{\mu}(0)$.

As we have seen on the example of the flat current profile in the presence of the resistive wall there is a range of nq_a where $\gamma \hat{\tau}_A << 1$. We take advantage of this fact to simplify equation (4.10) to

$$\frac{1}{r} \frac{\partial}{\partial r} \left[r^3 F^2 \xi_r' \right] - (m^2 - 1) F^2 \xi_r = 0. \tag{4.33}$$

Allowing for (4.5), (3.26) and (4.6), from (4.33) we find that

$$\frac{\partial}{r \partial r} \left(r \frac{\partial \psi}{\partial r} \right) - \frac{m^2}{r^2} \psi - \frac{1}{(\tilde{\mu} - n/m)} \frac{\partial}{r \partial r} \left[\frac{\partial}{r \partial r} (r^2 \tilde{\mu}) \right] \psi = 0. \tag{4.34}$$

The above equation can be transformed into the hypergeometric differential equation

$$\tilde{z}(1 - \tilde{z}) \varphi'' + \left[C - (A + B + 1) \tilde{z} \right] \varphi' - AB \varphi = 0, \tag{4.35}$$

where $\psi = \tilde{z}^{m/2} \varphi$,

$$\begin{aligned} A &= (m - \overline{m})/2, \\ B &= (m + \overline{m})/2, \\ C &= m + 1, \\ \overline{m} &= \sqrt{m^2 + 8} \end{aligned} \tag{4.36}$$

and

$$\tilde{z} = \frac{\alpha}{2} \frac{1}{1 - nq_0/m} \left(\frac{r}{r_a} \right)^2, \tag{4.37}$$

with $q_0 = q(0)$.

Solution of (4.34) which is finite for $r = 0$ is

$$\psi \propto \tilde{z}^{m/2} F(A, B; C; \tilde{z}), \tag{4.38}$$

where $F(A, B; C; \tilde{z})$ is a hypergeometrical function.

From (4.38) we find that

$$r_a(\ln\psi)'\big|_{a-} = m + 2\tilde{z}_a \frac{AB}{C}\frac{F(A+1,B+1;C+1;\tilde{z}_a)}{F(A,B;C;\tilde{z}_a)}, \tag{4.39}$$

where $\tilde{z}_a = \tilde{z}(r_a)$.

Allowing for (4.5), (3.26), (4.32) and (4.39), from (4.17) it follows that the stability criteria for the parabolic current profile of the form (2.18) is given by

$$2\frac{(1-\alpha)}{(2-\alpha)}\frac{\tilde{\mu}_a}{\tilde{\mu}_a - n/m} - m\frac{2m+\Gamma_m}{2m+\Gamma_m\left[1-(r_a/r_w)^{2m}\right]} - \tilde{z}_a\frac{AB}{C}\frac{F(A+1,B+1;C+1;\tilde{z}_a)}{F(A,B;C;\tilde{z}_a)} > 0, \tag{4.40}$$

where $\Gamma_m = \infty$ corresponds to the ideal wall limit, and $\Gamma_m = 0$ to the no wall limit.

Radial profiles of safety factor are shown in Fig. 4.5 for different values of the parameter α. One can see that for given nq_a and negative α there is a possibility to have a resonance surface within the plasma, this happens when $nq_a > m/(1-\alpha/2)$. Since we assumed the plasma to be ideal, from (4.5) it follows that $b_r(r_s) = 0$, otherwise we would have unphysical singularity for the displacement. Therefore, our solution (4.38) is not valid anymore. These special cases with rational surface inside the plasma we will consider later. Now let us turn to the stability boundaries, which are plotted in Fig. 4.6 on the nq_a - α plane. With or without the wall, the upper stability limit is the same $nq_a = m$ for $0<\alpha<1$, for $-1<\alpha<0$ our consideration is limited by $nq_a = m/(1-\alpha/2)$. For the no-wall case, the range of nq_a where the mode is unstable shrinks as we increase α from -1 to 1. With a closer ideal wall the stability area enlarges.

In the range between ideal and no wall stability limits for the configuration with the resistive wall, the growth rate is small enough to neglect the inertia of plasma. Substituting (4.39) into (4.16), we find the dispersion relation

$$2\frac{(1-\alpha)}{(2-\alpha)}\frac{\tilde{\mu}_a}{\tilde{\mu}_a - n/m} - m\frac{2m+\Gamma_m}{2m+\Gamma_m\left[1-(r_a/r_w)^{2m}\right]} - \tilde{z}_a\frac{AB}{C}\frac{F(A+1,B+1;C+1;\tilde{z}_a)}{F(A,B;C;\tilde{z}_a)} = 0. \tag{4.41}$$

Its solutions are plotted in Figs. 4.7 and 4.8. Closer is the ideal stability limit larger is the growth rate. With a more distant wall the stability deteriorates.

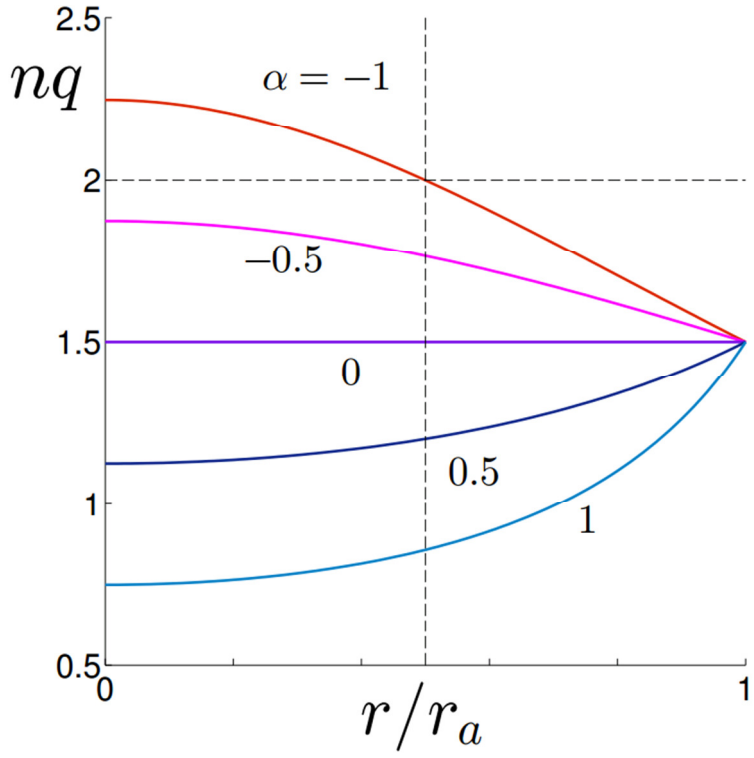

Fig. 4.5. Radial safety factor nq profiles for different α from -1 to 1. Vertical dashed line indicates the resonance surface position for $m=2$ mode and $\alpha=-1$.

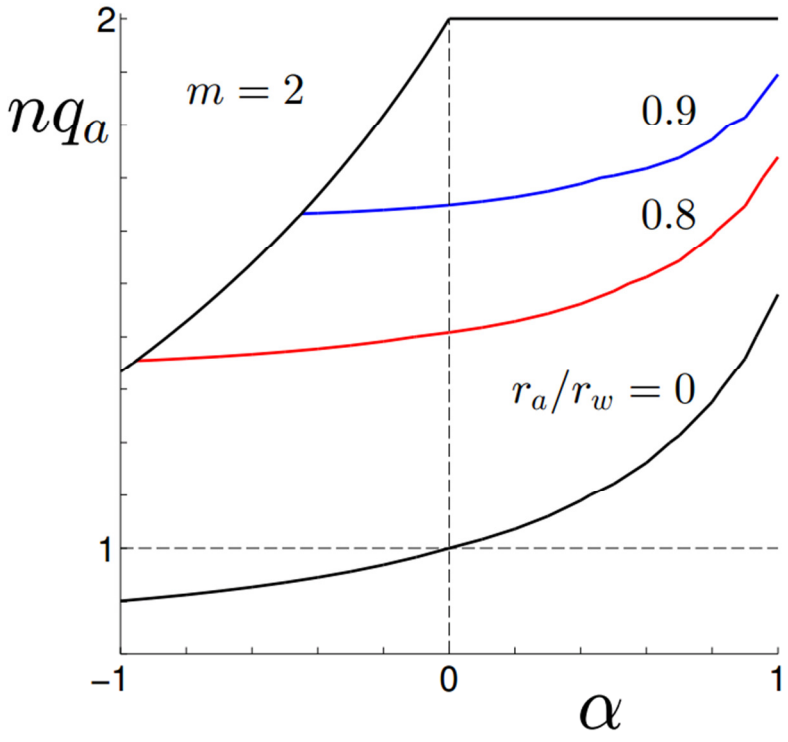

Fig. 4.6. The stability boundaries on the nq_a - α plane. In the area limited by the uppermost line from the top and one of the curves from the bottom the $m=2$ mode is ideally unstable. The lowermost curve corresponds to the no wall case, while two others to the ideal wall at r_a/r_w =0.8 and 0.9, respectively.

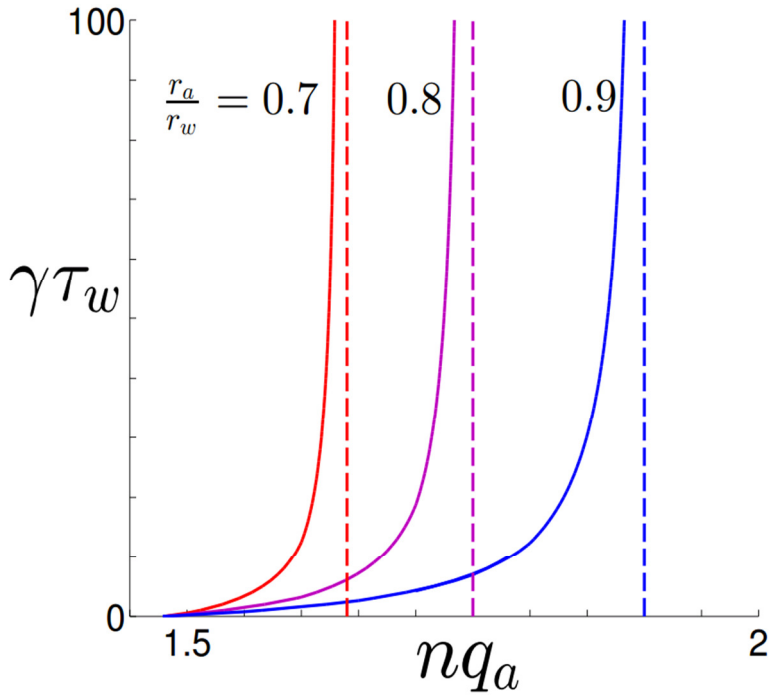

Fig. 4.7. The growth rate (solid curves) $\gamma = \gamma_R$ normalized to the wall time τ_w versus edge safety factor nq_a calculated by Eq. (4.41) for $m=2$ mode and $\alpha=1$. From left to right, the wall at r_a / r_w =0.7, 0.8 and 0.9. Vertical dashed lines designate corresponding ideal stability limits. (cf. Fig.4.2 plotted for $\alpha=0$).

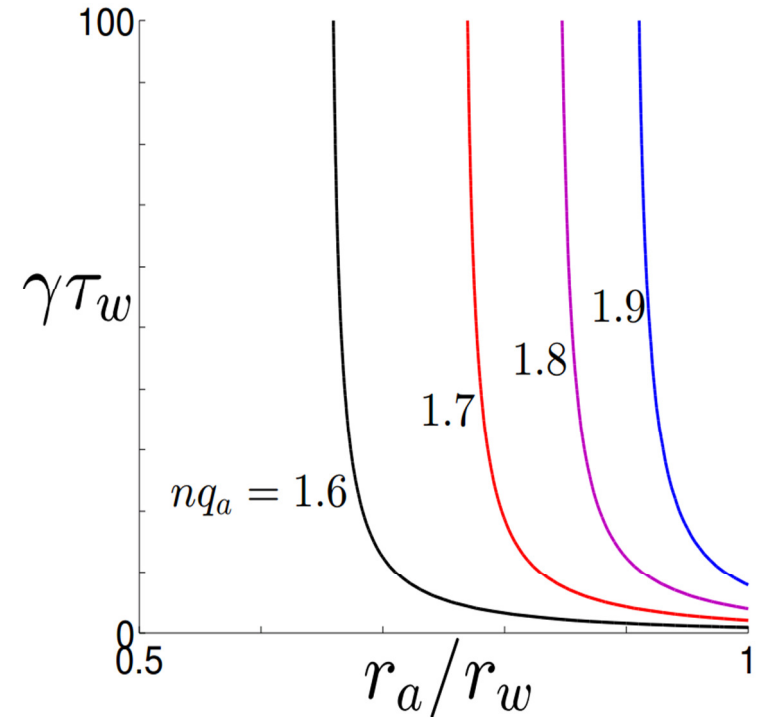

Fig. 4.8. The growth rate $\gamma = \gamma_R$ normalized to the wall time τ_w versus the resistive wall position for $m=2$ mode and $\alpha=1$. From left to right, the edge safety factor nq_a =1.6, 1.7, 1.8 and 1.9.

V. IDEAL PLASMA WITH RESISTIVE LAYERS

5.1. Resistive layers

Using induction equation (2.1) and generalized Ohm's law (2.6), one can obtain

$$\frac{\partial \mathbf{B}}{\partial t} = \nabla \times (\mathbf{v} \times \mathbf{B}) + \frac{\eta_{pl}}{\mu_0} \Delta \mathbf{B} . \tag{5.1}$$

Linearizing (5.1), for incompressible plasma, $\nabla \cdot \mathbf{v} = 0$, we find that

$$\frac{\partial \mathbf{b}}{\partial t} = (\mathbf{B}_0 \cdot \nabla)\mathbf{v}_1 + (\mathbf{b} \cdot \nabla)\mathbf{v}_0 - (\mathbf{v}_0 \cdot \nabla)\mathbf{b} - (\mathbf{v}_1 \cdot \nabla)\mathbf{B}_0 + \frac{\eta_{pl}}{\mu_0} \Delta \mathbf{b} . \tag{5.2}$$

The radial component of the above equation is

$$\frac{\partial b_r}{\partial t} = (\mathbf{B}_0 \cdot \nabla) v_{1,r} - (\mathbf{v}_0 \cdot \nabla) b_r + \frac{\eta_{pl}}{\mu_0} [\Delta \mathbf{b}]_r . \tag{5.3}$$

The second term on the RHS of (5.3) determines the phase shift due to the equilibrium plasma flow

$$(\mathbf{v}_0 \cdot \nabla) b_r = -i \Omega b_r , \tag{5.4}$$

with

$$\Omega = \left(\frac{n V_z}{R} - \frac{m V_\theta}{r} \right), \tag{5.5}$$

where V_z and V_θ are the toroidal and poloidal equilibrium plasma velocities. The last term in (5.3) with resistivity becomes important only in the vicinity of the rational surface where $\mathbf{B}_0 \cdot \nabla \approx 0$. We take advantage of this fact to find an analytical solution of the problem by dividing imaginatively the plasma in the resistive and ideal regions.

5.2. Constant - ψ approximation and Δ'

We assume that

$$\left| \hat{s} \ln \Delta \hat{x} \right| << 1 , \tag{5.6}$$

where $\Delta \hat{x}$ is the characteristic length of the resistive layer,

$$\hat{s} = -\frac{1}{2} + \left(\frac{1}{4} + U_0 \right)^{1/2}, \tag{5.7}$$

$$U_0 = \frac{2 r_s p'}{B_z^2 S^2}, \tag{5.8}$$

$$S = \left. \frac{r q'}{q} \right|_s . \tag{5.9}$$

In this case, for modes with $m > 1$, we can allow for continuity of ψ across the resistive region and use Δ' formalism [4].

Matching condition for two adjacent ideal solutions at the rational surface is [6, 59]

$$\Delta' = \Delta'_{in}, \tag{5.10}$$

$$\Delta' = \left. \frac{r \psi'}{\psi} \right|_{s+} - \left. \frac{r \psi'}{\psi} \right|_{s-}, \tag{5.11}$$

where subscripts $s-$ and $s+$, refer to the inner and outer sides of the resistive layer, respectively. Parameter Δ'_{in} is given by [6] (here we ignore inconsequential constants)

$$\Delta'_{in} = \frac{\bar{\gamma}^{5/4}}{|S|^{1/2}}, \tag{5.12}$$

$$\bar{\gamma} = (\gamma - i\Omega)\tau_s, \tag{5.13}$$

$$\tau_s = \tau_R^{3/5} \tau_A^{2/5}, \tag{5.14}$$

where plasma resistive time is determined by

$$\tau_R \equiv \frac{\mu_0 r_a^2}{\eta_{pl}}, \tag{5.15}$$

and τ_A is given by (4.14).

5.3. Resistive layer in the gap

5.3.1. Derivation of dispersion relation

Let us assume that instead of vacuum in the gap between ideal plasma and the wall there is a resistive plasma without equilibrium current and that there is a resonant surface $r_a < r_s < r_w$ (Fig. 5.1).

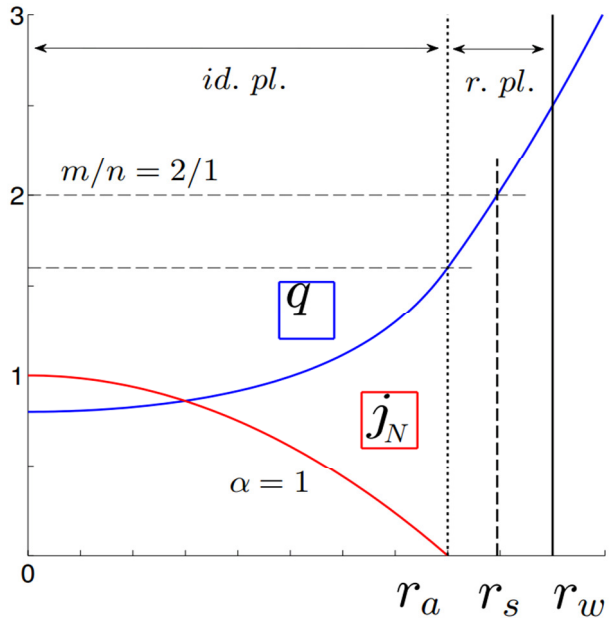

Fig. 5.1. Configuration under study and basic notations. The ideal plasma cylinder of radius r_a is surrounded by the coaxial conducting wall with radius r_w. The ideal plasma-wall gap contains a resonant surface of radius r_s and treated as resistive plasma. Beyond the wall is vacuum.

In this case the solutions of (3.2) in the gap on the left and on the right from the resonance are

$$\psi_{g1} \propto C_{g1}(r/r_s)^m + (r/r_s)^{-m}, \tag{5.16}$$

$$\psi_{g2} \propto C_{g2}(r/r_w)^m + (r/r_w)^{-m}. \tag{5.17}$$

For the wall at infinity ($C_{g2} = 0$), and for the ideal wall at r_w ($C_{g2} = -1$), Δ' is given by

$$\Delta'_\infty = -m - \left.\frac{r\psi'_{g1}}{\psi_{g1}}\right|_s, \tag{5.18}$$

and

$$\Delta'_{id} = -m\frac{1+(r_s/r_w)^{2m}}{1-(r_s/r_w)^{2m}} - \left.\frac{r\psi'_{g1}}{\psi_{g1}}\right|_s , \tag{5.19}$$

respectively.

Then, in terms of Δ'_∞ and Δ'_{id} for a resistive wall we have

$$\Delta' = \frac{\Delta'_\infty + R(\gamma)\Delta'_{id}}{1+R(\gamma)}, \tag{5.20}$$

where

$$R(\gamma) = \frac{\Gamma_m}{2m}\left[1-\left(\frac{r_s}{r_w}\right)^{2m}\right]. \tag{5.21}$$

From (5.16) it follows that

$$\left.\frac{r\psi'_{g1}}{\psi_{g1}}\right|_s = -m + 2m\frac{C_{g1}}{1+C_{g1}}, \tag{5.22}$$

and

$$C_{g1} = \left(\frac{r_a}{r_s}\right)^{-2m}\left.\frac{m + r\psi'_{g1}/\psi_{g1}}{m - r\psi'_{g1}/\psi_{g1}}\right|_{a+} . \tag{5.23}$$

From (4.11), we find that matching conditions for plasma-vacuum interface in neglecting surface currents (we consider slow modes only, $|\gamma\hat{\tau}_A| << 1$) is

$$\left.\frac{r\psi'}{\psi}\right|_{a-}^{a+} = \left.\frac{r\tilde{\mu}'}{\tilde{\mu}-n/m}\right|_{a-}^{a+} . \tag{5.24}$$

For the current profile of the form (2.18), RHS of (5.24) is given by

$$\left.\frac{r\tilde{\mu}'}{\tilde{\mu}-n/m}\right|_{a-}^{a+} = -4\frac{(1-\alpha)}{(2-\alpha)}\frac{\tilde{\mu}_a}{\tilde{\mu}_a - n/m}, \tag{5.25}$$

and $r_a(\ln\psi)'|_{a-}$ on the LHS is determined by (4.39).

Allowing for (5.12) where we omit magnetic shear S for simplicity, we arrive at the dispersion relation

$$\bar{\gamma}^{5/4} = \frac{\Delta'_{\infty} + R(\gamma)\Delta'_{id}}{1 + R(\gamma)}. \tag{5.26}$$

5.3.2. Rotational stabilization of RWMs

For $B_z = 2.2T$, a deuterium DIII-D plasma with $n_e = 5 \cdot 10^{19} m^{-3}$, $T_e = 5keV$ and $r_a = 0.67m$ has characteristic times $\tau_R \approx 5\,\text{min}$ and $\tau_A \approx 0.1\mu s$, giving a typical growth time $\tau_s \approx 50ms$. To compare, the resistive wall time for DIII-D, $\tau_w \approx 5ms$, therefore $\tau_s / \tau_w \approx 10$. For ITER with $B_z = 5.3T$, $n_e = 10^{20} m^{-3}$, $T_e = 5keV$ and $r_a = 2m$, we obtain $\tau_R \approx 25\,\text{min}$, $\tau_A \approx 0.2\mu s$ and $\tau_s \approx 250ms$, the time constant of its vacuum vessel $\tau_w \approx 188ms$ and hence $\tau_s / \tau_w \approx 1$.

The mode stabilization by plasma rotation was considered in [18] within a similar model, but for the flat current profile. In that paper the ratio τ_s / τ_w was assumed to be around 0.01, which for parameters of DIII-D corresponds to the electron temperature less than $10eV$. Just above we have shown that for fusion plasmas relevant values of τ_s / τ_w are in the different range $\tau_s / \tau_w \approx 1-10$. As we will see now the critical plasma rotation, such that the mode becomes stabilized, scales indeed, as it was noticed in [18] with $1/\tau_s$, but only if $\tau_s / \tau_w < 1$, when $\tau_s / \tau_w > 1$ it scales with $1/\tau_w$. In Fig. 5.3 the growth rate $\gamma_N = \gamma_R / \gamma_R^{vac}$ normalized on its value at $\tau_s = 0$ ($\gamma_R^{vac} \tau_w = 12.49$) is plotted versus plasma rotational frequency Ω normalized to τ_s. If $\tau_s / \tau_w < 1$, then for smaller τ_s / τ_w and fixed τ_s we need less plasma rotation for stabilization $\Omega \tau_s$, while if we fix τ_w the mode stabilizes at higher $\Omega \tau_w$. The case $\tau_s / \tau_w > 1$ is illustrated in Fig. 5.4, which is the same plot as Fig. 5.3, but with normalization of Ω to τ_w. Critical plasma rotation almost doesn't change with increase of τ_s / τ_w or in other words does not depend on τ_s. The other difference between $\tau_s / \tau_w > 1$ and $\tau_s / \tau_w < 1$, is that for the first case the mode is frozen into the fluid, $\omega \approx \Omega$, while for the second case ω can significantly differ from Ω , especially when the

wall is close to the rational surface. This is shown in Figs. 5.5 and 5.6, where critical plasma frequency $\Omega_{cr}\tau_w$ and corresponding value of the mode frequency $\omega_{cr}\tau_w$ are plotted as functions of the wall position for τ_s/τ_w =0.1, 1 and 10. The critical mode frequency $\omega_{cr}\tau_w$ does not change with τ_s/τ_w. Both Ω_{cr} and ω_{cr} increase when the wall is getting closer to the ideal limit or the rational surface position. For $\tau_s/\tau_w > 1$, in the wide range of r_a/r_w they vary slightly around $10/\tau_w$. Fig. 5.7 shows that with the increase of the plasma rotation, the range of the wall position where the mode is stable becomes wider. It has to be noticed that the mode can also be, in some cases, destabilized by rotation, in the sense that the growth rate can be larger in comparison with its value without rotation, this is illustrated in Fig. 5.8. For calculations the thin wall approximation (3.18) was used.

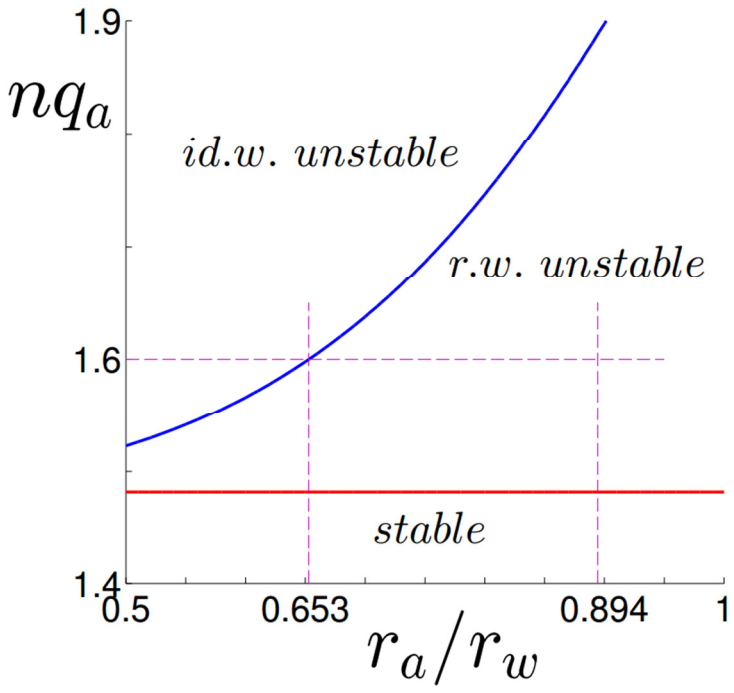

Fig. 5.2. The stability boundaries on the nq_a - r_a/r_w plane. The $m=2$ mode is unstable with an ideal wall above the upper curve and with no wall above the horizontal solid line. Vertical dashed lines indicate for $nq_a=1.6$ wall positions when the mode becomes unstable with an ideal wall $r_a/r_w=0.653$ and when the rational surface is expelled from the gap beyond the wall $r_a/r_w=0.894$.

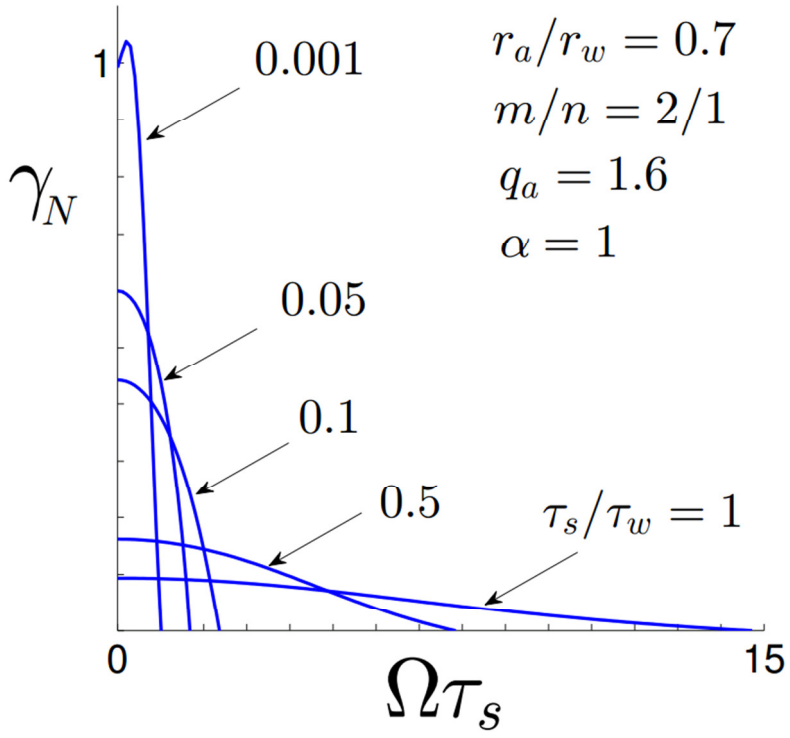

Fig. 5.3. Growth rate $\gamma_N = \gamma_R / \gamma_R^{vac}$ normalized on its value at $\tau_s = 0$ ($\gamma_R^{vac}\tau_w = 12.49$), versus plasma rotational frequency $\Omega\tau_s$ for τ_s/τ_w =0.001, 0.05, 0.1, 0.5 and 1. For calculations we used $nq_a = 1.6$, $\alpha = 1$, $m/n = 2/1$, $r_a/r_w = 0.7$.

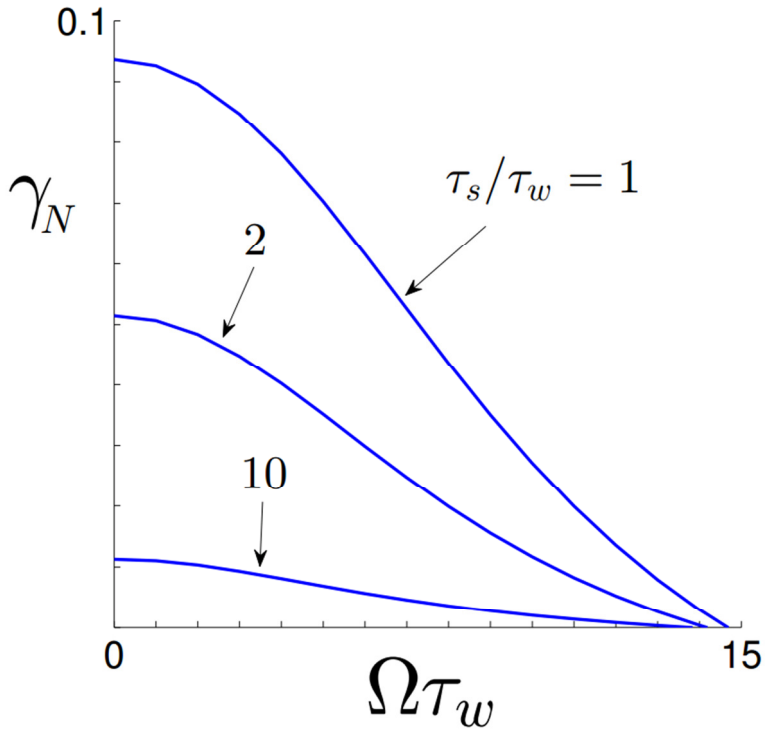

Fig. 5.4. The same plot as in Fig. 5.3, but with different normalization of Ω and for τ_s/τ_w =1, 2, 10.

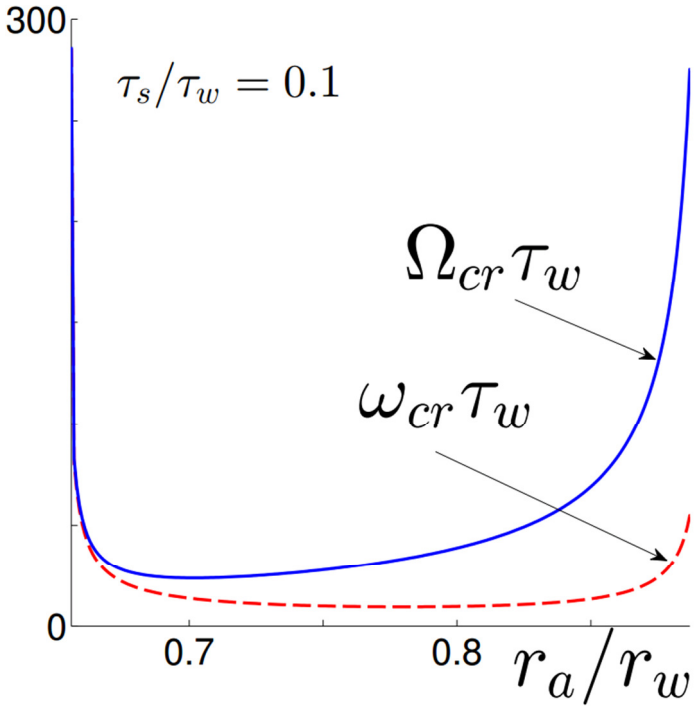

Fig. 5.5. Critical plasma rotation and corresponding value of mode frequency versus wall position for $\tau_s/\tau_w = 0.1$. For calculations we used $nq_a = 1.6$, $\alpha = 1$, $m/n = 2/1$.

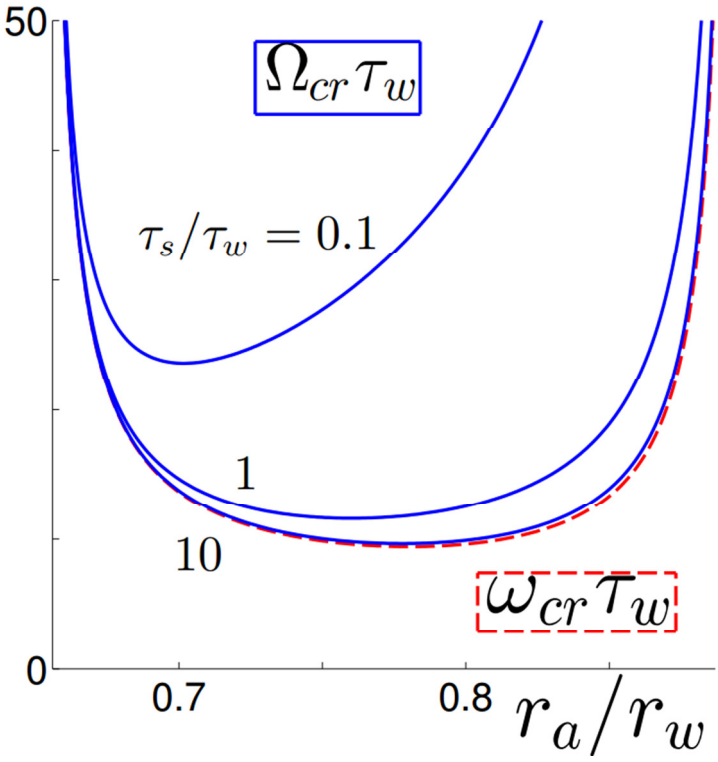

Fig. 5.6. The same plot as in Fig. 5.5, but for $\tau_s/\tau_w = 0.1$. 1 and 10. The mode rotational frequency (dashed curve) is the same for all three cases.

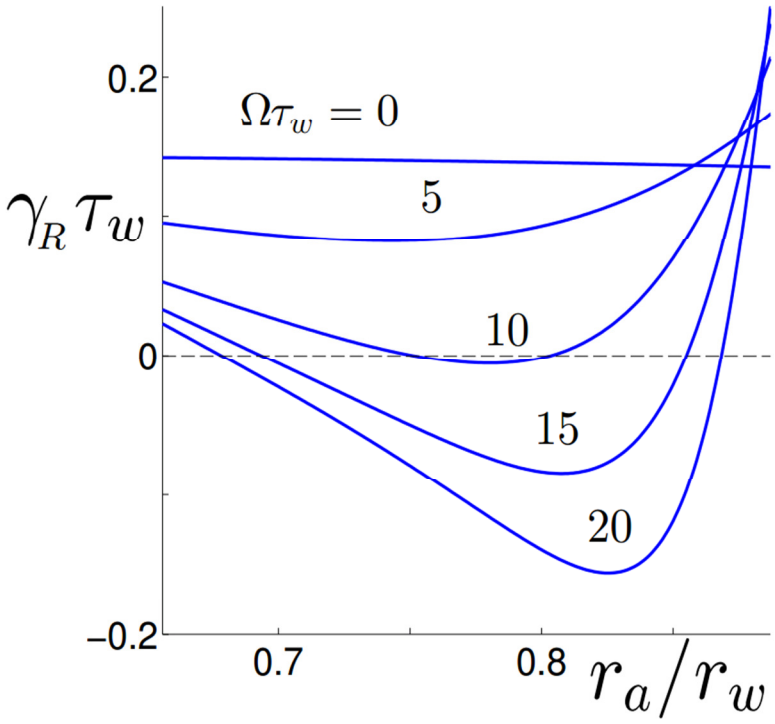

Fig. 5.7. Growth rate of $m/n = 2/1$ mode versus wall position for different plasma rotation $\Omega\tau_w$ from 0 to 20. For calculations we used $nq_a = 1.6$, $\alpha = 1$, $\tau_s/\tau_w = 10$. The mode and plasma rotational frequencies almost coincide.

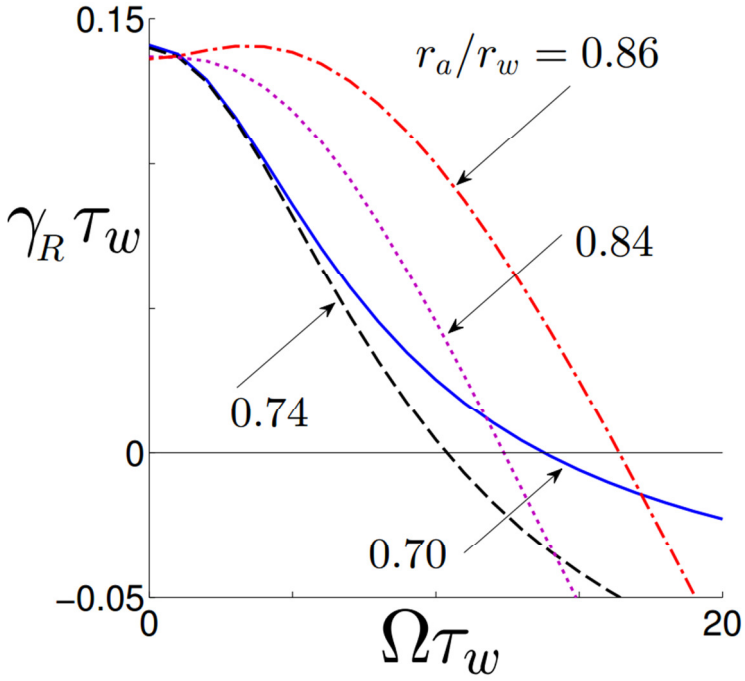

Fig. 5.8. Growth rate of $m/n = 2/1$ mode versus plasma rotational frequency $\Omega\tau_w$ for wall at r_a/r_w =0.70, 0.74, 0.84 and 0.86. For calculations we used $nq_a = 1.6$, $\alpha = 1$, $\tau_s/\tau_w = 10$.

5.4. Resistive layer in the current carrying plasma

5.4.1. Derivation of dispersion relation

Let us assume that the rational surface is located within the current carrying plasma $0 < r_s < r_a$. The gap between plasma and the wall we treat either as vacuum or currentless resistive plasma (Fig. 5.9) .

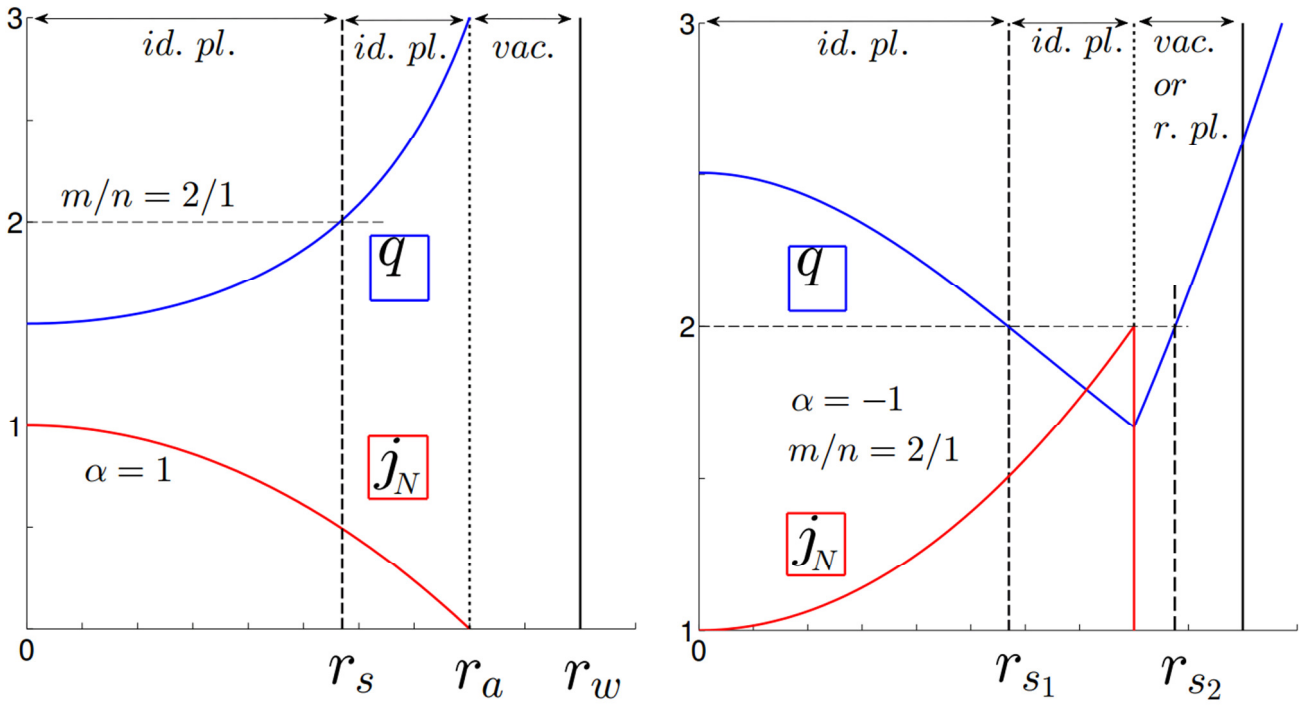

(a) (b)

Fig. 5.9. Configuration under study and basic notations. The plasma cylinder of radius r_a is surrounded by the coaxial conducting wall with radius r_w. Two ideal plasma regions are divided by the thin layer of resistive plasma. The plasma-wall gap is treated either as vacuum or currentless resistive plasma. Fig. 5.9a is plotted for $\alpha=1$, when only one rational surface of radius r_s exists, while Fig. 5.9b shows the case with $\alpha=-1$ and two resonances located at r_{s1} and r_{s2}.

In this case (4.34) can be transformed into the hypergeometric differential equation

$$z(1-z)\varphi'' + [C-(A+B+1)z]\varphi' - AB\varphi = 0, \qquad (5.27)$$

where $\psi = z^{m/2}\varphi$,

$$z = (r / r_s)^2 , \tag{5.28}$$

and A , B , C are determined by (4.36).

Solution of (4.34) in the internal region, $r < r_s$, which is finite for $r = 0$ is of the form

$$\psi_i \propto z^{m/2} F_i , \tag{5.29}$$

$$F_i \equiv F(A, B; C; z) . \tag{5.30}$$

For the external region, $r_s < r < r_a$, the solution of (4.34) is of the form

$$\psi_e \propto C_e z^{\overline{m}/2} F_1 + z^{-\overline{m}/2} F_2 , \tag{5.31}$$

$$F_1 \equiv F(A, A - C + 1; A - B + 1; 1/z) , \tag{5.32}$$

$$F_2 \equiv F(B, B - C + 1; B - A + 1; 1/z) , \tag{5.33}$$

here C_e is a constant. From (5.29) we find that

$$\frac{r\psi_i'}{\psi_i} = m + 2\frac{zF_i'}{F_i} , \tag{5.34}$$

where F_i' is a derivative of F_i with respect to z .

From (5.31) we find that

$$\frac{r\psi_e'}{\psi_e} = -\overline{m} - \frac{2}{z}\frac{C_e z^{\overline{m}}(F_1' - \overline{m} z F_1) + F_2'}{C_e z^{\overline{m}} F_1 + F_2} , \tag{5.35}$$

where F_1' , F_2' are derivatives of F_1 and F_2 , with respect to $1/z$.

When $|1 - z| << 1$, we have approximate formula [60]

$$F(u, v; u + v; z) = \frac{\Gamma(u + v)}{\Gamma(u)\Gamma(v)}\left[2\tilde{\psi}(1) - \tilde{\psi}(u) - \tilde{\psi}(v) - \ln(1 - z)\right], \tag{5.36}$$

where Γ and $\tilde{\psi}$ are gamma and digamma functions, respectively. Taking into account also that

$$F(u, v; u + v + 1; 1) = \frac{\Gamma(u + v + 1)}{uv\Gamma(u)\Gamma(v)} , \tag{5.37}$$

for $|1 - z| << 1$, we find from (5.34) and (5.35) that

$$\frac{r\psi_i'}{\psi_i} = m - 4\left[2\tilde{\psi}(1) - \tilde{\psi}(A + 1) - \tilde{\psi}(B + 1) - \ln(1 - z)\right] \tag{5.38}$$

$$\frac{r\psi_e'}{\psi_e} = -\overline{m} - 4\left[2\tilde{\psi}(1) - \ln(1-z)\right] + 4\frac{C_e\left[\overline{m}/2 + \tilde{\psi}(A+1) + \tilde{\psi}(-B+1)\right] + \delta\left[\tilde{\psi}(-A+1) + \tilde{\psi}(B+1)\right]}{C_e + \delta}, \tag{5.39}$$

where

$$\delta = -\frac{\Gamma(B-A)}{\Gamma(A-B)}\frac{\Gamma(A)}{\Gamma(-A)}\frac{\Gamma(-B)}{\Gamma(B)}. \tag{5.40}$$

Both logarithmic derivatives (5.38) and (5.39) have a singularity at the rational surface but their difference is finite:

$$\Delta' = 4\pi\frac{C_e\cot(\pi B) + \delta\cot(\pi A)}{C_e + \delta}. \tag{5.41}$$

From (5.35) it follows that

$$C_e = -z^{-\overline{m}}\left.\frac{2F_2' + (\overline{m} + r\psi_e'/\psi_e)zF_2}{2F_1' + (-\overline{m} + r\psi_e'/\psi_e)zF_1}\right|_{a-}. \tag{5.42}$$

Matching condition for the plasma-vacuum interface (5.24) reduces to

$$\left.\left(\frac{r\psi_g'}{\psi_g} - \frac{r\psi_e'}{\psi_e}\right)\right|_a = f_\alpha \qquad , \tag{5.43}$$

where

$$f_\alpha \equiv \left.\frac{r\mu'}{\mu - n/m}\right|_{a-}^{a+} = \frac{4}{1-(r_s/r_a)^2}\frac{1-\alpha}{\alpha}, \tag{5.44}$$

and $r_a(\ln\psi_g)'\big|_{a+}$ on the LHS of (5.43) is determined by (3.24)

If the ideal wall is at the plasma edge, then $\psi_e(r_a) = 0$ and $C_e = C_e^{id}$

$$C_e^{id} = -z^{-\overline{m}}\left.\frac{F_2}{F_1}\right|_{a-} = -z^{-\overline{m}}\left.\frac{F(B, B-C+1; B-A+1; 1/z)}{F(A, A-C+1; A-B+1; 1/z)}\right|_{a-}. \tag{5.45}$$

From (5.10) it follows that the dispersion relation for rotating linear tearing modes in the presence of the resistive wall is

$$\Delta' = \Delta'_{in}, \tag{5.46}$$

where Δ' is given by (5.41) and Δ'_{in} by (5.12).

5.4.2. Numerical results for $\alpha > 0$

As it follows from (5.46), locked tearing modes are unstable if $\Delta' > 0$. Parameter Δ', given by (5.41) is plotted in Fig. 5.10 versus rational surface position for parabolic current with $\alpha = 1$. With an ideal wall at the plasma surface only $m = 2$ and $m = 3$ perturbations are unstable. Without any wall, $m = 2$ and $m = 3$ harmonics are unstable for an arbitrary resonance position, while $m \geq 4$ modes are localized at the plasma edge, as shown in Fig. 5.11. Figs. 5.12 and 5.13 illustrate the case when an ideal wall is separated from plasma by a vacuum gap. The wall has a positive effect on the plasma stability, its influence is stronger when it is located closer to the plasma.

The parameter α affects the solution through the boundary conditions only. That is the reason why Δ' is independent on α if an ideal wall is situated at the plasma surface. When $\alpha << 1$, from (5.44) and (5.43) we find that $\psi_e(r_a) \approx 0$, the same condition as with an ideal wall at r_a. Therefore, we can conclude that for $|\alpha| << 1$, influence of boundary conditions on the stability is negligible. In Fig. 5.14 α varies from -1 to 1 for configuration without any wall. Decreasing α one can stabilize modes located close to the plasma edge. As shown in Fig. 5.15, already at $\alpha = 0.99$ modes with $m \geq 5$ are stable, and the growth of $m = 2-4$ modes is mitigated,

5.4.3. Rotational stabilization for $\alpha > 0$

If a tearing mode is stable with the ideal wall, it can be also stabilized by plasma rotation in the presence of the resistive wall [61]. In Fig. 5.20 growth rate $\gamma_N = \gamma_R \tau_w$ of $m/n = 3/1$ rotating modes is plotted versus resistive wall position. Depending on the plasma rotational frequency $\Omega_N = \Omega \tau_w$ instability is either mitigated or stabilized. Critical plasma rotational frequency Ω_{cr} at which the mode becomes stable depends on the resistive wall position and the ratio τ_s / τ_w. This is shown in Fig. 5.21, where $\Omega_{cr} \tau_w$ and corresponding value of the critical mode frequency $\omega_{cr} \tau_w$ are plotted versus r_w / r_a. For all three cases $\tau_s / \tau_w = 1$, 0.1 and 0.05, $\omega_{cr} \tau_w$ almost does not change and is shown by one red dashed curve. Results at $\tau_s / \tau_w > 1$ and $\tau_s / \tau_w = 1$ almost coincide for both $\Omega_{cr} \tau_w$ and $\omega_{cr} \tau_w$.

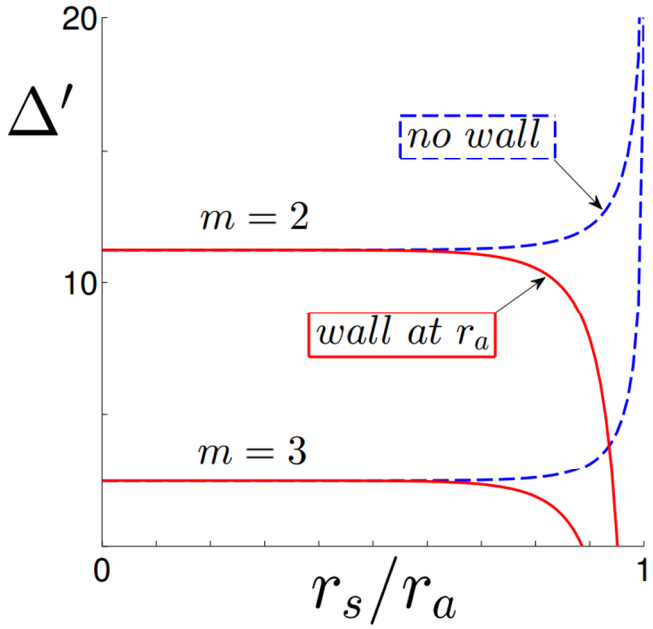

Fig. 5.10. Dependencies of Δ' on the position of the rational surface r_s / r_a for purely parabolic current profile (α=1). With the ideal wall at the plasma edge (solid curves) modes with $m=2$ and $m=3$ can be unstable ($\Delta'>0$), while modes with $m\geq 4$ are stable ($\Delta'<0$) for any r_s / r_a. Without any wall (dashed lines) m=2, 3 perturbations are unstable for arbitrary r_s / r_a.

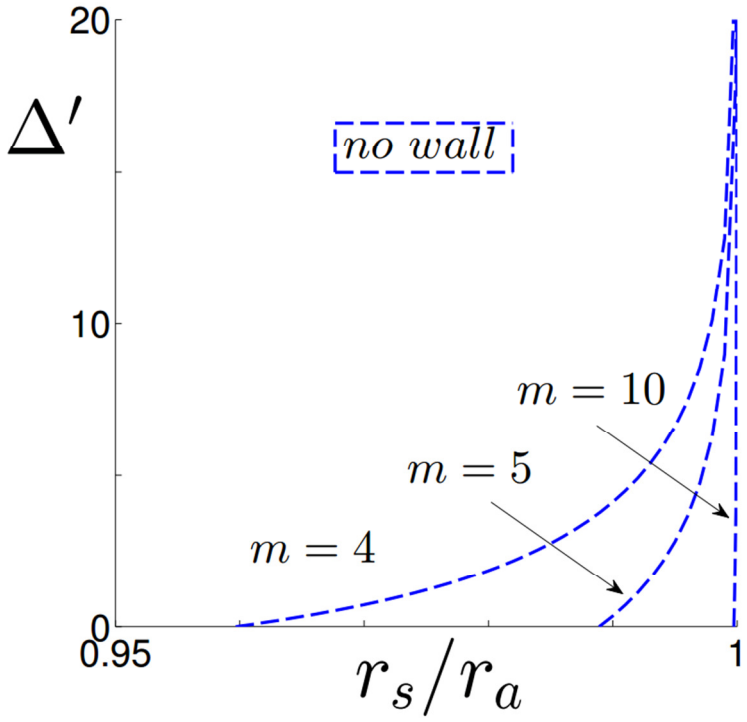

Fig. 5.11. The same plot as in Fig. 5.10, but in the range $0.95< r_s / r_a <1$. Without any wall, modes with $m\geq 4$ are localized at the plasma edge. For higher m number the instability area shrinks as illustrated for m=4, 5 and 10.

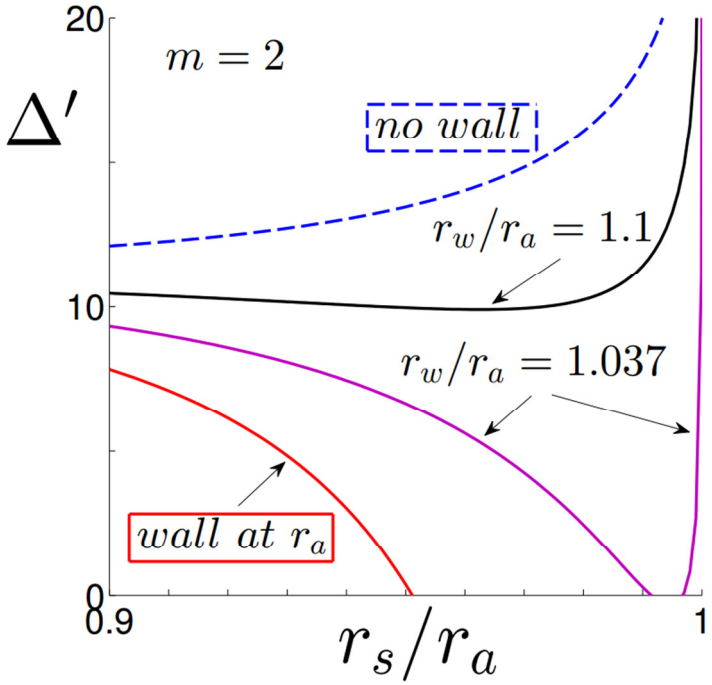

Fig. 5.12. Dependencies of Δ' on the position of the rational surface r_s / r_a for purely parabolic current profile ($\alpha=1$) and $m=2$ mode, with a wall at the plasma edge (red curve), with an ideal wall at $r_w / r_a = 1.037$ (solid purple), $r_w / r_a = 1.1$ (solid black) and without any wall (dashed blue line).

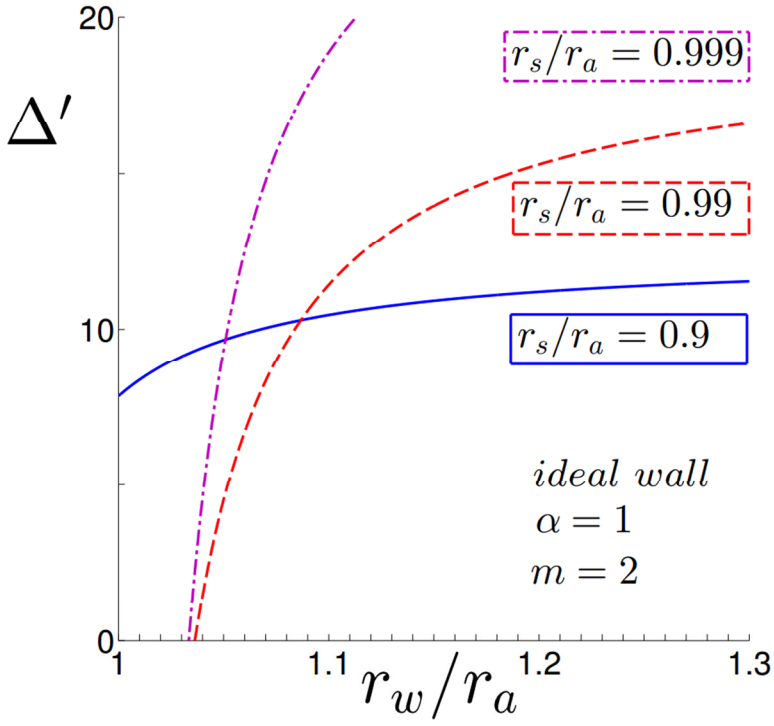

Fig. 5.13. Dependencies of Δ' on the position of the ideal wall r_w / r_a for purely parabolic current profile ($\alpha=1$) and $m=2$ mode, with a rational surface at $r_s / r_a = 0.9$ (blue solid curve), $r_s / r_a = 0.99$ (red dashed) and $r_s / r_a = 0.999$ (purple dash-dotted line).

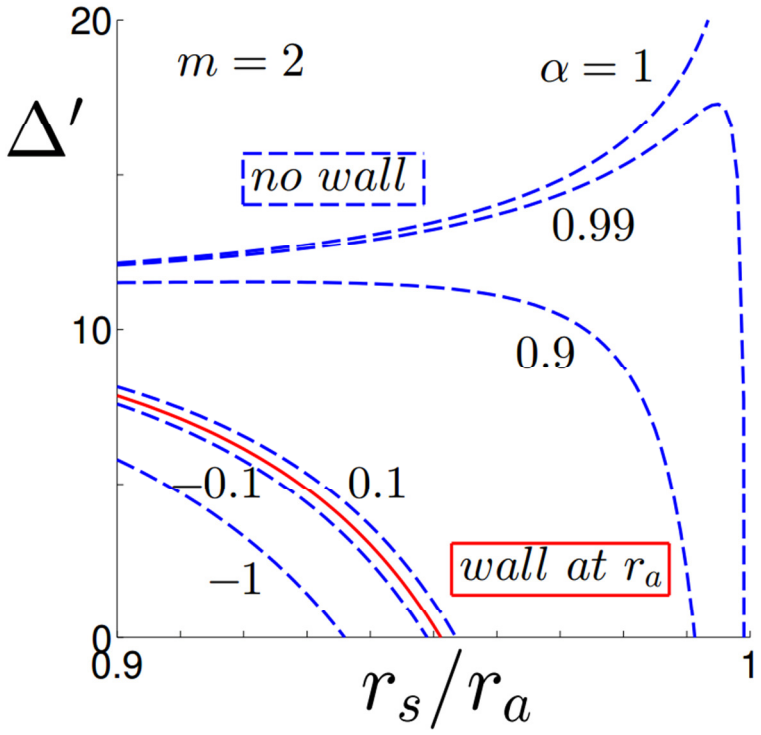

Fig. 5.14. Dependencies of Δ' on the position of the rational surface r_s / r_a for $m=2$ mode, and parabolic current profiles with α=1, 0.99, 0.9, 0.1, -0.1 and -1 as indicated on the plot. Dashed curves correspond to the no wall configuration, while the red solid line shows the case with a wall at the plasma surface, which is unaffected by the parameter of the parabolicity α.

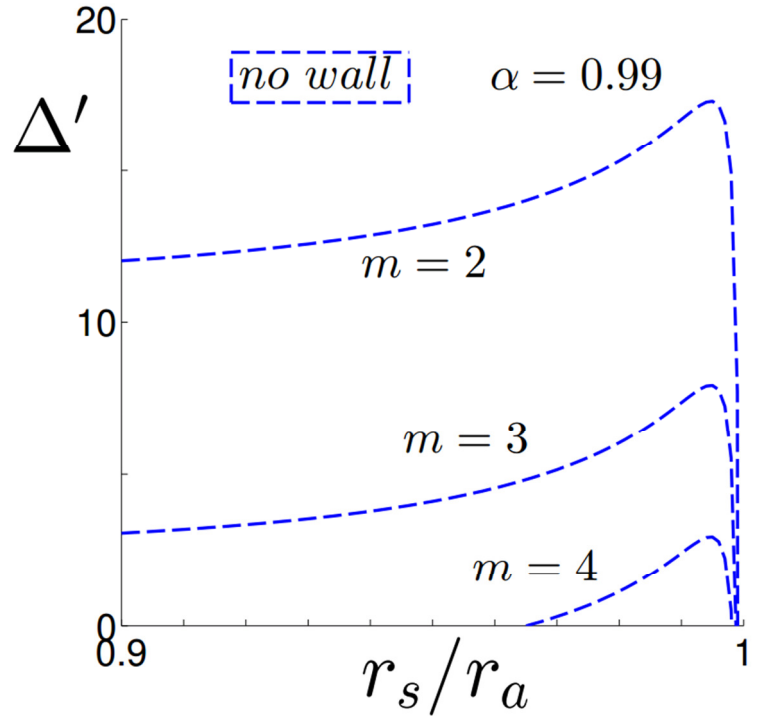

Fig. 5.15. Dependencies of Δ' on the position of the rational surface r_s / r_a for m=2, 3, 4 modes, parabolic current profiles with $\alpha=0.99$ and without any wall. Modes with $m \geq 5$ are stable, (cf. (Fig. 5.11)).

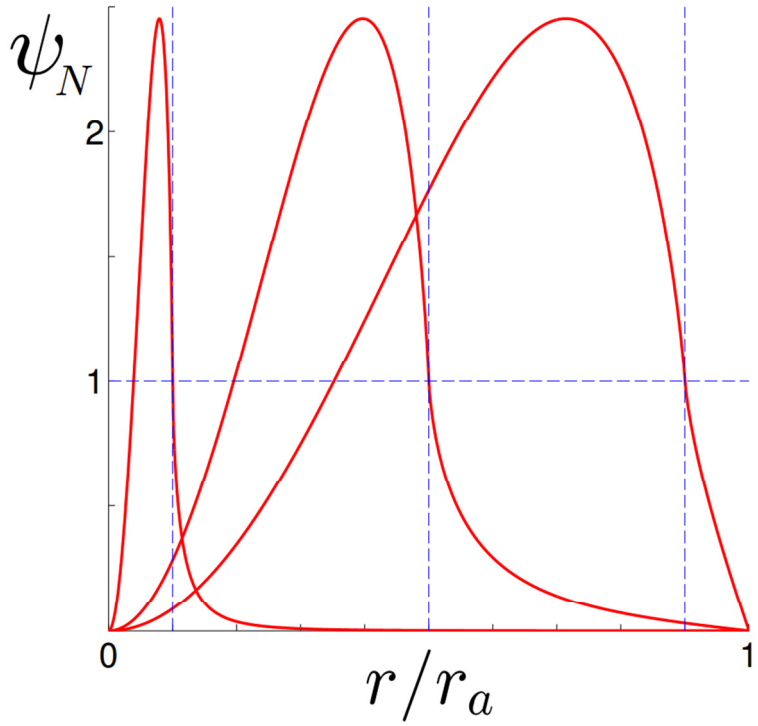

Fig. 5.16. The $m=2$ perturbation of the poloidal magnetic flux $\psi_N=\psi/\psi_s$ normalized on its value at the rational surface versus normalized radius r/r_a for configuration with a wall at the plasma edge and $r_s/r_a=0.1$, 0.5 and 0.9.

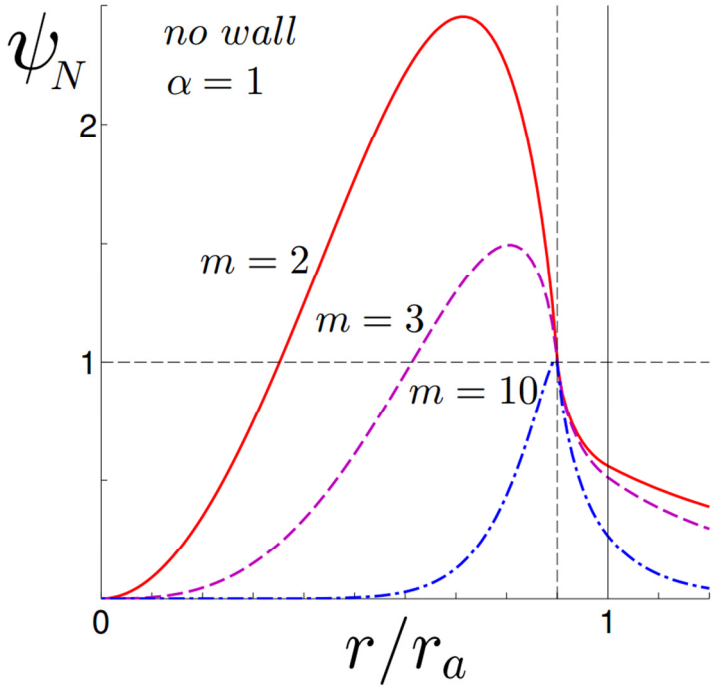

Fig. 5.17. $\psi_N=\psi/\psi_s$ versus r/r_a for no wall configuration with $r_s/r_a=0.9$ and $\alpha=1$, and modes with $m=2$ (red solid), $m=3$ (purple dashed) and $m=10$ (blue dash-dotted curve).

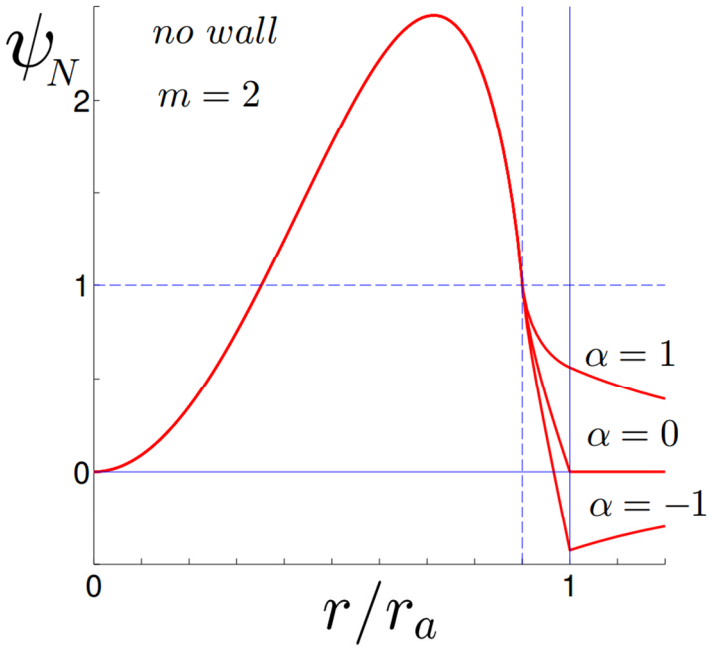

Fig. 5.18. The $m=2$ perturbation of the poloidal magnetic flux $\psi_N = \psi/\psi_s$ normalized on its value at the rational surface versus normalized radius r/r_a for no wall configuration with $r_s/r_a = 0.9$ and α=-1, 0 and 1, as indicated in the plot.

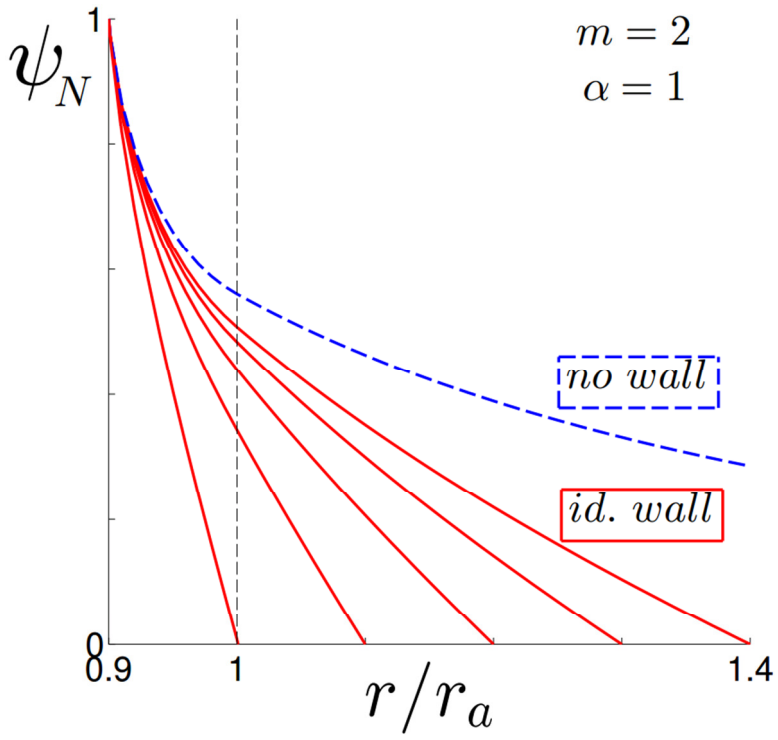

Fig. 5.19. The $m=2$ perturbation of the poloidal magnetic flux $\psi_N = \psi/\psi_s$ normalized on its value at the rational surface versus normalized radius r/r_a for $r_s/r_a = 0.9$ and $\alpha = 1$. Blue dashed line shows the no wall solution, while red solid curves are plotted for the ideal wall at r_w/r_a =1, 1.1, 1.2, 1.3 and 1.4.

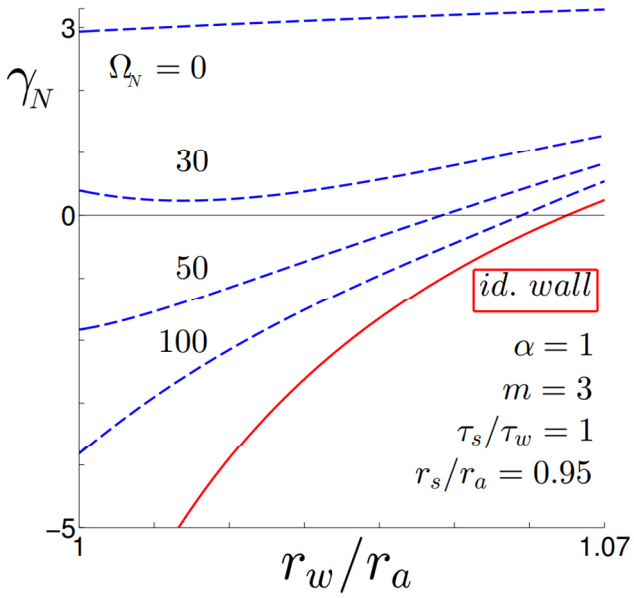

Fig. 5.20. Growth rate $\gamma_N = \gamma_R \tau_w$ of $m/n = 3/1$ mode versus resistive wall position for different plasma rotation $\Omega_N = \Omega \tau_w$ from 0 to 100 (blue dashed curves). Red solid curve corresponds to the case with the ideal wall. The plot is done for purely parabolic current profile (α=1), $\tau_s / \tau_w = 1$, $r_s / r_a = 0.95$.

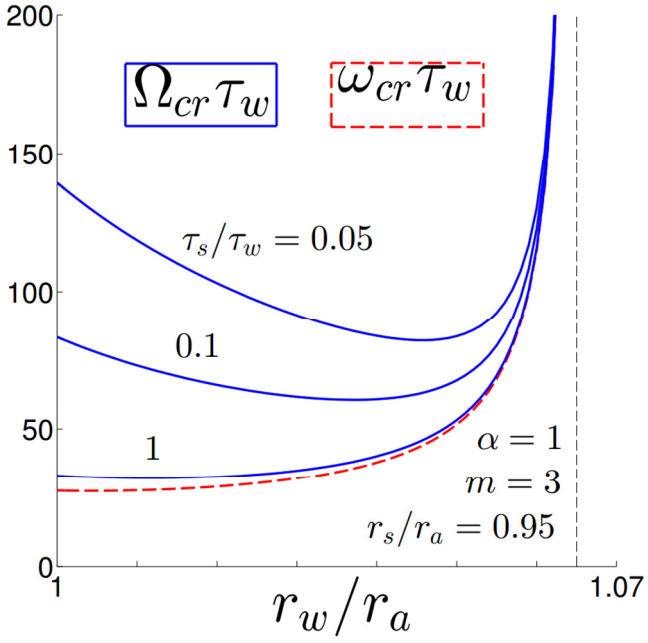

Fig. 5.21. Critical plasma rotation (blue solid curves) and corresponding value of mode frequency versus wall position for $\tau_s / \tau_w = 1$, 0.1 and 0.05. For calculations we used $r_s / r_a = 0.95$, α=1, $m/n = 3/1$. The mode rotational frequency (dashed curve) is the same for all three cases. For $\tau_s / \tau_w > 1$ plasma rotational frequency almost coincides with the mode's one. Dashed vertical line indicates the radius at which the mode becomes unstable with the ideal wall.

5.4.4. Numerical results for $\alpha < 0$

In contrast with $\alpha>0$ case, for $\alpha<0$ denominator in (5.41) can equal to zero and $\Delta' \to \infty$. In Fig. 5.22 Δ' is plotted versus r_s / r_a for α=-5 and -10 in the absence of any wall. Vertical dashed lines indicate critical rational surface positions r_s^{cr} / r_a where $\Delta' = \infty$, $r_s^{cr} / r_a = 0.4182$ for $\alpha = -5$ and $r_s^{cr} / r_a = 0.5318$ for $\alpha = -10$. In Fig. 5.23 radial dependencies of $\psi_N = \psi / \psi_s$ for $m = 2$ mode are shown for the case when r_s / r_a is close to the critical value, $r_s / r_a = 0.41$ for $\alpha = -5$ and $r_s / r_a = 0.52$ for $\alpha = -10$.

For $\alpha < 0$, an ideal wall can either stabilize or destabilize, depending on the rational surface and the wall positions. This is illustrated for $\alpha = -1$ and $m = 2$ mode in Fig. 5.24, where Δ' is plotted versus ideal wall radius r_w / r_a. The critical wall position r_w^{cr} / r_a, at which $\Delta' = \infty$, is located closer to plasma when r_{s1} / r_a is closer to the plasma edge. Just behind r_w^{cr} / r_a there is a range of r_w / r_a where the mode is stable, its width shrinks as r_{s1} / r_a decreases. The second rational surface r_{s2} / r_a is always inside the critical wall radius r_w^{cr} / r_a: $r_{s2} / r_a = 1.155$ and $r_w^{cr} / r_a = 1.168$ for $r_{s1} / r_a = 0.5$, $r_{s2} / r_a = 1.098$ and $r_w^{cr} / r_a = 1.101$ for $r_{s1} / r_a = 0.7$, and $r_{s2} / r_a = 1.0333$ and $r_w^{cr} / r_a = 1.0334$ for $r_{s1} / r_a = 0.5$. As one can see in Fig. 5.25 they almost coincide when r_{s1} is close to r_a, while for smaller r_{s1} / r_a the gap between them increases.

The behaviour of eigen-functions change drastically as ideal wall position r_w / r_a crosses the critical value r_w^{cr} / r_a. In Fig. 5.26 the $m = 2$ perturbation of the poloidal magnetic flux $\psi_N = \psi / \psi_s$ is plotted versus normalized radius r / r_a for configuration with reversed shear $\alpha = -1$ and an ideal wall at r_w / r_a = 1.160, 1.166, 1.167, 1.170 and 1.180. Rational surface is located at $r_s / r_a = 0.5$ and corresponding critical ideal wall radius at $r_w^{cr} / r_a = 1.168$. When r_w approaches r_w^{cr} value of ψ at the edge grows. For $r_w > r_w^{cr}$ it changes the sign and as r_w increases further, $|\psi(r_a)|$ decreases.

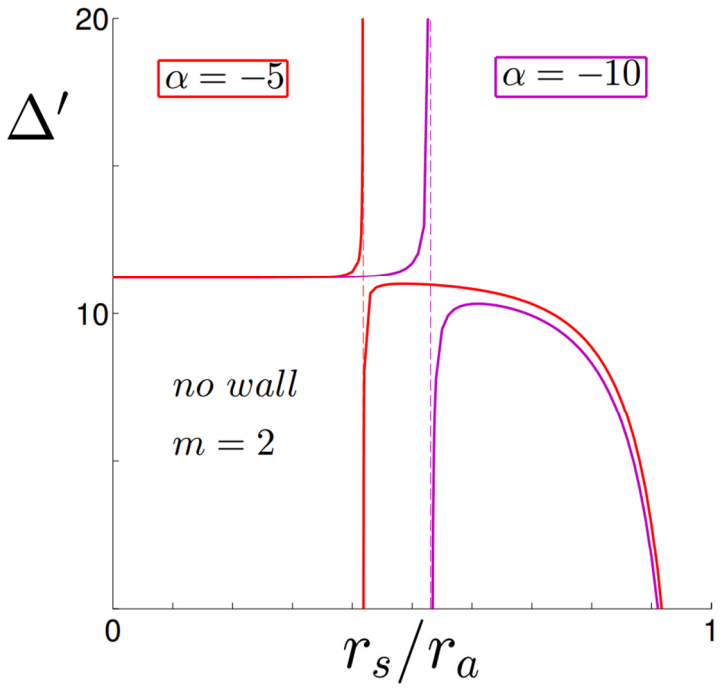

Fig. 5.22. Dependencies of Δ' on the position of the rational surface r_s / r_a for no wall configuration, $m=2$ mode, and parabolic current profiles with $\alpha=-5$ (red curves) and $\alpha=-10$ (purple curves). Dashed vertical lines indicate corresponding values of r_s / r_a where $\Delta' \to \infty$.

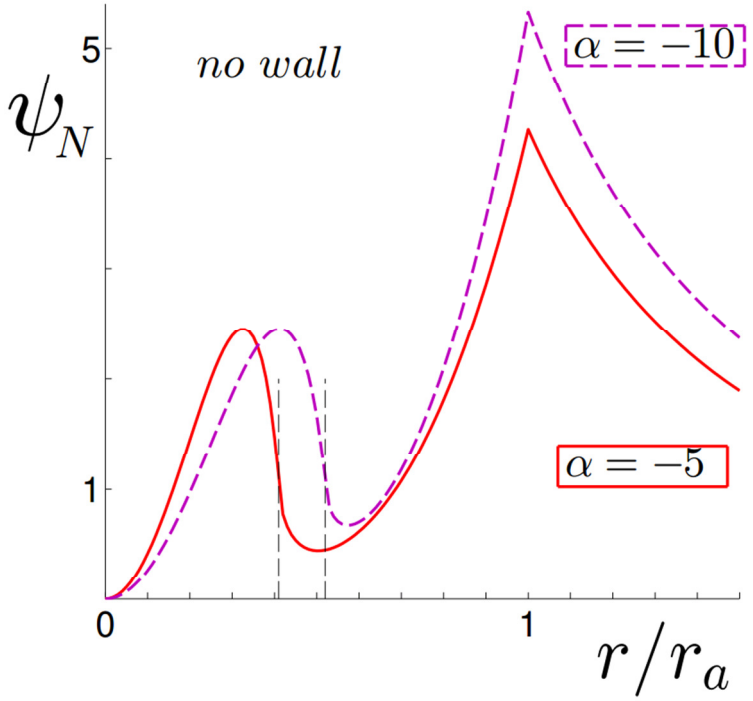

Fig. 5.23. The $m=2$ perturbation of the poloidal magnetic flux $\psi_N = \psi/\psi_s$ normalized on its value at the rational surface versus normalized radius r/r_a for configuration with no wall. Red solid curve: $\alpha=-5$ and $r_s/r_a = 0.41$. Purple dashed line: $\alpha=-10$ and $r_s/r_a = 0.52$.

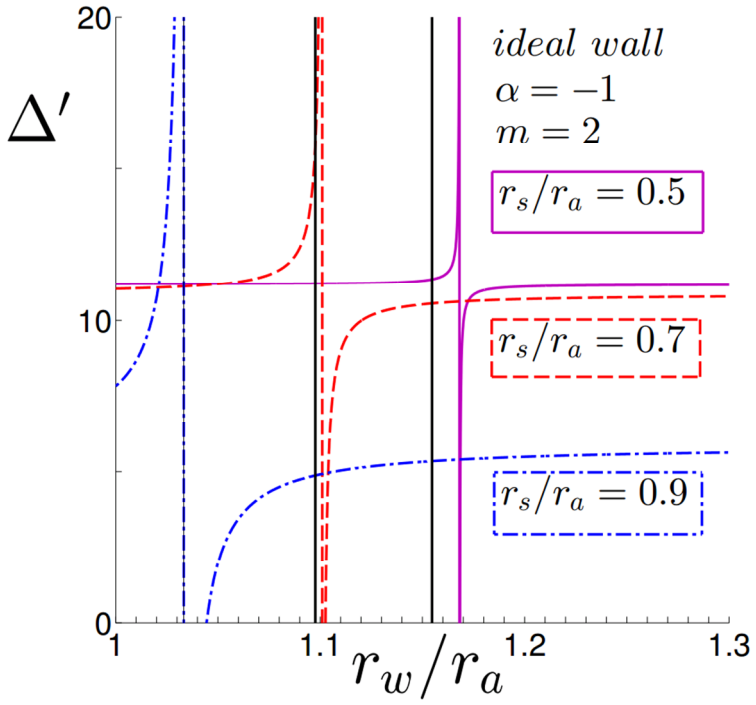

Fig. 5.24. Dependencies of Δ' on the position of the ideal wall r_w / r_a for parabolic current profile with $\alpha = -1$ and $m = 2$ mode with rational surface at $r_{s1} / r_a = 0.5$ (purple solid), $r_{s1} / r_a = 0.7$ (red dashed) and $r_{s1} / r_a = 0.9$ (blue dash-dotted curve). Black solid vertical lines indicate corresponding values of second rational surface r_{s2} / r_a. For the case $r_s / r_a = 0.9$ it almost coincides with r_w^{cr} / r_a.

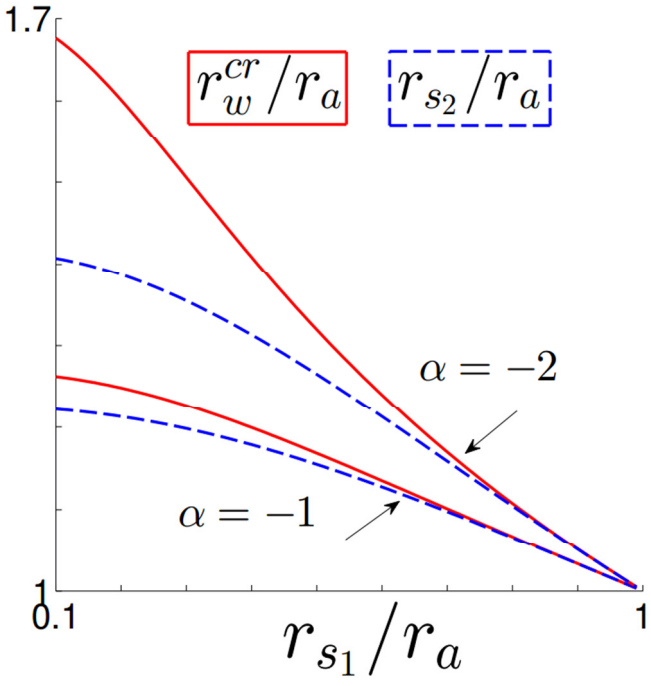

Fig. 5.25. The critical ideal wall r_w^{cr} / r_a (red solid) and second rational surface radii r_{s2} / r_a (blue dashed curves) versus the position of the first rational surface r_{s1} / r_a for $m = 2$ mode, and parabolic current profiles with $\alpha = -1$ and $\alpha = -2$ as indicated in the plot.

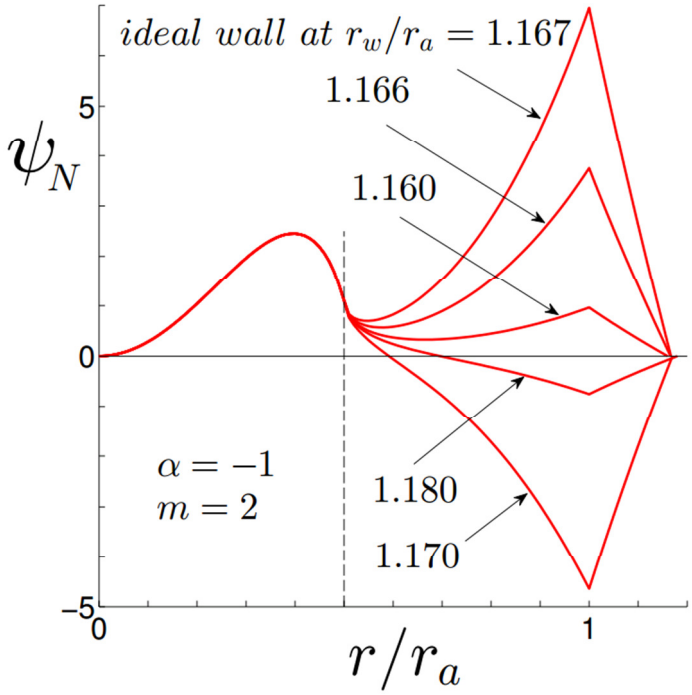

Fig. 5.26. The $m=2$ perturbation of the poloidal magnetic flux $\psi_N = \psi/\psi_s$ normalized on its value at the rational surface versus normalized radius r/r_a for configuration with reversed shear $\alpha=-1$ and an ideal wall at $r_w/r_a = 1.160$, 1.166, 1.167, 1.170 and 1.180. Rational surface position $r_s/r_a = 0.5$ and corresponding critical ideal wall radius $r_w^{cr}/r_a = 1.168$.

5.4.5. Rotational stabilization for $\alpha < 0$

The growth rate of locked tearing modes almost does not affected by the presence of a resistive wall. But sufficiently fast plasma rotation makes the resistive wall to act as if it been ideal one. This is illustrated in Fig. 5.27, where the growth rate $\gamma_N = \gamma_R \tau_w$ of $m/n = 2/1$ mode is plotted versus the wall position. For $\Omega_N \equiv \Omega\tau_w = 0$ (blue dotted line) the solution is negligibly influenced by the resistive wall, as plasma frequency grows the solution tends to mimic the ideal case shown by red solid curve. Depending on the resistive wall radius plasma rotation can either stabilize or destabilize the mode.

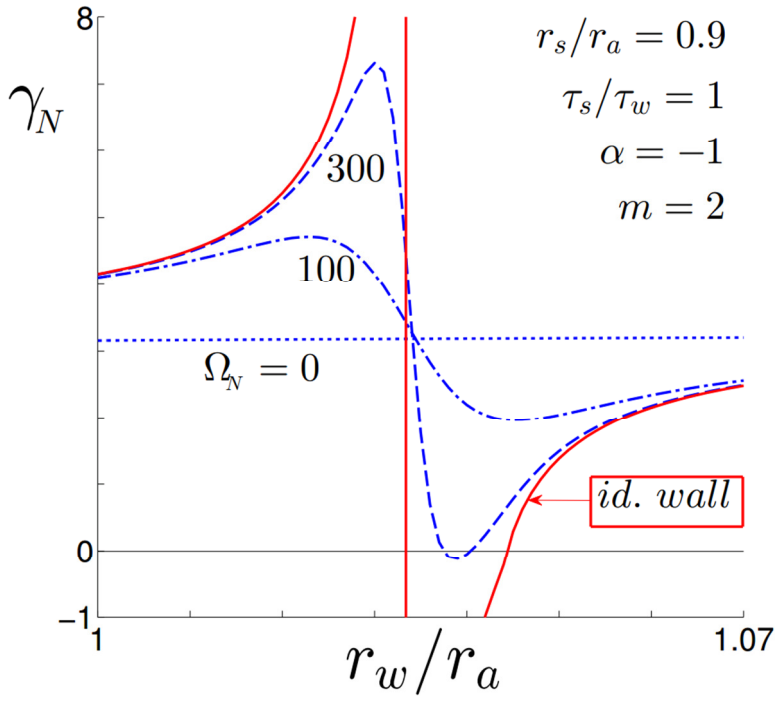

Fig. 5.27. Growth rate $\gamma_N = \gamma_R \tau_w$ of $m/n = 2/1$ mode versus resistive wall position for different plasma rotational frequency $\Omega_N \equiv \Omega\tau_w = 0$ (blue dotted), 100 (blue dash-dotted) and 300 (blue dashed curve). Red solid curve corresponds to the ideal wall. The plot is done for $\alpha = -1$, $\tau_s/\tau_w = 1$ and $r_s/r_a = 0.9$.

5.5. Double tearing mode

If two resistive layers of the same mode are sufficiently close to each other, then constant-ψ approximation is invalid [62]. We assume that the distance between two rational surfaces is large enough to justify the use of Δ' formalism.

Let us consider a configuration shown in Fig. 5.9 b. The solutions in the gap, when it filled with resistive plasma, are determined by (5.16) and (5.17). The matching conditions at rational surfaces are

$$\Delta'_1 = {}_1\Delta'_{in}, \tag{5.47}$$

$$\Delta'_2 = {}_2\Delta'_{in}, \tag{5.48}$$

with

$$\Delta_1' = \left.\frac{r\psi_e'}{\psi_e}\right|_{s1} - \left.\frac{r\psi_i'}{\psi_i}\right|_{s1}, \tag{5.49}$$

$$\Delta_2' = \left.\frac{r\psi_{g2}'}{\psi_{g2}}\right|_{s2} - \left.\frac{r\psi_{g1}'}{\psi_{g1}}\right|_{s2}, \tag{5.50}$$

where subscripts $s1$ and $s2$, refer to the first and the second rational surface positions, respectively. Parameters Δ_{in}' are given by

$${}_1\Delta_{in}' = \frac{\bar{\gamma}_1^{5/4}}{|S_1|^{1/2}}, \tag{5.51}$$

$${}_2\Delta_{in}' = \frac{\bar{\gamma}_2^{5/4}}{|S_2|^{1/2}}, \tag{5.52}$$

with

$$\bar{\gamma}_1 = (\gamma - i\Omega_1)\tau_{s1}, \tag{5.53}$$

$$\bar{\gamma}_2 = (\gamma - i\Omega_2)\tau_{s2}, \tag{5.54}$$

$$S_1 = \left.\frac{rq'}{q}\right|_{s1}, \tag{5.55}$$

$$S_2 = \left.\frac{rq'}{q}\right|_{s2}, \tag{5.56}$$

where τ_{s1} and τ_{s2} are determined by (5.14) , (5.15) and the plasma resistivity η_{pl} corresponding to the resonance radii. Plasma rotational frequencies Ω_1 and Ω_2 (5.5) are assumed to be also different.

Following the same matching procedure as in 6.4. we arrive at the dispersion relation for the double tearing mode

$${}_1\Delta_{in}' = 4\pi \frac{C_e \cot(\pi B) + \delta \cot(\pi A)}{C_e + \delta}, \tag{5.57}$$

where

$$C_e = -z^{-\bar{m}} \left. \frac{2F_2' + (\bar{m} + r\psi_e'/\psi_e) z F_2}{2F_1' + (-\bar{m} + r\psi_e'/\psi_e) z F_1} \right|_a , \tag{5.58}$$

$$\left. \frac{r\psi_e'}{\psi_e} \right|_a = \left. \frac{r\psi_{g1}'}{\psi_{g1}} \right|_a - f_\alpha , \tag{5.59}$$

$$f_\alpha = \frac{4}{1-(r_{s1}/r_a)^2} \frac{1-\alpha}{\alpha} , \tag{5.60}$$

$$\left. \frac{r\psi_{g1}'}{\psi_{g1}} \right|_a = -m + 2m \frac{C_{g1}(r_a/r_{s2})^{2m}}{1 + C_{g1}(r_a/r_{s2})^{2m}} , \tag{5.61}$$

$$C_{g1} = \left. \frac{m + r\psi_{g2}'/\psi_{g2} - {}_2\Delta_{in}'}{m - r\psi_{g2}'/\psi_{g2} + {}_2\Delta_{in}'} \right|_{s2} , \tag{5.62}$$

$$\left. \frac{r\psi_{g2}'}{\psi_{g2}} \right|_{s2} = -m + 2m \frac{C_{g2}(r_{s2}/r_w)^{2m}}{1 + C_{g2}(r_{s2}/r_w)^{2m}} , \tag{5.63}$$

$$C_{g2} = -\frac{\Gamma_m}{2m + \Gamma_m} , \tag{5.64}$$

with Γ_m given by (3.11).

For $\tau_{s1}/\tau_w \geq 1$ the mode frequency ω is almost frozen into the fluid at the first rational surface, $\omega \approx \Omega_1$. When the mode frequency ω and the plasma rotation at the second rational surface Ω_2 are of the same order $\Omega_2 \approx \omega$, results differ negligibly from the case with vacuum in the gap. Therefore, if $\Omega_2 \approx \omega$, double tearing mode can be stabilized by rotation in the same range of parameters as for the single tearing mode. For $\tau_{s2}|\omega - \Omega_2| >> 1$, the second rational surface acts as if it been an ideal wall. Since $r_{s2} < r_w^{cr}$, it always leads to the destabilization.

5.6. Conclusions

In the presence of the resistive wall, both RWMs and tearing modes can be stabilized by plasma rotation in the range of parameters where the ideal wall provides their stability.

Harmonics are almost frozen into the plasma when, $\tau_s/\tau_w \geq 1$, which is an expected result for tearing modes. In contrast, the majority of experimental observations on RWM rotational

stabilization indicates that their frequencies are almost locked to the wall, $\omega\tau_w \approx 1$, while the plasma rotates several orders of magnitude faster [48]. In the analyzed model such result can be obtained only under the assumption that $\tau_s / \tau_w << 1$, which corresponds to a very cold plasma $< 10eV$. On the other hand, some experimental results [45] show that close to the ideal wall limit the RWM frequency is high, $\omega\tau_{sk} \approx 1$, and comparable with the plasma rotation, which is in agreement with our results.

The flattening of the equilibrium current profile after a disruption almost vanishes the amplitude of tearing modes outside the plasma and, therefore, they do not contribute to the electromagnetic force acting on the wall. In contrast, for flatter current distributions the growth rate and instability limits of RWMs enlarge, that can lead to stronger loads on the vessel.

For profiles with negative magnetic shear the ideal wall can be either stabilizing or destabilizing, depending on its position. Correspondingly, being replaced by a wall with a finite conductivity in combination with plasma rotation it provides either stabilization or destabilization.

The double tearing mode is found to be destabilized by the differential rotation. If the plasma rotational frequencies at two rational surfaces are close to each other, then the mode can be stabilized in the presence of a nearby resistive wall.

VI. TEARING MODE LOCKING

6.1. Electromagnetic torque acting on the plasma

The interaction of the plasma with eddy currents in the resistive wall exerts electromagnetic torque on the plasma and reduces its poloidal and toroidal momenta [63, 64].

By definition, the poloidal electromagnetic torque exerted on the plasma cylinder is

$$T^{\theta} \equiv \int \mathbf{e}_z \cdot \mathbf{r} \times (\mathbf{j} \times \mathbf{B}) dV , \tag{6.1}$$

with integration performed over the plasma or larger volume including vacuum. Using the identity

$$\mathbf{e}_z \cdot \mathbf{r} \times (\mathbf{j} \times \mathbf{B}) = -\frac{\partial}{\partial \theta} \frac{\mathbf{B}^2}{2\mu_0} + \frac{1}{\mu_0} \nabla r B_\theta \mathbf{B} , \tag{6.2}$$

from (6.1), we find

$$T^{\theta} = \frac{1}{\mu_0} \int_S r B_\theta \mathbf{B} \cdot d\mathbf{S} , \tag{6.3}$$

where S is the axisymmetric surface in the vacuum at the inner side of the wall. Due to the symmetry (6.3) reduces to

$$T^{\theta} = \frac{1}{\mu_0} \int_S r b_\theta \mathbf{b} \cdot d\mathbf{S} . \tag{6.4}$$

From (6.4) we arrive at

$$T^{\theta} = \frac{r_w S_w}{\mu_0} \langle b_r b_\theta \rangle_{\theta,\varphi} , \tag{6.5}$$

where $S_w = 4\pi^2 r_w R$, and

$$\langle f \rangle_{\theta,\varphi} \equiv \frac{1}{4\pi^2} \int_0^{2\pi} d\theta \int_0^{2\pi} f \, d\varphi . \tag{6.6}$$

For

$$b_r = \sum b_{mn}(r,t) \exp(im\theta - in\varphi) , \tag{6.7}$$

and b_θ of the same form, we find

$$\left\langle b_r b_\theta \right\rangle_{\theta,\varphi} = \sum_{m\geq 0, n>0} (b^*_{mn} b_{\theta,mn} + b_{mn} b^*_{\theta,mn}), \tag{6.8}$$

where the star means the complex conjugate. Then

$$T^\theta = \sum_{m\geq 0, n>0} T^\theta_{mn}, \tag{6.9}$$

with

$$T^\theta_{mn} = \frac{r_w S_w}{\mu_0} (b^*_{mn} b_{\theta,mn} + b_{mn} b^*_{\theta,mn}). \tag{6.10}$$

As it was shown in [63], the toroidal electromagnetic torque exerted on the plasma cylinder is

$$T^z = \sum_{m\geq 0, n>0} T^z_{mn}, \tag{6.11}$$

with

$$T^z_{mn} = \frac{R S_w}{\mu_0} (b^*_{mn} b_{z,mn} + b_{mn} b^*_{z,mn}). \tag{6.12}$$

In vacuum $\mathbf{b} = \nabla\phi$, therefore

$$b_z = -\frac{nr}{mR} b_\theta, \tag{6.13}$$

and comparing (6.10) and (6.12) one can conclude that

$$T^z_{mn} = -\frac{n}{m} T^\theta_{mn}. \tag{6.14}$$

Using (3.26), we find that

$$T^z_{mn} = -\frac{inS_w}{\mu_0 r_w} |\psi|^2 \left(\frac{r\psi'}{\psi} - \frac{r\psi'^*}{\psi^*} \right)\Bigg|_{w-}, \tag{6.15}$$

with omitted subscript mn for ψ. Using (3.10), from (6.15) we arrive at

$$T^z_{mn} = \frac{inS_w}{\mu_0 r_w} |\psi_{w-}|^2 \left(\Gamma_m - \Gamma^*_m\right), \tag{6.16}$$

where ψ_{w-} is the value of ψ at the inner side of the wall r_w in vacuum.

For the thin wall approximation (3.16), (6.16) reduces to

$$T_{mn}^{z} = -\frac{2nS_w}{\mu_0 r_w}\left|\psi_{w-}\right|^2 n\omega\tau_w . \tag{6.17}$$

For the thick wall approximation (3.19), (6.16) reduces to

$$T_{mn}^{z} = -\frac{nS_w}{\mu_0 d_w}\left|\psi_{w-}\right|^2 \sqrt{\frac{2n\omega\tau_{sk}}{\hat{\mu}}} . \tag{6.18}$$

Let us find the relation between ψ_{w-} and ψ_{s+} - the value of ψ at the outer side of the magnetic island. From continuity of ψ at the plasma-vacuum interface, (3.3), (5.31) and (5.43), it follows that

$$\frac{\psi_{w-}}{\psi_{s+}} = \frac{\psi_g(r_w)}{\psi_g(r_a)} \cdot \frac{\psi_e(r_a)}{\psi_e(r_{s+})}, \tag{6.19}$$

with

$$\frac{\psi_g(r_w)}{\psi_g(r_a)} = \left(\frac{r_a}{r_w}\right)^m \frac{2m}{2m+\Gamma_m\left[1-(r_a/r_w)^{2m}\right]}, \tag{6.20}$$

and

$$\frac{\psi_e(r_a)}{\psi_e(r_{s+})} = \frac{(C_e z^{\overline{m}/2}F_1 + z^{-\overline{m}/2}F_2)\big|_a}{(C_e z^{\overline{m}/2}F_1 + z^{-\overline{m}/2}F_2)\big|_{s+}}, \tag{6.21}$$

where subscript $s+$ refers to the outer side of the island $r_{s+} = r_s + W/2$,

$$C_e = -z^{-\overline{m}} \left.\frac{2F_2' + (\overline{m} + r\psi_e'/\psi_e)zF_2}{2F_1' + (-\overline{m} + r\psi_e'/\psi_e)zF_1}\right|_a , \tag{6.22}$$

$$\left.\frac{r\psi_e'}{\psi_e}\right|_a = \left.\frac{r\psi_g'}{\psi_g}\right|_a - f_\alpha , \tag{6.23}$$

$$f_\alpha = \frac{4}{1-(r_s/r_a)^2}\frac{1-\alpha}{\alpha}, \tag{6.24}$$

$$\left.\frac{r\psi_g'}{\psi_g}\right|_a = -m\frac{2m+\Gamma_m\left[1+(r_a/r_w)^{2m}\right]}{2m+\Gamma_m\left[1-(r_a/r_w)^{2m}\right]}. \tag{6.25}$$

To mimic a peaked current profile one can use the vacuum solution (3.3) for the external with respect to the island plasma region, in this case instead of (6.19) we find

$$\frac{\psi_{w-}}{\psi_{s+}} = \frac{\psi_g(r_w)}{\psi_g(r_{s+})}, \tag{6.26}$$

with the outer side of the island located at $r_{s+} = r_s + W/2$ and

$$\frac{\psi_g(r_w)}{\psi_g(r_{s+})} = \left(\frac{r_{s+}}{r_w}\right)^m \frac{2m}{2m + \Gamma_m\left[1-(r_{s+}/r_w)^{2m}\right]}. \tag{6.27}$$

With the drop of the perturbation amplitude given by (6.26) and for the slow mode rotation, such that $\tau_w\omega \approx 1$, Γ_m is given by (3.18), and (6.16) reduces to

$$T^z_{mn} \approx -\frac{2nS_w}{\mu_0 r_w}\left(\frac{r_{s+}}{r_w}\right)^{2m} \left|\psi_{s+}\right|^2 n\omega\tau_w, \tag{6.28}$$

which predicts the linear dependence of the torque on $\omega\tau_w$.

For fast modes, such that $\tau_{sk}\omega >> 1$, Γ_m is given by (3.20), and (6.16) reduces to

$$T^z_{mn} \approx -\frac{nS_w d_w}{\mu_0 r_w^2}\left(\frac{r_{s+}}{r_w}\right)^{2m} \frac{4m^2}{\left[1-(r_{s+}/r_w)^{2m}\right]^2}\left|\psi_{s+}\right|^2 \sqrt{\frac{2}{n\omega\tau_{sk}}}, \tag{6.29}$$

which predicts the decrease of the torque with increase of the frequency as $(\omega\tau_{sk})^{-1/2}$.

For $\tau_{sk}\omega >> 1$, the thin formula (3.18) underestimates the torque, indeed, allowing for (6.27), (3.18) and (3.20), from (6.16) we find

$$\frac{T^z_{mn}(thin)}{T^z_{mn}(thick)} \approx \sqrt{\frac{2}{n\omega\tau_{sk}}}. \tag{6.30}$$

To be noticed is that the amplitude ψ_{w-} in (6.16), (6.17) and (6.18) also depends on $\hat{\mu}$. For $\tau_{sk}\omega >> 1$, from (6.18), (6.27) and (3.19), we find

$$T^z_{mn}(\hat{\mu}) \approx \sqrt{\hat{\mu}}\, T^z_{mn}(1), \tag{6.31}$$

where $T^z_{mn}(1)$ is T^z_{mn} of the form (6.18) calculated for $\hat{\mu} = 1$.

For the following numerical calculations of the torque we use the normalized quantity

$$T^z_N = -\frac{\mu_0 r_w T^z_{mn}}{nS\left|\psi_{s+}\right|^2}. \tag{6.32}$$

In Fig. 6.1 the normalized toroidal torque T^z_N is plotted versus mode rotational frequency $n\omega\tau_{sk}$ for Γ_m determined by the exact solution (3.14) (black solid line), by the thin wall approximation (3.18) (blue dashed line) and the thick wall formula (3.20) (red dash-dotted line). For

$n\omega\tau_{sk}=10$ the thin formula (3.18) gives $\sqrt{5}$ lower value for the torque in agreement with the prediction (6.30), while for $n\omega\tau_{sk}<1$ it serves as a good estimate. The thick wall approximation (3.20) can be used for $n\omega\tau_{sk}>>1$ only, otherwise it underestimates the torque. If the initial tearing mode frequency is high, such that $n\omega_{in}\tau_{sk}>>1$, then the exact formula (3.14) must be used. For the parameters of RFX-mod Upgrade tokamak $\tau_{sk}=0.6$ ms, therefore, $\omega_{sk}\tau_{sk}=1$ corresponds to $\nu_{sk}\equiv\omega_{sk}/2\pi=265$ Hz, while the typical initial frequency is expected to be of the same order of magnitude as for RFX-mod, $\omega_{in}\tau_{sk}=3-4$ kHz. For DIII-D $\tau_{sk}=0.1$ ms [53], $\nu_{sk}=1.6$ kHz and $\omega_{in}\tau_{sk}>5$ kHz [65]. In both above cases, $\omega_{in}>>\omega_{cr}$, the thin wall approximation underestimates the torque and, therefore, overestimates the locking time.

The torque becomes stronger for a shorter distance between the island and the wall, this is illustrated in Fig. 6.2 for different wall positions and in Fig. 6.3 for various island widths. For current profiles with smaller positive α the mode amplitude drops steeper across the external ideal plasma region reducing the mode interaction with the wall, therefore, decreasing the torque. This is shown in Fig. 6.4 for $\alpha=0.1$, 0.5 and 1.

Dependence of the torque on the wall magnetic permeability is analyzed in Fig. 6.5. While for $n\omega\tau_{sk}<<1$ the torque decreases for higher values of $\hat{\mu}$, in the limit $n\omega\tau_{sk}>>1$ the torque increases for larger $\hat{\mu}$ in agreement with the prediction (6.31). Even for intermediate values of $\hat{\mu}=2-4$, the effect of the wall ferromagnetism on the dynamics of the mode locking must be strong.

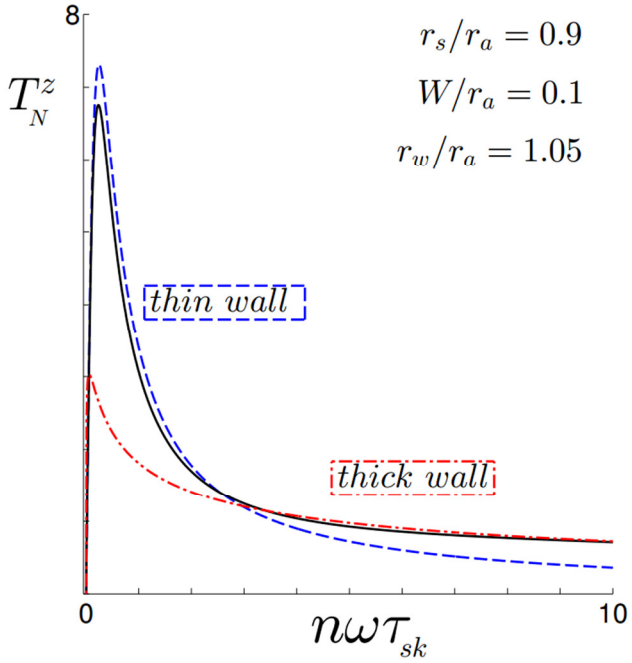

Fig. 6.1. Dependencies of T_N^z on the $m/n=2/1$ mode rotational frequency $n\omega\tau_{sk}$ for the magnetically thin wall (3.18) (blue dashed line), the thick wall (3.20) (red dash-dotted line) and without limitations on the wall magnetic thickness (3.14) (black solid curve). The parameters for the calculation are: $r_s/r_a=0.9$, $W/r_a=0.1$, $r_w/r_a=1.05$, $d_w/r_w=0.02$, $\alpha=1$ and $\hat{\mu}=1$.

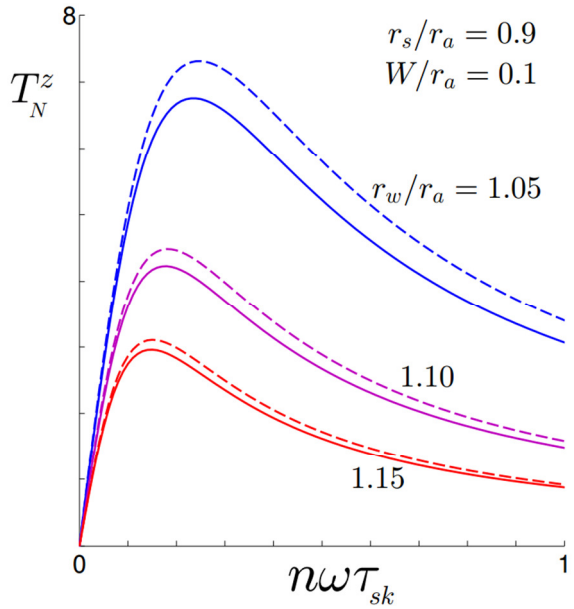

Fig. 6.2. Dependencies of T_N^z on the $m/n=2/1$ mode rotational frequency $n\omega\tau_{sk}$ for different wall positions: r_w/r_a = 1.05 (blue), 1.10 (purple) and 1.15 (red curves). Dashed lines show solutions for the magnetically thin wall (3.18) and solid curves correspond to the exact formula (3.14). The parameters for the calculation are: $r_s/r_a=0.9$, $W/r_a=0.1$, $d_w/r_w=0.02$, $\alpha=1$ and $\hat{\mu}=1$.

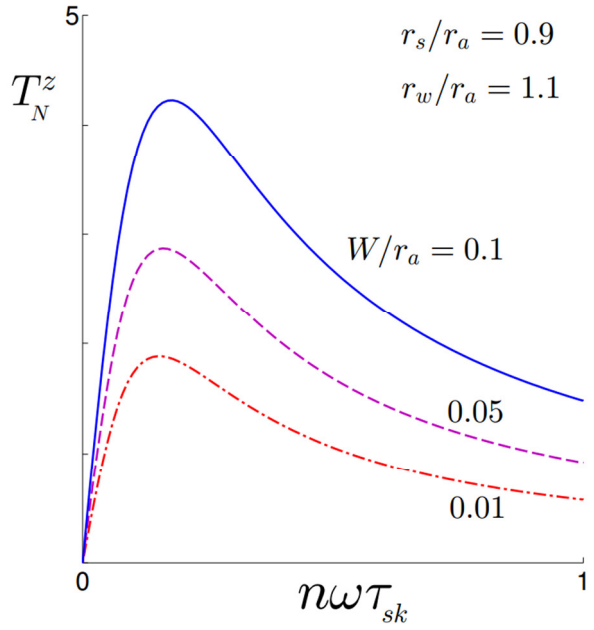

Fig. 6.3. Dependencies of T_N^z on the $m/n=2/1$ mode rotational frequency $n\omega\tau_{sk}$ for different magnetic island width: $W/r_a=0.01$ (red dash-dotted), 0.05 (purple dashed) and 0.1 (blue solid curve). The parameters for the calculation are: $r_s/r_a=0.9$, $r_w/r_a=1.1$, $d_w/r_w=0.02$, $\alpha=1$ and $\hat{\mu}=1$.

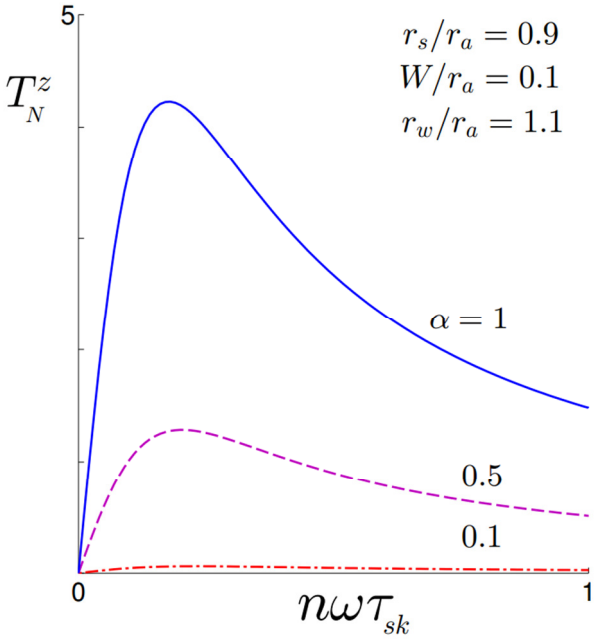

Fig. 6.4. Dependencies of T_N^z on the $m/n=2/1$ mode rotational frequency $n\omega\tau_{sk}$ for different values of the current profile parabolicity: $\alpha=0.1$ (red dash-dotted), 0.5 (purple dashed) and 1 (blue solid curve). The parameters for the calculation are: $r_s/r_a=0.9$, $W/r_a=0.1$, $r_w/r_a=1.1$ $d_w/r_w=0.02$, $\alpha=1$ and $\hat{\mu}=1$.

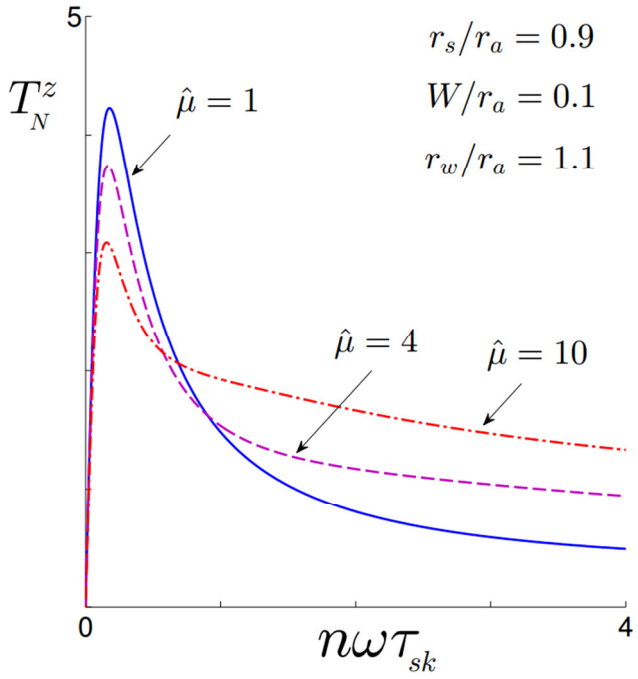

Fig. 6.5. Dependencies of T_N^z on the $m/n = 2/1$ mode rotational frequency $n\omega\tau_{sk}$ for different relative magnetic permeability of the wall: $\hat{\mu} = 1$ (blue solid), 4 (purple dashed) and 10 (red dash-dotted curve). The parameters for the calculation are: $r_s / r_a = 0.9$, $W / r_a = 0.1$, $r_w / r_a = 1.1$ $d_w / r_w = 0.02$ and $\alpha = 1$.

6.2. Magnetic island evolution equation

Under the assumption of the continuity of ψ across the reconnection region, the non-linear growth of the magnetic island is governed by [7, 66]

$$\tau_R \frac{dW / r_s}{dt} = \Delta'_R, \tag{6.33}$$

with

$$\tau_R = \frac{\mu_0 r_s^2}{\eta_{pl}}, \tag{6.34}$$

and

$$\Delta'_R = \mathrm{Re}\left(\frac{r\psi'_e}{\psi_e}\bigg|_{s+} - \frac{r\psi'_i}{\psi_i}\bigg|_{s-} \right), \tag{6.35}$$

where for the parabolic current profile (2.18) logarithmic derivatives are determined by (5.34) and (5.35), and subscripts $s+$ and $s-$ refer to the outer $r_{s+} = r_s + W/2$ and inner $r_{s-} = r_s - W/2$ borders of the island, respectively. The island width W is related to ψ through

$$W = 4\left| \frac{q}{q'} \frac{\psi}{B_\theta} \right|^{1/2}_s, \tag{6.36}$$

where subscript s refers to the rational surface position $r = r_s$.

The modified versions of (6.33) with additional terms was reviewed in [67]. Here, we are mostly interested in the effect of the boundary conditions on the mode locking, that is why the simplest form of the island evolution equation is used.

To mimic a peaked current profile one can use the vacuum solution to calculate $r\psi'_e / \psi_e$ at the outer side of the island, in this case instead of (5.35) we find

$$\frac{r\psi'_e}{\psi_e}\bigg|_{s+} = -m \frac{2m + \Gamma_m \left[1 + (r_{s+} / r_w)^{2m} \right]}{2m + \Gamma_m \left[1 - (r_{s+} / r_w)^{2m} \right]}, \tag{6.37}$$

with the outer side of the island located at $r_{s+} = r_s + W/2$.

The parameter Δ'_R is plotted in Fig. 6.6 versus the $m/n=2/1$ island width W/r_a for different mode frequencies. The Δ'_R is calculated for parabolic current profile (2.18) with $\alpha=1$, that corresponds to $r\psi'_e/\psi_e$ of the form (5.35). For $\omega\tau_{sk}>0.5$, results vary insignificantly and are shown by one dotted black curve. The island saturates, $W=W_s$, when $\Delta'_R=0$. Due to the wall-mode interaction the frequency decreases and the size of the saturated island W_s becomes larger. The dependencies of Δ'_R on W and resulting W_s are very sensitive to the assumption on the equilibrium current profile [68]. More peaked, in comparison with the parabolic profile, current distribution can give larger saturated width, to mimic this effect we treat the space between the outer island border and the wall as vacuum, in this case $r\psi'_e/\psi_e$ has to be calculated by (6.37) instead of (5.35). In Fig. 6.7 one can see the difference between Δ'_R for peaked (blue curves) and parabolic (black lines) current profiles. For the peaked current distribution Δ'_R and W_s are larger, therefore, one can expect that the mode locking should be faster, indeed, the simulations in Section 7.5. confirm this guess (see Figs. 6.12 and 6.13).

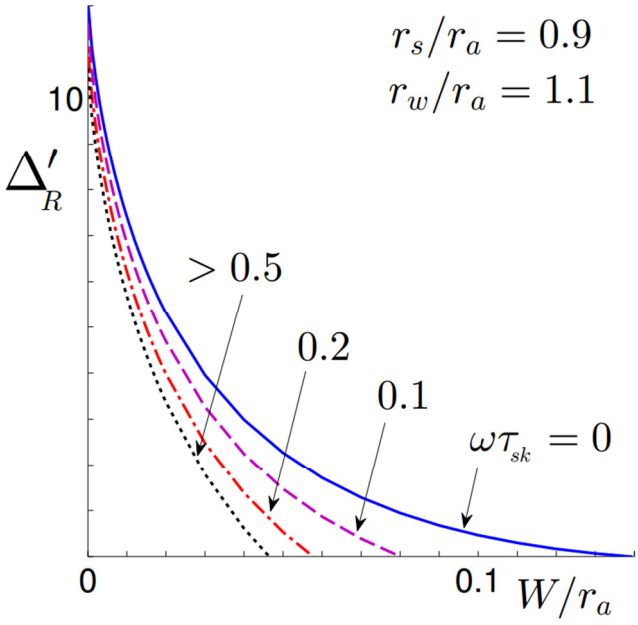

Fig. 6.6. Dependencies of Δ'_R on the $m/n=2/1$ island width W/r_a for parabolic current profile and different mode frequencies $\omega\tau_{sk}$ = 0 (solid blue), 0.1 (dashed purple), 0.2 (dash-dotted red) and $\omega\tau_{sk} > 0.5$ (dotted black curve). The parameters for the calculation are: $r_s/r_a = 0.9$, $W/r_a = 0.1$, $r_w/r_a = 1.1$, $d_w/r_w = 0.02$, $\hat{\mu} = 1$ and $\alpha = 1$.

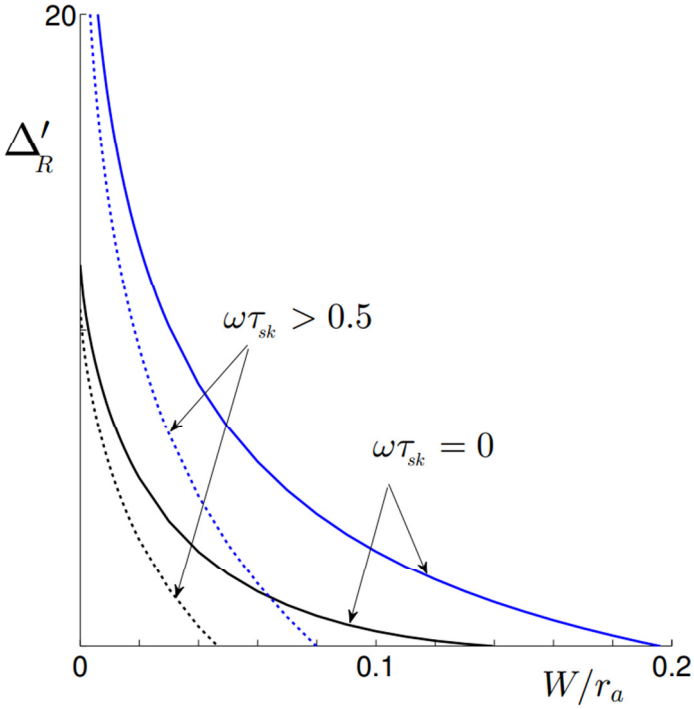

Fig. 6.7. Dependencies of Δ'_R on the $m/n=2/1$ island width W/r_a for $\omega\tau_{sk} = 0$ (solid) and $\omega\tau_{sk} > 0.5$ (dotted lines). The upper set of blue curves corresponds to the peaked current profile and the lower set of black curves to the parabolic one. The parameters for the calculation are: $r_s/r_a = 0.9$, $W/r_a = 0.1$, $r_w/r_a = 1.1$, $d_w/r_w = 0.02$, $\hat{\mu} = 1$ and $\alpha = 1$.

6.3. Angular momentum equation

The integral torque balance was analyzed in [64]. As the sources of the plasma angular momentum can serve the neutral beam injection (NBI) [69] and interaction of the edge plasma with the scrape-off-layer (SOL) plasma [64, 70]. The plasma viscosity and the poloidal flow damping [71] can only redistribute the momentum within the plasma, but does not affect its total amount. The electromagnetic interaction of the plasma with the wall and/or error fields is the main sink of the plasma angular momentum [63].

For the axisymmetric cylindrical geometry with vacuum in the gap between plasma and the wall, and in the absence of any momentum sources and error fields, the evolution of the total plasma toroidal momentum is governed by

$$4\pi^2 R^2 \int_0^a \rho \frac{dV_z}{dt} r dr = T^z, \tag{6.38}$$

where T^z is given by (6.11). We assume that the torque is applied at the rational surface only, the velocity is constant across the island width and does not change beyond the magnetic island, then from (6.38) we find

$$4\pi^2 R^2 r_s W \rho \frac{dV_z}{dt} = T^z_{mn}, \tag{6.39}$$

where T^z_{mn} is given by (6.12). Under the assumption that the mode is frozen into the fluid and in neglecting the poloidal flow, the mode rotational frequency ω is related to the plasma toroidal velocity V_z through

$$\omega = \frac{nV_z}{R}. \tag{6.40}$$

Allowing for (6.40), from (6.39) we arrive at the mode frequency evolution equation

$$\frac{d\omega}{dt} = \frac{nT^z_{mn}}{4\pi^2 R^3 r_s W \rho}. \tag{6.41}$$

6.4. Tearing mode locking

The dynamics of the tearing mode locking [72] is governed by (6.41) and the Rutherford's equation (6.33). The last one can be roughly approximated by

$$\tau_R \frac{dW/r_s}{dt} = \Delta'_R(0)(1 - W/W_s), \tag{6.42}$$

where $\Delta'_R(0)$ is the value of Δ'_R at $W = 0$. The solution of (6.42) is

$$W = W_s(1 - \exp(-t/\tau_{sat}), \tag{6.43}$$

where

$$\tau_{sat} = \frac{\tau_R}{\Delta'_R(0)} \frac{W_s}{r_s}. \tag{6.44}$$

If the mode locking time τ_{lock} is much bigger than the characteristic time of the island growth τ_{sat}, $\tau_{lock} >> \tau_{sat}$, then W_s in (6.42) is determined by the saturated island size W_s^{in} at the initial frequency $\omega = \omega_{in}$, in the opposite limit, $\tau_{lock} << \tau_{sat}$, W_s is given by the saturated island width W_s^0 for the locked mode, $\omega = 0$.

Allowing for (6.36) and (6.12), from (6.41) we find

$$\frac{d\omega}{dt} = \frac{i}{256} \frac{n^4}{m^2} \frac{W^3 r_a^2}{R^4 r_s} \left(\frac{rq'}{q} \right)_s^2 \left| \frac{\psi_{w-}}{\psi_{s+}} \right|^2 \frac{\Gamma_m - \Gamma_m^*}{\tau_A^2}, \tag{6.45}$$

where the drop of the mode amplitude $|\psi_{w-}/\psi_{s+}|$ also depends on the island width and is given by (6.19) for parabolic or by (6.26) for peaked current profile. The results of numerical solutions of equations (6.33) and (6.45) are presented in the next section.

6.5. Results for RFX-mod and RFX-mod Upgrade

In the present RFX-mod arrangement the nearest to the plasma wall serves as a vacuum vessel, its position is $r_{w1}/r_a = 1.07$ and the wall time is $\tau_{w1} = 2ms$. With the thickness $d_{w1}/r_{w1} = 0.006$, for the wall skin time we find $\tau_{sk1} \approx 0.012ms$, which for typical mode frequencies gives $\omega\tau_{sk1} << 1$. This justifies the treatment of the vacuum vessel as a magnetically thin wall (3.18). The second wall is a copper shell that serves for MHD stability, its position is $r_{w2}/r_a = 1.12$ and the wall time is $\tau_{w2} = 100ms$. With the thickness $d_{w2}/r_{w2} = 0.006$, for the wall skin time we find $\tau_{sk2} = 0.6ms$, which for typical mode frequencies gives $\omega\tau_{sk2} >> 1$. That is why we start our consideration treating the copper shell without limitations on its magnetic thickness (3.14). However, as we will see later, for the case with the highly-resistive vacuum vessel within the shell, also the last one can be modeled as a thin wall.

For the configuration with a magnetically thin wall between plasma and the second wall, Γ_m in (6.16) and (6.25) is given by

$$\Gamma_m = in\omega\tau_{w1} + \frac{2m(r_{w1}/r_{w2})^{2m}\Gamma_2}{2m + \Gamma_2\left[1-(r_{w1}/r_{w2})^{2m}\right]}, \tag{6.46}$$

$$\Gamma_2 = y_i \frac{K_{m-1}(y_i)I_{m-1}(y_e) - I_{m-1}(y_i)K_{m-1}(y_e)}{K_m(y_i)I_{m-1}(y_e) + I_m(y_i)K_{m-1}(y_e)}, \tag{6.47}$$

$$y_i \equiv \frac{r_{w2}}{d_{w2}}\sqrt{in\omega\tau_{sk2}} \text{ and } y_e \equiv y_i(1+d_{w2}/r_{w2}), \tag{6.48}$$

and instead of r_w one has to use r_{w1}.

In Fig. 6.8 the dependency of T_N^z on the $m/n = 2/1$ mode rotational frequency $n\omega\tau_{sk}$ is plotted for the wall configuration of the RFX-mod with the vacuum vessel inside the copper shell (red curve). To explain the function behavior the results for the vacuum vessel only (black line) and for the copper shell only (blue line) are also shown. For the low frequency $n\omega\tau_{sk} = n\omega\tau_{sk2} << 1$, the vacuum vessel time constant is too small to affect the solution, since

$$\tau_{w1}\omega = \frac{\tau_{w1}}{\tau_{sk2}}\omega\tau_{sk2} \approx 3\omega\tau_{sk2} << 1. \tag{6.49}$$

For $\tau_{sk2}\omega > 1$, the first wall screens partially the second one and the solution is determined mostly by the inner wall. The dotted black curve corresponds to the case with the vacuum vessel and the shell treated as magnetically thin walls. As one can see the difference from the exact solution with Γ_2 of the form (6.47) is very small, therefore, instead of (6.46) one can use

$$\Gamma_m = in\omega\tau_{w1} + \frac{2m(r_{w1}/r_{w2})^{2m} in\omega\tau_{w2}}{2m + in\omega\tau_{w2}\left[1-(r_{w1}/r_{w2})^{2m}\right]}. \tag{6.50}$$

After the new upgrade of the RFX-mod machine the vacuum vessel will be outside the copper shell which allow to increase the plasma radius, the new position of the wall will be $r_w / r_a = 1.05$, with the same skin time $\tau_{sk} = 0.6ms$ and the thickness $d_w / r_w = 0.006$. Since the wall time of the vacuum vessel is much smaller than the shell time $\tau_{w1} << \tau_{w2}$, we can exclude it from the analysis when it is located outside the shell.

In Fig. 6.9 the normalized electromagnetic torques (6.32) for configurations of RFX-mod (dashed blue) and RFX-mod Upgrade (solid red curve) are plotted versus the mode rotational frequency $n\omega\tau_{sk}$. For $n\omega\tau_{sk} < 1$, the torque is larger for the new arrangement, but for $n\omega\tau_{sk} > 1$ it is vice versa. The ratio of the torques for two assemblies is shown in Fig. 6.10. For $n\omega\tau_{sk} >> 1$ they differ approximately in ten times. With $\tau_{sk} = 0.6$ ms, $\omega\tau_{sk} = 10$ corresponds to $\nu \equiv \omega/2\pi = 2650$ Hz, which is a typical initial frequency for RFX-mod, therefore one can conclude that the locking time after the upgrade will be roughly an order of magnitude longer. Indeed, the simulation of the locking shown in Fig. 6.11 confirms this estimate based on the comparison of torques for two configurations.

In Figs. 6.12 and 6.13 the dynamics of the locking is presented for the parameters of RFX-mod tokamak and two different current profiles: parabolic (blue dashed) and peaked (red solid curve). For the peaked current distribution the mode locks an order of magnitude faster than for the parabolic one, its locking time is comparable to the island growth time $\tau_{lock} \approx \tau_{sat}$, that is why the island grows almost continuously up to the W_s^0. In contrast, for the parabolic profile, $\tau_{lock} >> \tau_{sat}$, at first, the island saturates at W_s^{in} and only after the locking grows up to W_s^0.

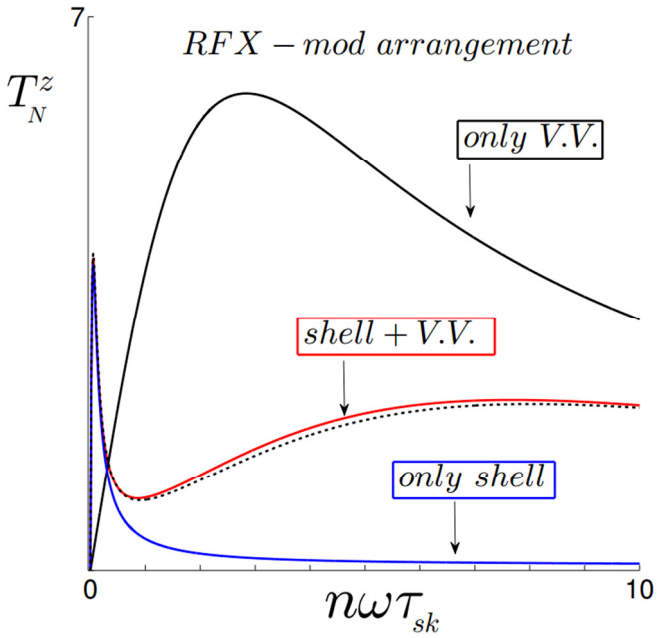

Fig. 6.8. Dependencies of T_N^z on the $m/n=2/1$ mode rotational frequency $n\omega\tau_{sk}$ for the wall configuration of the RFX-mod with the vacuum vessel and the copper shell (red curve), for the vacuum vessel only (black line) and for the copper shell only (blue line). The dotted black curve corresponds to the case with the vacuum vessel and the shell treated as a magnetically thin wall. The parameters for the calculation are: $r_s/r_a=0.9$, $W/r_a=0.1$, $\alpha=1$ and $\tau_{sk}=\tau_{sk2}=0.6$ms.

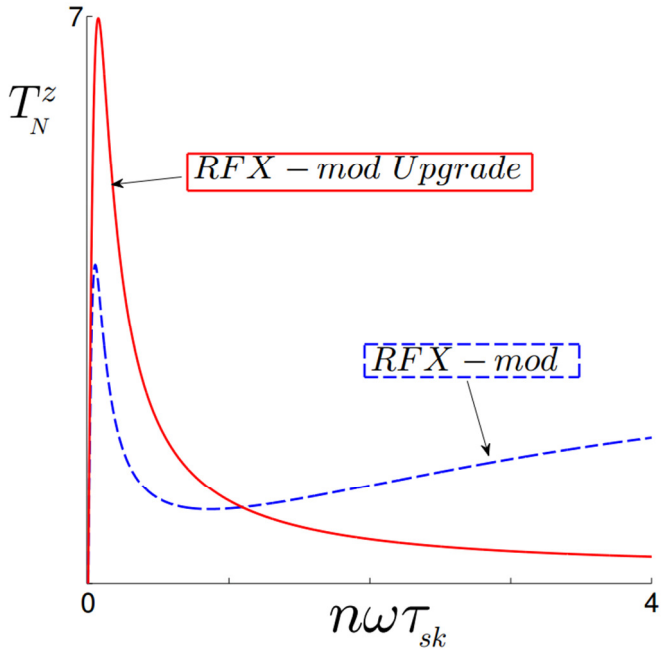

Fig. 6.9. Dependencies of T_N^z on the $m/n=2/1$ mode rotational frequency $n\omega\tau_{sk}$ for the wall configurations of the RFX-mod (dashed blue) and RFX-mod Upgrade (solid red curve). The parameters for the calculation are: $r_s/r_a=0.9$, $W/r_a=0.1$, $\alpha=1$ and $\tau_{sk}=0.6$ms.

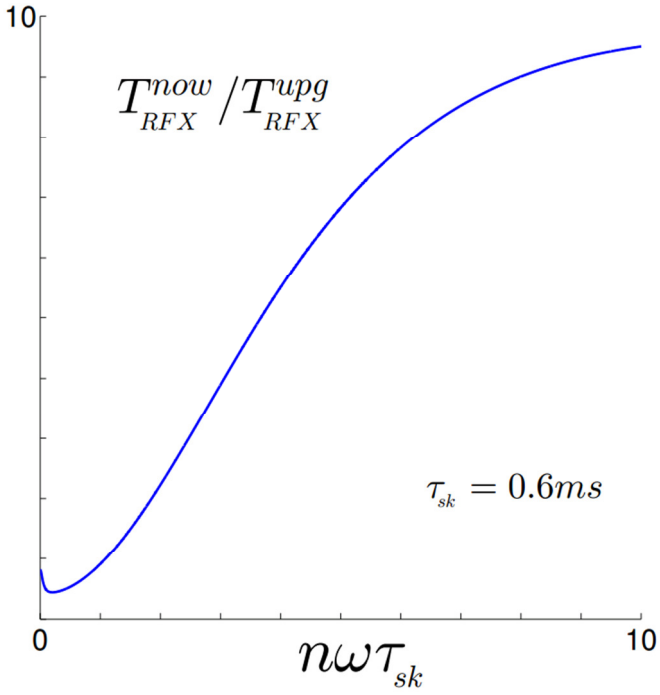

Fig. 6.10. The ratio of T_N^z for the wall configurations of the RFX-mod and RFX-mod Upgrade versus the $m/n=2/1$ mode rotational frequency $n\omega\tau_{sk}$. The parameters for the calculation are: $r_s/r_a=0.9$, $W/r_a=0.1$, $\alpha=1$ and $\tau_{sk}=0.6$ms.

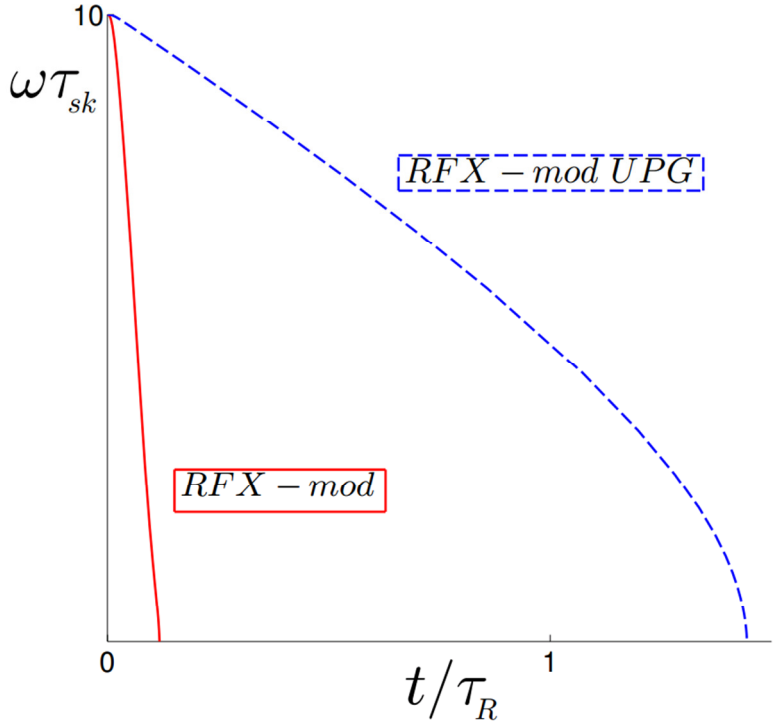

Fig. 6.11. The dynamics of $m/n=2/1$ island locking in RFX-mod (solid red) and RFX-mod Upgrade (dashed blue curve): The parameters for the calculation are: $r_s/r_a=0.9$, $\tau_A=0.5\mu s$, $\tau_R=1s$ and $R/r_a=4$.

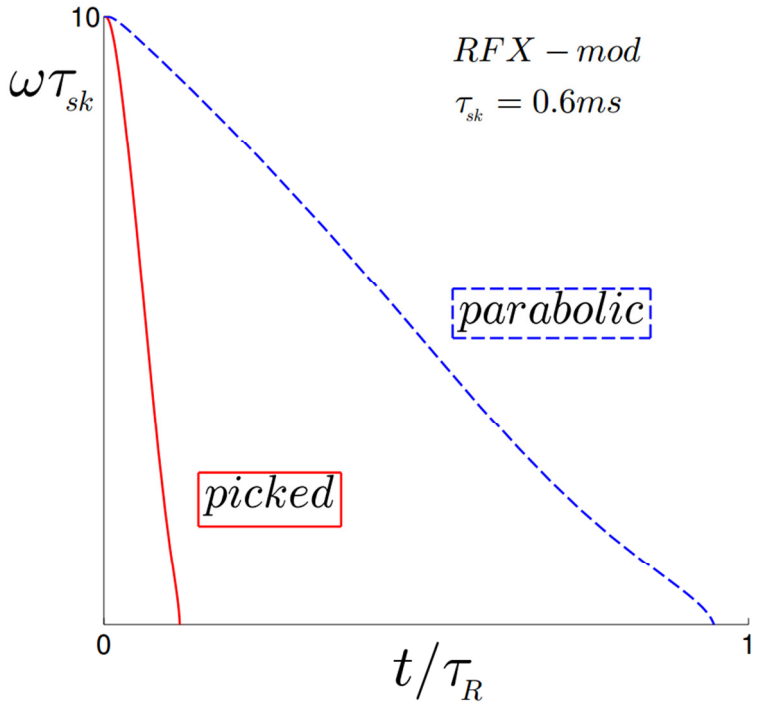

Fig. 6.12. The dynamics of $m/n=2/1$ island locking in RFX-mod tokamak for peaked (solid red) and parabolic (dashed blue curve) current profiles: The parameters for the calculation are: $r_s/r_a=0.9$, $\tau_A=0.5\mu s$, $\tau_R=1s$ and $R/r_a=4$.

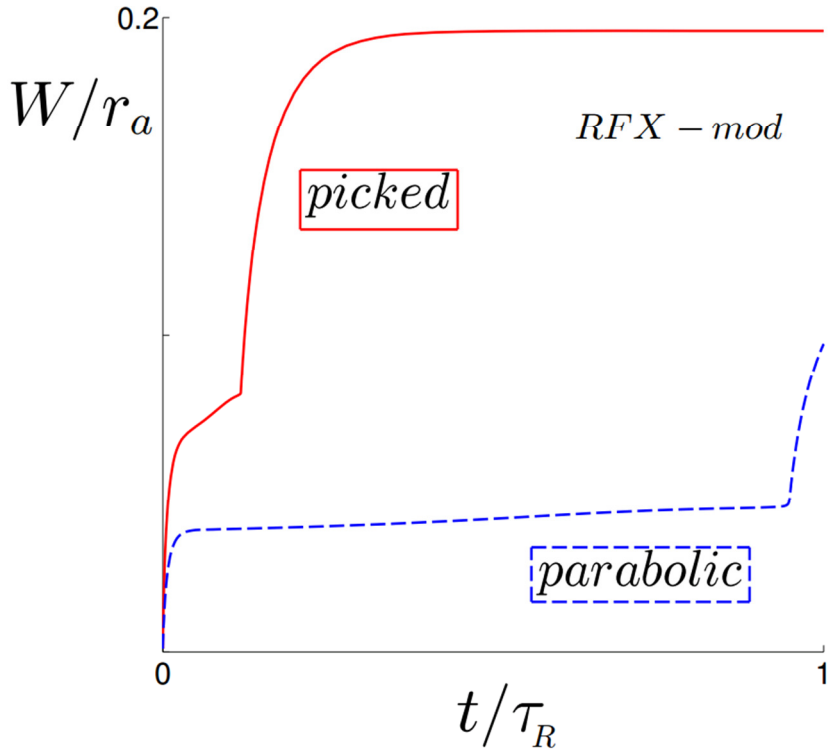

Fig. 6.13. The dynamics of $m/n=2/1$ island growth in RFX-mod tokamak for peaked (solid red) and parabolic (dashed blue curve) current profiles: The parameters for the calculation are: $r_s/r_a=0.9$, $\tau_A=0.5\mu s$, $\tau_R=1s$ and $R/r_a=4$.

6.6. Results for ITER geometry with double vacuum vessel and blanket

The assembly of ITER with blanket system and double vacuum vessel can be modeled as three nested coaxial cylindrical walls. The parameters of the nearest to the plasma wall that mimics the blanket are $r_{w1}/r_a = 1.125$ and $\tau_{w1} = 2ms$. The second wall is the inner shell of the vacuum vessel with $r_{w2}/r_a = 1.25$, $d_{w2}/r_{w2} = 0.024$, $\tau_{w2} = 82ms$ and $\tau_{sk2} = 2ms$. The third wall is the outer shell of the vessel with $r_{w3}/r_a = 1.625$, $d_{w3}/r_{w3} = 0.018$, $\tau_{w3} = 106ms$ and $\tau_{sk3} = 2ms$. These estimates are done for the low-field side midplane with $r_a = 2m$ [73], $r_{w1} = 2.25m$ [74], $\eta_{w1}/d_{w1} = 1.33\cdot 10^{-4}\Omega$ [74], $r_{w2} = 2.5m$ [75], $r_{w3} = 3.25m$ [75], $d_{w3} = d_{w3} = 60mm$ [75], and the total vacuum vessel wall time $\tau_{V.V.} = 188ms$ [76].

For the configuration with a magnetically thin wall between plasma and two walls, Γ_m in (6.16) and (6.25) is given by

$$\Gamma_m = in\omega\tau_{w1} + \frac{2m(r_{w1}/r_{w2})^{2m}\Gamma_2}{2m+\Gamma_2\left[1-(r_{w1}/r_{w2})^{2m}\right]}, \tag{6.51}$$

$$\Gamma_2 = -m - \left.\frac{r\psi'_{g2}}{\psi_{g2}}\right|_{w2-}, \tag{6.52}$$

$$\left.\frac{r\psi'_{g2}}{\psi_{g2}}\right|_{w2-} = y_{w2}\left.\frac{C_{w2}I'_m(y_{w2}) + K'_m(y_{w2})}{C_{w2}I_m(y_{w2}) + K_m(y_{w2})}\right|_{w2-}, \tag{6.53}$$

$$y_{w2} \equiv \frac{r}{d_{w2}}\sqrt{in\omega\tau_{sk2}}, \tag{6.54}$$

$$C_{w2} = -\left.\frac{y_{w2}K'_m(y_{w2}) - \dfrac{r\psi'_{g3}}{\psi_{g3}}K_m(y_{w2})}{y_{w2}I'_m(y_{w2}) - \dfrac{r\psi'_{g3}}{\psi_{g3}}I_m(y_{w2})}\right|_{w2+}, \tag{6.55}$$

$$\left.\frac{r\psi'_{g3}}{\psi_{g3}}\right|_{w2+} = -m\left.\frac{2m+\Gamma_3\left[1+(r/r_{w3})^{2m}\right]}{2m+\Gamma_3\left[1-(r/r_{w3})^{2m}\right]}\right|_{w2+}, \tag{6.56}$$

where subscripts $w2+$ and $w2-$ refer to the outer $r = r_{w2} + d_{w2}$ and inner $r = r_{w2}$ sides of the second wall, respectively.

$$\Gamma_3 = y_i \frac{K_{m-1}(y_i) I_{m-1}(y_e) - I_{m-1}(y_i) K_{m-1}(y_e)}{K_m(y_i) I_{m-1}(y_e) + I_m(y_i) K_{m-1}(y_e)}, \tag{6.57}$$

$$y_i \equiv \frac{r_{w3}}{d_{w3}} \sqrt{in\omega\tau_{sk3}} \text{ and } y_e \equiv y_i (1 + d_{w3} / r_{w3}), \tag{6.58}$$

moreover, instead of r_w in (6.16) and (6.25) one has to use r_{w1}.

In Fig. 6.14 the dependency of T_N^z on the $m/n = 2/1$ mode rotational frequency $n\omega\tau_{sk}$ is plotted for the vacuum vessel of ITER without blanket. The red solid curve shows the solution for the double vacuum vessel and the blue dashed line corresponds to the case with only inner shell of the vessel taken into account. The difference between the results is small. Therefore, in the study of the mode locking in ITER the outer shell of the vessel can be excluded from the analysis, $\Gamma_3 = 0$.

Three configurations of the ITER conducting structures are considered in Fig. 6.15: the vacuum vessel and the blanket (red solid), the vessel only (blue dashed) and the blanket only (black dash-dotted curve). For ITER $\tau_{sk} = 2$ ms and $\omega_{sk}\tau_{sk} = 1$ corresponds to $\nu_{sk} \equiv \omega_{cr} / 2\pi = 80$ Hz, while the initial mode frequency can be estimated as $\nu_{in} > 500$ Hz [77]. Therefore, these results show that neither blanket nor vessel can be excluded from the simulations of the mode locking in ITER. The dotted red line shows the case with the blanket and the inner shell of the vacuum vessel treated as magnetically thin walls. The difference from the exact solution (6.51) is insignificant, hence instead of (6.51) one can use

$$\Gamma_m = in\omega\tau_{w1} + \frac{2m(r_{w1}/r_{w2})^{2m} in\omega\tau_{w2}}{2m + in\omega\tau_{w2}\left[1 - (r_{w1}/r_{w2})^{2m}\right]}, \tag{6.59}$$

where $\tau_{w1} = 2ms$, $\tau_{w2} = 82ms$ and $r_{w1}/r_{w2} = 0.9$.

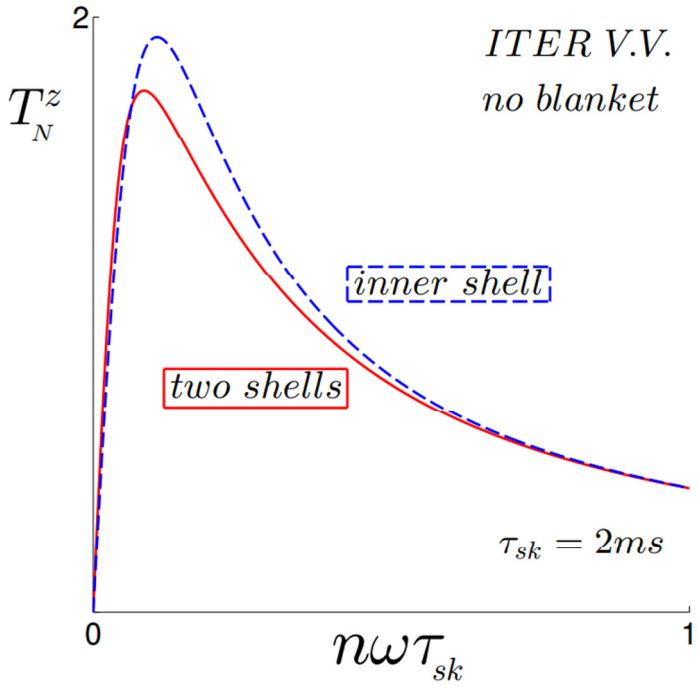

Fig. 6.14. Dependencies of T_N^z on the $m/n=2/1$ mode rotational frequency $n\omega\tau_{sk}$ for the wall configuration of ITER without blanket: with two shells of the vacuum vessel (red solid) and with only inner shell (blue dashed line). The parameters for the calculation are: $r_s/r_a=0.9$, $W/r_a=0.1$ and $\tau_{sk}=\tau_{sk2}=2$ms.

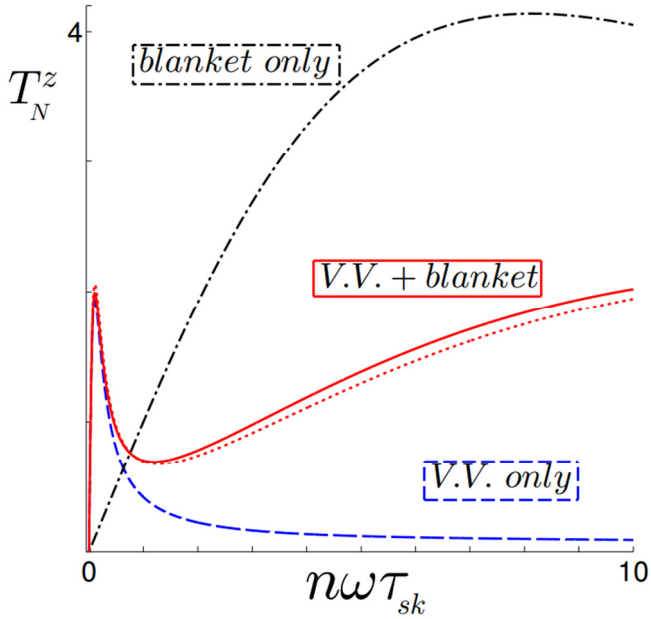

Fig. 6.15. Dependencies of T_N^z on the $m/n=2/1$ mode rotational frequency $n\omega\tau_{sk}$ for the wall configuration of ITER with the vacuum vessel and the blanket (red solid), for the vacuum vessel only (blue dashed) and for the blanket only (black dash-dotted curve). The dotted red line corresponds to the case with the blanket and the vacuum vessel treated as magnetically thin walls. The parameters for the calculation are: $r_s/r_a=0.9$, $W/r_a=0.1$ and $\tau_{sk}=\tau_{sk2}=2$ms.

6.7. Conclusions

For configurations with only one shell, and typical initial mode frequencies, $\omega_{in}\tau_{sk} >> 1$, the use of the thin wall approximation underestimates the electromagnetic torque acting on the plasma in $\sqrt{n\omega\tau_{sk}/2}$ times, and consequently, overestimates the locking time.

The wall ferromagnetism increases the torque in $\sqrt{\hat{\mu}}$ times, therefore, even for intermediate values of the magnetic permeability, $\hat{\mu} = 2-4$, the presence of ferritic materials must have notable impact on the dynamics of the locking.

When a highly-resistive wall is situated within a lowly-resistive wall, for the mode locking simulations both shells has to be taken into account and both can be modeled as magnetically thin walls (6.50) with a fair accuracy.

The comparison of the RFX-mod and RFX-mod Upgrade configurations predicts an order of magnitude longer locking time for the new machine.

The electromagnetic torque for the ITER assembly with double vacuum vessel and blanket can be calculated with fair accuracy neglecting the outer shell of the vacuum vessel and treating the inner shell as a magnetically thin wall (6.59). The blanket strongly affects the results and has to be taken into account.

The locking time and resulting saturated island width is found to be very sensitive to the assumption on the equilibrium current profile. More peaked current distribution leads to the faster locking and growth of the magnetic island.

VII. CONCLUSIONS OF THE WORK AND PERSPECTIVES

The sideways force acting on the vacuum vessel during disruptions is calculated within linear single-mode cylindrical analysis assuming the plasma to be separated from the wall by a vacuum gap. The derived formula gives the maximum force for the ideal wall, or in other words, for the fastest perturbations. However, there are strong theoretical indications [26] that the peak of the load has to be for the modes growing on the resistive wall time scale, $\gamma_R \tau_w \approx 1$, which is in agreement with non-linear numerical simulations performed on M3D code [33, 34].

Irrespectively to the question whether the plasma surface currents contribute to halo currents or not [36, 37], such single-mode analysis can be too simplified to make reliable predictions for ITER. The approach to the problem of the sideways forces calculation proposed in [26] allowing direct experimental verification can be a better way to extrapolate present force measurements to the ITER scale.

In the presence of the resistive wall, linear tearing modes can be stabilized by plasma rotation due to the resistive dissipation, in the range of parameters where the ideal wall provides their stability. The same result is found for RWMs, however, the comparison with the majority of experimental data on the rotational stabilization reveals discrepancy between the mode rotational frequency predicted by the model and observed in experiments. This difference can be caused by other effects: Landau damping [17], the mode resonances with Alfvén continuum [20] or bounce/precession motions of thermal [21, 22] and fast particles [23], which can also serve as additional energy sinks. To solve the question about the main mechanisms for the rotational stabilization of RWMs and possible interplay between them, the comparison of the contributions to the energy balance from every effect is needed [25]. This is the topic of future studies. The influence of the resistive dissipation in plasma on the RWM stability was analyzed under the assumption of continuity of ψ across the resistive layer. For non-zero pressure gradient constant-ψ approximation is violated and more delicate matching of the ideal solutions has to be performed, this work is currently in progress.

For advanced tokamak scenario with negative magnetic shear the differential plasma rotation at two rational surfaces is found to be destabilizing for the linear double tearing mode. However, we speculate that the finite pressure gradient effects in combination with the shift between mode and plasma rotational frequencies can change the total mode energy balance and can bring to the opposite conclusion.

The electromagnetic torque acting on the plasma is calculated for different wall arrangements within the approach that is free of any assumptions about the plasma. For configurations with only

one shell, and typical initial mode frequencies, $\omega_{in}\tau_{sk} >> 1$, the use of the thin wall approximation underestimates the electromagnetic torque acting on the plasma in $\sqrt{n\omega\tau_{sk}/2}$ times, and consequently, overestimates the time of the tearing mode locking. When a highly-resistive wall is situated within a lowly-resistive wall, for the mode locking simulations both shells has to be taken into account and both can be modeled as magnetically thin walls with a fair accuracy. The locking time and resulting saturated island width is found to be very sensitive to the assumption on the equilibrium current profile. More peaked current distribution leads to the faster locking and growth of the magnetic island.

The electromagnetic torque for the ITER assembly with double vacuum vessel and blanket can be calculated with fair accuracy neglecting the outer shell of the vacuum vessel and treating the inner shell as a magnetically thin wall. The blanket strongly affects the results and has to be taken into account. For $\omega_{in}\tau_{sk} >> 1$, the wall ferromagnetism increases the torque in $\sqrt{\hat{\mu}}$ times, therefore, even for intermediate values of the magnetic permeability, $\hat{\mu} = 2-4$, the presence of ferritic materials must have notable impact on the dynamics of the mode locking. While this result is directly applicable to HBT-EP [78] and JT-60SA [79] tokamaks with ferromagnetic inserts of the simple geometry, it is difficult to make quantitative predictions for ITER due to the uncertainties in the effective magnetic thickness of the ferritic blanket [80].

As a final general remark it could be said that the analytical models studied in this thesis addressing different aspects of the disruption problem (halo, eddy and surface currents, torque balance and mode locking, effect of the plasma rotation and boundary conditions on the mode stabilization) can grasp the complex plasma dynamics only partially. However, the handiness of the models and the easiness of parametric studies, are good features that, I hope, with future further refinements and expansions, can help in the interpretation of the results obtained with large numerical codes that, being extremely time and cost consuming, cannot cover the whole space of the physical parameters.

Bibliography

[1] Landau L D 1946 *J. Phys.* (Moscow) **10** 25

[2] Shafranov V D 1970 *Sov. Phys.-Tech. Phys.* **15** 175-83

[3] Kadomtsev B B and Pogutse O P 1973 *Zh. Eksp. Teor. Fiz.* **65** 575-589

[4] Mikhailovskii A B *Instabilities in a Confined Plasma* (Institute of Physics, Bristol, 1998)

[5] Bernstein I B *et al* 1958 *Proc. R. Soc. London, Ser. A* **244** 17

[6] Furth H P *et al* 1963 *Phys. Fluids* **6** 459

[7] Rutherford P H 1973 *Phys. Fluids* **16** 1903

[8] Wesson J *Tokamaks* (Oxford University Press, 2011)

[9] ITER Physics Basis 1999 *Nucl. Fusion* **39** 2251

[10] Hender T C *et al* 2007 *Nucl. Fusion* **47** S128

[11] Nicolas T 2013 Sawtooth driven particle transport in tokamak plasmas *PhD Thesis* Ecole Polytechnique Paris

[12] Pustovitov V D 2015 *J. Plasma Phys.* **81** 905810609

[13] Igochin V *Active Control of Magneto-hydrodynamic Instabilities in Hot Plasmas* (Springer-Verlag Berlin Heidelberg, 2015)

[14] Igochin V 2012 *Nucl. Fusion* **52** 074010

[15] Strait E J *et al* 1995 *Phys. Rev. Lett.* **74** 2483

[16] Taylor T S *et al* 1995 *Phys. Plasmas* **2** 2390

[17] Bondeson A and Ward D J 1994 *Phys. Rev. Lett.* **72** 2709

[18] Finn J M 1995 *Phys. Plasmas* **2** 198

[19] Finn J M 1995 *Phys. Plasmas* **2** 3782

[20] Gregoratto D *et al* 2001 *Plasma Phys. Control. Fusion* **43** 1425

[21] Liu Y Q *et al* 2004 *Nucl. Fusion* **44** 232

[22] Hu B and Betti R 2004 *Phys. Rev. Lett.* **93** 105002

[23] Liu Y *et al* 2010 *Plasma Phys. Control. Fusion* **52** 104002

[24] Pustovitov V D and Yanovskiy V V 2013 *Plasma Phys. Rep.* **39** 779

[25] Pustovitov V D 2015 *Nucl. Fusion* **55** 033008

[26] Pustovitov V D 2015 *Nucl. Fusion* **55** 113032

[27] Romanelli F and Laxåback M 2011 *Nucl. Fusion* **51** 094008

[28] Noll P *et al* 1996 *Proc. 19th Symp. on Fusion Technology* (Lisbon, Portugal, 1996) vol 1 p 751 www.iop.org/Jet/fulltext/JETP96044.pdf

[29] Riccardo V *et al* 2000 *Fusion Eng. Des.* **47** 389

[30] Riccardo V and Walker S P 2000 *Plasma Phys. Control. Fusion* **42** 29

[31] Riccardo V *et al* 2003 *Fusion Sci. Technol.* **43** 493

[32] Zakharov L E *et al* 2012 *Phys. Plasmas* **19** 055703

[33] Paccagnella R 2009 *Nucl. Fusion* **49** 035003

[34] Strauss H R *et al.* 2010 *Phys. Plasmas* **17** 082505

[35] Gerasimov S N *et al.* 2014 *Nucl. Fusion* **54** 073009

[36] Zakharov L E 2008 *Phys. Plasmas* **15** 062507

[37] Zakharov L E 2011 *Phys. Plasmas* **18** 062503

[38] Okabayashi M *et al* 2010 *Plasma Phys. Control. Fusion* **44** B339

[39] Takeji S *et al* 2002 *Nucl. Fusion* **42** 5

[40] Sabbagh S A *et al* 2002 *Phys. Plasmas* **9** 2085

[41] Reimerdes H *et al* 2005 *Nucl. Fusion* **45** 368

[42] Strait E J 2005 *Fusion Sci. Technol.* **48** 864

[43] Turnbull A D *et al* 2005 *Fusion Sci. Technol.* **48** 875

[44] Garofalo A M 2005 *Fusion Sci. Technol.* **48** 918

[45] Okabayashi M *et al* 2005 *Nucl. Fusion* **45** 1715

[46] Reimerdes H *et al* 2006 *Phys. Plasmas* **13** 056107

[47] Strait E J *et al* 2007 *Phys. Plasmas* **14** 056101

[48] Chu M S and Okabayashi M 2010 *Plasma Phys. Control. Fusion* **52** 123001

[49] Tanigawa H *et al* 2011 *J. Nucl. Mater.* **417** 9

[50] Tanigawa H *et al* 2012 Research and Development Status of Reduced Activation Ferritic/Martensitic Steels Corresponding to DEMO Design Requirement *Proc. 24th IAEA Fusion Energy Conf. (San Diego, 2012)* FTP/P7-17 http://www-naweb.iaea.org/napc/physics/FEC/FEC2012/papers/584_FTPP717.pdf

[51] Pustovitov V D and Yanovskiy V V 2013 *Plasma Phys. Rep.* **39** 345

[52] Pustovitov V D and Yanovskiy V V 2014 *Phys. Plasmas* **21** 022516

[53] Pustovitov V D and Yanovskiy V V 2015 *Phys. Plasmas* **22** 032509

[54] Pustovitov V D and Yanovskiy V V 2014 *Plasma Phys. Control. Fusion* **56** 035003

[55] Pustovitov V D and Yanovskiy V V Ferromagnetic destabilization of resistive wall modes in tokamaks *41st EPS Conf. on Plasma Phys. (Berlin, Germany, 2014)* P4.008 http://ocs.ciemat.es/EPS2014PAP/pdf/P4.008.pdf

[56] Mironov D V and Pustovitov V D 2015 *Phys. Plasmas* **22** 052502

[57] Mironov D V and Pustovitov V D, Analytical model of wall force produced by kink modes combined with plasma vertical displacement, *42nd EPS Conf. on Plasma Phys. (Lisbon, Portugal, 2015)* P5.183

[58] Webster A J 2010 *Phys. Plasmas* **17** 110708

[59] Furth H P *et al* 1973 *Phys. Fluids* **16** 1054

[60] Abramovitz M and Stegun I A *Handbook of Mathemathical Functions* (Dover Publications, New York, 1964)

[61] Jensen T H 1983 *J. Plasma Phys.* **30** 57

[62] Pritchett P L *et al* 1980 *Phys. Fluids* **23** 1368

[63] Pustovitov V D 2007 *Nucl. Fusion* **47** 1583

[64] Pustovitov V D 2011 *Nucl. Fusion* **51** 013006

[65] La Haye R J *et al* 2002 *Phys. Plasmas* **9** 2051

[66] White R B *et al* 1977 *Phys. Fluids* **20** 800

[67] Mikhailovskii A B 2003 *Contrib. Plasma Phys.* **43** 125

[68] Biskamp D *Nonlinear Magnetohydrodynamic* (Cambridge University Press, 2000) pp. 120-122

[69] Pankin A et al 2004 *Comput. Phys. Commun.* **159** 157

[70] Loarte A et al 2007 *Nucl. Fusion* **47** S203

[71] Stix T H 1973 *Phys. Fluids* **16** 1260

[72] Nave M F F and Wesson J A 1990 *Nucl. Fusion* **30** 2575

[73] Shimada M *et al* 2007 *Nucl. Fusion* **47** S1

[74] Villone F *et al* 2010 *Nucl. Fusion* **50** 125011

[75] Design description document of ITER vacuum vessel G A0 FDR 1 01-07-13 R1.0

[76] Navratil G, Bialek J and Katsuro-Hopkins O 2002 VALEN modelling of RWM control in FIRE and ITER *Second Meeting of the ITPA Topical Group on MHD, Disruption and Control (21–23 October 2002)* (Garching, Germany: IPP)

[77] Gormezano C *et al* 2007 *Nucl. Fusion* **47** S285

[78] Hughes P E *et al* 2015 *Rev. Sci. Instr.* **86** 103504

[79] Kamada Y *et al* 2013 *Nucl. Fusion* **53** 104010

[80] Tanigawa H *et al* 2008 *Fusion Eng. Des.* **83** 1471